AALBORG UNIVERSITY
DEPARTMENT OF PHYSICS
AND NANOTECHNOLOGY

MASTER'S THESIS

Formation of Metal-Polymer Nanocomposites Using Cluster Beam Technique

Author:
Florian A. Ceynowa

Supervisor:
Vladimir N. Popok

AALBORG UNIVERSITY
DENMARK

May 19, 2017

AALBORG UNIVERSITY
DENMARK

Department of Physics and Nanotechnology
Skjernvej 4A, 9220 Aalborg East
Phone +45 9940 9215
http://www.nano.aau.dk

Title:

Formation of Metal-Polymer Nanocomposites Using Cluster Beam Technique

Project Period:

September 1, 2016 - May 19, 2017

Author:

Florian A. Ceynowa

Supervisor:

Assoc. Prof. Vladimir N. Popok

Number of copies: 3
Number of pages: 88 (109)
Number of appendices: 2
Completed: May 19, 2017

Abstract:

This master's thesis deals with the formation of metal-polymer nanocomposite films and the characterization of their plasmonic properties. In the first part of the study, size-selected Cu nanoparticles (NPs) are deposited on thin films of poly(methyl methacrylate) (PMMA) and polystyrene (PS) utilizing a magnetron sputtering cluster apparatus. Dynamics of the NP embedding as well as effects of annealing on the localized surface plasmon resonance (LSPR) of NPs are studied. Treatment of as-deposited NPs in ozone promoting the formation of a thin oxide shell is found to be a promising way for preserving the LSPR on a long time scale in ambient conditions. In the second part, the cluster beam technique is combined with electron beam lithography to fabricate ordered arrays of Ag NPs. The feasibility of the approach is successfully demonstrated, and initial study of plasmonic properties is carried out.

PREFACE

This master's thesis was written by the author within the framework of the master's degree program *Nanomaterials and Nanophysics* at the Department of Physics and Nanotechnology at Aalborg University during the period September 1, 2016 - May 19, 2017.

Sources in this thesis are denoted by numbers in square brackets, i.e. [#]. These numbers correspond to entries in the bibliography found at the end of the thesis. If the reference is placed before a full stop, it refers to that sentence only. When placed after a full stop, it refers to the entire paragraph. Equations, inequalities, figures, and tables are abbreviated with Eq., Ineq., Fig., and Tab., respectively, and are numbered according to the chapter in which they are found, with the first figure in chapter 2 denoted by 2.1, the second by 2.2, etc. All graphs and images are referred to as figures. Figures without citation are created by the author. When referring to a specific part of the thesis, chapters, sections and the appendices are abbreviated with Chap., Sec., and App., respectively.

The author would like to thank Vladimir N. Popok for guidance during the entire project period and Manohar Chirumamilla for assistance with electron beam lithography.

Florian A. Ceynowa

Acronyms	
AFM	atomic force microscope/microscopy
CSE	cluster size effect
DDA	deposition-diffusion-aggregation
EBL	electron beam lithography
EQMS	electrostatic quadrupole mass selector
GAS	gas aggregation source
LSPR	localized surface plasmon resonance
MaSCA	magnetron sputtering cluster apparatus
MD	molecular dynamics
ML	monolayer
MS	mass spectral
NP	nanoparticle
OS	optical spectroscopy
PDMS	polydimethylsiloxane
PMGI	polymethylglutarimide
PMMA	poly(methyl methacrylate)
PS	polystyrene
RF	radio frequency
SCA	spherical cluster approximation
SCBI	supersonic cluster beam implantation
TEM	transmission electron microscope/microscopy

CONTENTS

CHAPTER 1

Introduction

Due to continuous tendency to miniaturization of electronic, optical, or other devices, there is an increasing need in understanding of the properties of materials on the nanoscale. Therefore, an attractive object of research in recent years are clusters which are aggregates of few to thousands of atoms (or molecules). Clusters possess properties intermediate between those of individual atoms (or molecules), characterized by discrete energy levels, and those of bulk matter characterized by continua or bands of states[1]. For example, bulk metals lose their high electrical conductivity upon size reduction and become insulating on the nanoscale[2]. Another distinct feature of clusters is the strongly increased surface-to-volume ratio which can e.g. be exploited in sensing or catalytic applications[3, 4]. In fact, clusters can be presumed to form a bridge between atoms (or molecules) and solid bulk as they depict a distinct form of matter with varying electrical, optical, magnetic, or chemical properties. Generally, they may be composed of same chemical constituents (homo-atomic clusters), or two or more different chemical species (hetero-atomic clusters). Depending on the chemical composition, they can be further characterized by different binding types as well as different geometric and electronic structures. When speaking about intermediate to large clusters, i.e. aggregates of hundreds to thousands of atoms (or molecules)[5], these can also be referred to as nanoparticles (NPs)[1].

Clusters are not only relevant for studying size effects on the nanoscale, but also attractive for applications in a range of different fields. For instance, metal NPs are applied for catalysis[6], cancer treatment[7], as antimicrobial agents[8], etc. By filling a polymer matrix with metal clusters, metal-polymer nanocomposites are obtained which combine favorable properties of the constituents. Thereby, interesting functional properties are acquired such as electrical conductivity including single-electron hopping, tunneling, and percolation[9] giving for instance rise to applications as H_2 sensors[10] or elastomeric electrodes[11], magnetic properties featuring ferromagnetic single domain behavior or superparamagnetism[12] which could find use in monolithic microwave integrated circuit devices[13], and localized surface plasmon resonance (LSPR) which can for example be exploited for optical transducers for protein sensing[14], Bragg reflectors[13], or for surface-enhanced Raman scattering[15].

In addition to promising functional properties of metal-polymer nanocomposites, polymers are generally low-cost materials and can be easily fabricated in different shapes.

There are several approaches for formation of metal-polymer nanocomposites among which are vapor phase deposition, ion implantation, wet chemical techniques, etc. Many of those approaches have the main disadvantage that they do not allow for independent control of NP size and filling factor, and properties of the polymer matrix. One of the recently demonstrated methods that overcome this problem is the cluster beam technique[16, 17] which is also used in this study.

The experimental work of the master's project is subdivided into two parts. In the main part, the metal-polymer nanocomposites are produced by deposition of Cu NPs on thin films of poly(methyl methacrylate) (PMMA) and polystyrene (PS) followed by thermal annealing above the polymer glass transition temperature (T_g) to facilitate embedment of the NPs. The main objectives are (i) to explore the capability of the employed magnetron sputtering cluster apparatus (MaSCA) in terms of cluster size selection and adjustability of the surface coverage, (ii) to study the immersion of Cu NPs into the polymer films in order to require better understanding of the thermodynamics and kinetics governing this process, and (iii) to examine the evolution of the plasmonic properties during embedding of the Cu NPs. In the second part, the aforementioned preparation method is combined with electron beam lithography (EBL) to fabricate ordered arrays of Ag NPs with specific periodicity. Here, the aim is (i) to verify the feasibility of the selected approach, and (ii) to investigate the plasmonic properties of the obtained arrays in view of potentially unique features which distinguish them from the optical properties of randomly deposited Ag NPs. In both parts, the prepared samples are thoroughly studied by means of atomic force microscopy (AFM) and optical spectroscopy (OS).

It may also be noted that a part of the conducted work has already been summarized in an article which is going to be published in the journal *Nuclear Instruments and Methods in Physics Research, B.* The accepted article is attached to the appendix, see App. A.

Chapter 2

Structure and Properties of Metal Clusters

This chapter is intended to overview the theory of structure and properties of metal clusters. First, different cluster sources are briefly mentioned, and the basics of cluster nucleation and growth are considered. Then, the electronic and geometric shell structure of smaller metal clusters is discussed, while emphasis is placed on the latter and its transition to the bulk crystal structure. Finally, general properties of metal clusters are discussed, including cluster size effects, electrical, and optical properties.

2.1. Formation of Clusters

There is a number of different types of cluster sources, some of which are listed below. Typically, the cluster generation can be divided into three main stages. First, *vaporization* of the atoms (or molecules) occurs which then condense and form a cluster nucleus (*nucleation*). In the final phase of the cluster formation, *growth* of these nuclei takes place so that larger clusters can be formed. The latter two stages will be addressed in more detail in Sec. 2.1.1.

Depending on e.g. used cluster species and desired cluster size, there must be appropriate methods for cluster production. Thus, several different approaches exist, and some of them are briefly presented in Tab. 2.1.[1, 18, 19]

Table 2.1. List of selected cluster sources with short description.

Cluster source	Description
Gas aggregation	A solid or liquid is evaporated into an aggregation chamber which is filled with cold inert gas at a few mbar. Due to supersaturation and collisions with the cold gas, the atoms nucleate and form clusters. Usually used for low-to-medium boiling ($< 2000\,\mathrm{K}$) materials. Possible to produce large clusters ($N > 20000$, N denoting number of atoms), but size distribution cannot be so easily controlled.
Laser vaporization	A high-power pulsed laser (e.g. Nd:YAG) erodes locally the target material and produces a vapor plume which is introduced into cold, inert gas to enable cooling and facilitate cluster formation. Both neutral and charged clusters of any metal can be produced. Small- to medium-sized (up to several hundreds of atoms) clusters.

Cluster source	Description
Arc discharge	An electric discharge vaporizes the target material, approximately 10% of the produced clusters are ionized.
Magnetron sputtering	Sputtering source in which low-pressure, inert gas (commonly Ar) is ionized by applying a d.c. or r.f. potential, hence, forming a highly reactive plasma. In addition, a magnetic field is applied to confine the plasma which is accelerated towards the cathode (target), resulting in sputtering of the material. Clusters of semiconducting and conducting materials can be produced, while problems may arise with ferromagnetic materials. Depending on the cluster constituents, 20%-80% can be ionized. Size can vary from several atoms up to over 10^6 atoms.
Supersonic (free-jet) expansion	While the aforementioned methods can include either supersonic or subsonic expansion, this approach is used to form clusters of rare gases or low-boiling metals by supersonic expansion through a nozzle into vacuum. This method is often combined with the gas aggregation technique by seeding of a low-melting metal in an inert gas at a stagnation pressure of several bars. Cluster size can be controlled by variation of stagnation pressure and nozzle diameter.

As already mentioned, a magnetron sputtering source was used in this project in order to deposit metal (Cu and Ag) NPs on bare or polymer-covered substrates. A more detailed description of the experimental setup and settings will be given in Sec. 5.2.

2.1.1. Nucleation and Growth

The starting point of cluster formation is the homogeneous nucleation. If the partial pressure of a pure vapor exceeds the saturated vapor pressure at a given temperature, it will become supersaturated corresponding to a metastable state. Over a certain period of time, it will go over into an equilibrium state by the formation and growth of very small droplets.[20] The subject of nucleation has already been goal of scientific research for several decades and a lot of literature can be found about it. Generally, there are two approaches to examine nucleation. The first one is the classical thermodynamic-kinetic approach utilized by Volmer and Weber[21], Becker and Döring[22], or Farkas[23]. The second method is based on statistical mechanics[24, 25] and was driven by the goal to solve the problems that arose from the classical theory. However, that has not succeeded completely and a definitive theory has yet to be invented.

A commonly used starting point for cluster nucleation is the three-atom collision in a supercooled gas. The formation of a dimeric nucleus is enabled, if the binding energy of the dimer is higher than the local thermal energy of the beam while the third atom removes the excess energy as kinetic energy (KE)[18, Ch. 1.3]. If metal atoms (M) are considered, this process can be presented as follows:

$$\mathrm{M} + \mathrm{M} + \mathrm{M}(\mathrm{KE}_1) \longrightarrow \mathrm{M}_2 + \mathrm{M}(\mathrm{KE}_2 > \mathrm{KE}_1) \tag{2.1}$$

Besides the energy stabilization, it is also necessary that the momentum conservation is fulfilled at the same time[1]. In the presence of an inert, cold gas (buffer gas) such as He, the nucleation becomes more efficient:

$$\mathrm{M} + \mathrm{M} + \mathrm{He}(\mathrm{KE}_1) \longrightarrow \mathrm{M}_2 + \mathrm{He}(\mathrm{KE}_2 > \mathrm{KE}_1) \tag{2.2}$$

The formed dimer then acts as a condensation nucleus for further growth.[18, Ch. 1.3] The following cluster growth can be divided into four consecutive stages: attachment of atoms, coagulation, coalescence, and aggregation[26, Ch. 9.1]. This is illustrated in Fig. 2.1. As with the description of the nucleation process, the following explanation of the cluster growth is made using the example of metal clusters.

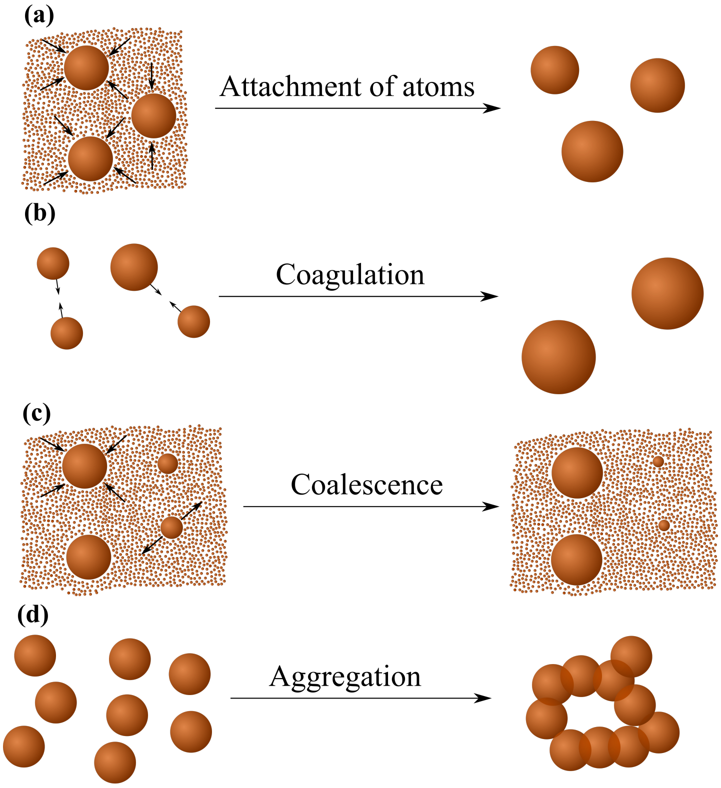

Figure 2.1. Schematic representation of the four stages in cluster growth: (a) attachment of atoms, (b) coagulation, (c) coalescence, and (d) aggregation.

First, the formed condensation nuclei grow by attachment of metal atoms according to the scheme

$$\mathrm{M}_\mathrm{n} + \mathrm{M} \longrightarrow \mathrm{M}_{\mathrm{n}+1}, \tag{2.3}$$

where n denotes the number of metal atoms. Considering metal atoms, this attachment process typically proceeds much faster than the three-atom collision as the rate constant of the latter process is a few orders of magnitude smaller than the reduced rate constant for atomic attachment to the cluster surface[27]. As a result, there will already be large clusters in the first phase of cluster growth.

The second phase of cluster growth is coagulation, see Fig. 2.1(b). It is defined as the merging of two individual clusters to a single cluster according to

$$\mathrm{M_{n-m}} + \mathrm{M_m} \longrightarrow \mathrm{M_n}, \tag{2.4}$$

with n and m denoting the number of atoms in each cluster. It should be noted that the coagulation process is sometimes also called coalescence in the literature, leading to some confusion. Considering the cluster growth in the beam, these two terms describe two different processes as it will become clear from the further explanation below.

In the third stage, coalescence takes place which follows from the interaction of the cluster with a parent atomic vapor, see Fig. 2.1(c). The process is also termed Ostwald ripening and basically constitutes the growth of larger clusters at the expense of smaller ones, when the degree of supersaturation is very low[28]. In particular, the evaporation rate for clusters of a size larger than the critical cluster size is lower than the rate of atomic attachment to these clusters, while the opposite relation holds true for smaller clusters. Therefore, larger clusters grow while the smaller ones disappear, resulting in an increased average cluster size. The critical cluster size depends on the number density of free metal atoms, the diffusion coefficient for metal atoms in a buffer gas, temperature, etc.

In the last phase of cluster growth, the grown clusters are joined but preserve partially their initial shape. This process is called aggregation and is depicted in Fig. 2.1(d).[26, Ch. 9] During the different stages of cluster growth, the internal energy and, thus, the temperature of the clusters is increased considerably due to the heat of condensation of the added atoms. In order to decrease their temperature, there are mainly three different cooling mechanisms which are presented below.

(a) Collisional cooling: By collision of the clusters with atoms in the beam, the latter can transfer the excess energy away as kinetic energy:

$$\mathrm{M_n(T_1)} + \mathrm{B(KE_1)} \longrightarrow \mathrm{M_n(T_2 < T_1)} + \mathrm{B(KE_2 > KE_1)} \tag{2.5}$$

Here, B might be an atom of the same chemical element as M or a cold, inert gas.

(b) Evaporative cooling: Evaporation of one or more atoms lowers the internal energy of the clusters in an endothermic process. In order for evaporation to occur, the activation energy barrier for bond breaking must be overcome by channeling of the internal energy into the cluster vibrational modes. The excess energy is carried away as kinetic energy by the evaporating atom:

$$\mathrm{M_n(T_1)} \longrightarrow \mathrm{M_{n-1}(T_2 < T_1)} + \mathrm{M(KE)} \longrightarrow \mathrm{M_{n-2}(T_3 < T_2)} + \mathrm{M(KE)} \tag{2.6}$$

As soon as collisions no longer occur in the cluster source, this is the only cooling mechanism.

(c) Radiative cooling: Emission of an infrared photon can lower the cluster's internal energy:

$$\mathrm{M_n(T_1)} \longrightarrow \mathrm{M_n(T_2 < T_1)} + h\nu \tag{2.7}$$

This cooling mechanism, however, takes longer than most experiments and is thus very inefficient. Regarding the cluster source used in this project (see Sec. 5.2), the cluster formation is further supported by additional cooling of Ar and He gases with liquid N_2. It becomes obvious now that the clusters do not continuously grow but also shrink due to evaporation of atoms in order to lower their internal energy. In addition, they can also reduce their size by fragmentation, i.e. splitting into smaller clusters. Thus, there is a continuous competition between growth and decay.

2.2. Transition to Bulk Structure

Considering a small metal cluster composed of a few atoms and the subsequent attachment of additional atoms to it, several properties change drastically with increasing size, including the electronic and geometrical shell structure of the cluster. This section shortly introduces the transition from the electronic to the geometrical shell structure in metal clusters, before the second transition to the bulk crystal structure is discussed for increasing cluster size.

A good starting point for the first discussion part are the mass spectral (MS) studies of large Na clusters carried out by Martin *et al.*[29], see Fig. 2.2.

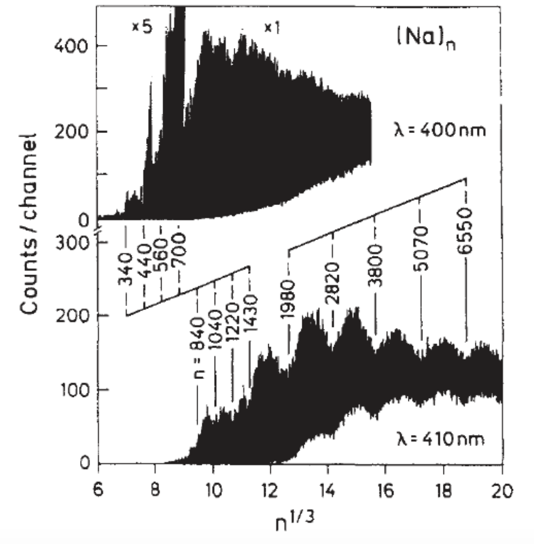

Figure 2.2. MS intensity measurements for large Na clusters showing evenly spaced, periodic oscillations.[18]

The spectra were obtained using near-threshold photoionization in order to produce cluster cations. Clusters with pronounced stability have higher ionization energies and, thus, show minima in the MS intensity. Nuclearities (numbers of atoms) corresponding to these dips are also called magic numbers.

As can be seen from Fig. 2.2, the MS intensity shows two sequences of periodic oscillations which are approximately evenly spaced when plotted against $N^{1/3}$. For $N < 2000$, these oscillations have a shorter period. In this size regime, the magic numbers can be assigned to filling of electronic shells which arise from single electronic sub-shells bunching together at high energy. Thus, the smaller Na clusters are also said to adopt the electronic shell structure.[18, Ch. 4] For the first demonstration of electronic shell structure, the reader is referred to the publication by Knight *et al.*[30]. With increasing nuclearity, the electronic shells evolve into bands with quasi-continuous levels so that the cluster's stability is no longer governed by electron shell filling. Instead, it is dominated by geometric shell effects as it is indicated in Fig. 2.2 by longer period oscillations for $N > 2000$. This means that the pronounced stability occurs now due to filling of concentric, polyhedral shells of atoms. It should be noted that the cluster size at which transition to geometric shell structure occurs is dependent on a number of factors, e.g. the density of electronic states, the atomic electron configuration, the cluster's melting temperature, and the temperature of the cluster. Several geometric shell structures exist, but the most abundant ones for metal clusters are icosahedra, decahedra, and cuboctahedra[29]. For instance, the icosahedral structure is built by arranging 12 neighboring atoms at the corners of an icosahedron around one central atom (considered as the first shell), thus, completing the second shell. Next, 42 atoms make a third shell so that the original symmetry is regained. The number of cluster atoms for each filled geometric shell is the magic number and for the icosahedral structure, it can be determined as follows

$$N^*(K) = \frac{1}{3}\left(10K^3 - 15K^2 + 11K - 3\right), \tag{2.8}$$

where K denotes the number of shells. For instance, $K = 1, 2, 3, 4, ...$ gives the magic numbers $N^* = 1, 13, 55, 147, ...$, respectively. Fig. 2.3 depicts the icosahedral shape for the third, fourth, and fifth completed, geometric shell.

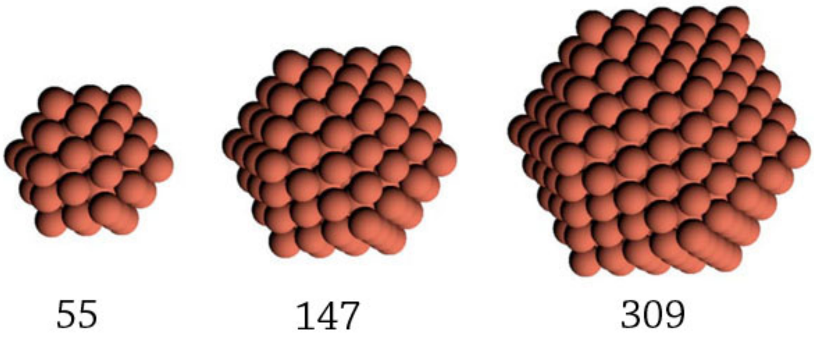

Figure 2.3. Three icosahedra with the third, fourth, and fifth shell completed corresponding to the magic numbers 55, 147, and 309, respectively.[31]

Unlike the previously mentioned Na clusters, the transition metal clusters adopt the geometric shell structure at much lower nuclearity. This is related to the partially filled, tightly bound valence *d* orbitals in each atom leading to narrow bands with small energy level spacing, already at small cluster size. Cu clusters, which are produced in this project, are assumed to have icosahedral shape at small sizes as it is reported in several studies[32–35]. Icosahedral structure is favorable at low nuclearity because it has a high surface coordination number (number of nearest neighbors of surface atoms), resulting in a minimized surface energy. However, icosahedra posses fivefold symmetry which is incompatible with the translation symmetry observed in crystals. Therefore, the Cu clusters have to undergo a structural phase transition to their bulk face-centered cubic (fcc) structure at a critical nuclearity (N_c). The icosahedron is constructed of 20 tetrahedra sharing a common vertex. Since tetrahedra can be cut out of a fcc crystal, one could mistakenly ascribe the icosahedra a crystalline growth as well. However, the tetrahedra are not space filling so that they need to distort slightly in order to fill out the whole volume. This leads to an elastic strain which increases with rising cluster size. Upon reaching N_c, this strain is high enough to destabilize the geometric shell structure (low surface energy, high strain) and the transition to bulk-like crystalline structure (high surface energy, low strain) occurs.[18,29] Reinhard *et al.*[36] have studied this transition for Cu_N (produced by inert-gas aggregation technique based on metal evaporation) using electron diffraction and molecular dynamics (MD) simulations, and reported it to occur at a critical cluster diameter of about 3.8 nm. Applying the spherical cluster approximation, which will be introduced in the following section, and including the factor for highest packing density, this corresponds to $N_c = 1849$ (with $R_{WS}(\mathrm{Cu}) = 0.14\,\mathrm{nm}$[37], see Eq. 2.10).

Similarly, Ag clusters are also expected to adopt the icosahedral structure for smaller sizes but have been predicted to undergo transition to fcc-like structures for N on a scale of a few hundreds[38]. However, previous studies of unsupported Ag clusters produced by inert-gas aggregation technique revealed the existence of icosahedral structures consisting of a few 10^6 atoms[39], even though fcc structure is predicted for these cluster sizes considering the energy state of the system. The authors explained this observation by the conditions of cluster growth (dense and cool metallic vapor) which were dominated by kinetic factors, thus, enabling the formation of metastable structures far away from thermodynamic equilibrium. Recently, Barke *et al.*[40] investigated the 3D structure of unsupported Ag clusters (produced by magnetron cluster source[41]) using single-shot wide-angle scattering of femtosecond soft X-ray free-electron laser pulses. They reported the existence of metastable structures for even larger sizes, e.g. truncated octahedra and icosahedra for cluster diameters of 200 nm and 240 nm, respectively. However, these polyhedral structures constituted only a small fraction of all observed clusters since the absolute majority showed fcc structure. The Ag clusters produced in this project are expected to have fcc structure as previous studies by transmission electron microscopy (TEM) have revealed[16].

2.3. General Properties of Metal Clusters

As mentioned before, various properties of metal clusters differ extremely from the bulk materials. In this section, some of them will be addressed and explained both quantitatively and qualitatively.

2.3.1. Scaling Laws

In the medium to large cluster regime (hundreds to thousands of atoms), many common properties (G) show a smooth dependence on the cluster nuclearity, e.g. ionization energy (IE), melting temperature (T_m), electron affinity, or binding energy[18, Ch. 1.2]. These cluster size effects (CSEs) can be described within the framework of the spherical cluster approximation (SCA) in which a cluster is modeled by an N-atom sphere with specific cluster radius (R_c), surface area (S_c), and volume (V_c).

As a first approximation, the cluster volume is determined by multiplying the number of atoms with the volume of the constituent atoms (V_a)

$$V_c = NV_a \tag{2.9a}$$

$$\tfrac{4}{3}\pi R_c^3 = N\tfrac{4}{3}\pi R_{WS}^3, \tag{2.9b}$$

where R_{WS} denotes the Wigner-Seitz radius which is defined as the radius of a sphere whose volume is equal to the volume occupied by one atom in the bulk material[42]. By rearranging Eq. 2.9b, it follows that

$$R_c = N^{1/3} R_{WS}. \tag{2.10}$$

This $N^{1/3}$-dependency of the cluster radius, by the way, also explains the periodic occurrence of MS intensity dips related to geometric shell closing which were presented in Fig. 2.2. The surface area of a cluster in relation to that of an atom (S_a) is governed by

$$S_c = 4\pi R_c^2 = 4\pi \left(N^{1/3} R_{WS}\right)^2 = 4\pi N^{2/3} R_{WS}^2. \tag{2.11}$$

Considering the medium to large cluster regime, the number of cluster surface atoms (N_s) is then obtained by dividing the surface area of the cluster by the cross-sectional area of one atom (A_a) as

$$N_s = \frac{4\pi N^{2/3} R_{WS}^2}{\pi R_{WS}^2} = 4N^{2/3}. \tag{2.12}$$

Finally, the fraction of surface atoms (f_s) is given as

$$f_s = \frac{N_s}{N} = 4N^{-1/3}. \tag{2.13}$$

As it will turn out below, this is an important property that is directly related to several CSEs. However, Eq. 2.13 should be considered carefully as it is only valid for larger clusters. It breaks down for approximately $N < 300$ where already 60% of the cluster atoms are sitting on the surface (according to Eq. 2.13)[18, Ch 1.2]. By adopting the SCA, simple scaling laws can be used to predict the size-dependent variation of a generic property (G). They are given in Eqs. 2.14 and 2.15 as functions of the cluster radius and the nuclearity, respectively:

$$G(R_c) = G(\infty) + aR_c^{-\alpha} \tag{2.14}$$

$$G(N) = G(\infty) + bN^{-\beta} \tag{2.15}$$

While $G(\infty)$ is the bulk limit value, typically obtained from experiments[43], a and b are constants in the respective equations. Since many properties of clusters depend on the fraction of surface atoms, and $f_s \propto N^{-1/3} \propto 1/R_c$ (see Eqs. 2.13 and 2.10, respectively), α and β generally adopt the values 1 and 1/3. Using these simple scaling laws, several CSEs can be determined in accordance with experimental results. For instance, the ionization energy of K clusters is governed by the following equation

$$IE^K(N)/eV = 2.3 + 2.04N^{-1/3}, \tag{2.16}$$

where the first term gives the work function of bulk potassium. As can be seen from Fig. 2.4, the experimentally predicted values are in good agreement with the interpolation given by Eq. 2.16.

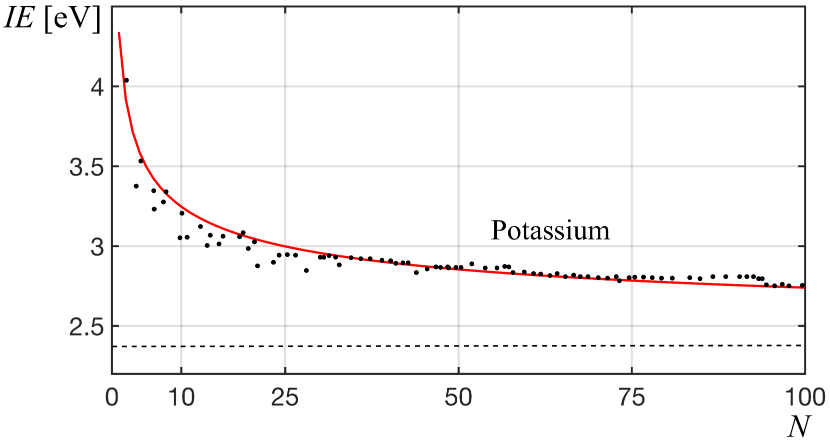

Figure 2.4. Ionization energy of K clusters as a function of the number of atoms. The points are experimental data, and the solid line is given by Eq. 2.16.[18]

Another example is the size-dependent variation of the melting temperature in Au clusters which follows a $1/R_c$ trend and can be expressed in the form

$$T_m^{Au}(R_c)/K = 1336.15 - 5543.65(\text{Å}/R_c). \tag{2.17}$$

Again, the experimental data show good agreement with the values obtained by Eq. 2.17, see Fig. 2.5.

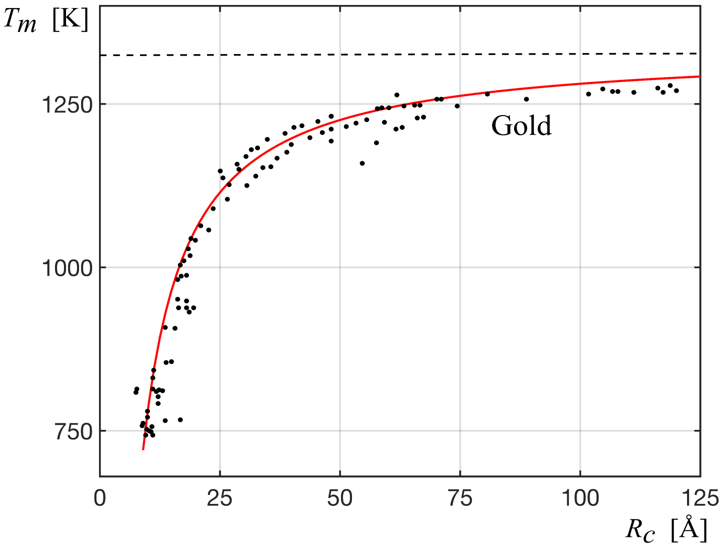

Figure 2.5. Melting temperature of Au clusters as a function of cluster radius. The points are experimental data, and the solid line is given by Eq. 2.17.[18]

As already indicated, the scaling laws are only applicable for larger clusters showing a smooth variation with the nuclearity or cluster radius. In contrast, the properties of small clusters do not follow these simple equations, but feature large deviations or oscillations which arise either from quantum mechanical effects (e.g. electronic shell closing) or surface size effects (e.g. geometric shell closing, see [44]) which were discussed in the previous section.[18, Ch. 1.2]

2.3.2. Metal-Insulator Transition

In addition to the aforementioned CSEs, the electrical properties of metal clusters can also deviate strongly from those of their bulk counterparts. In particular, by varying NP size or the amount of NPs embedded in an insulating matrix (e.g. polymer matrix), a metal-insulator transition takes place at a critical NP size or at a critical concentration of embedded metal clusters, respectively. Both of these metal-insulator transitions are addressed in the following.

Size-Induced Transition

As indicated above, metals show a drastic change in their electrical properties during size reduction from bulk crystals to small clusters comprising a few atoms. This is schematically illustrated in Fig. 2.6 where three different size regimes are depicted. The *macroscopic* range corresponds to the bulk metal, while the *mesoscopic* regime constitutes large- to small-sized clusters, thus, bridging the gap to the *microscopic* region of single atoms, or molecules.

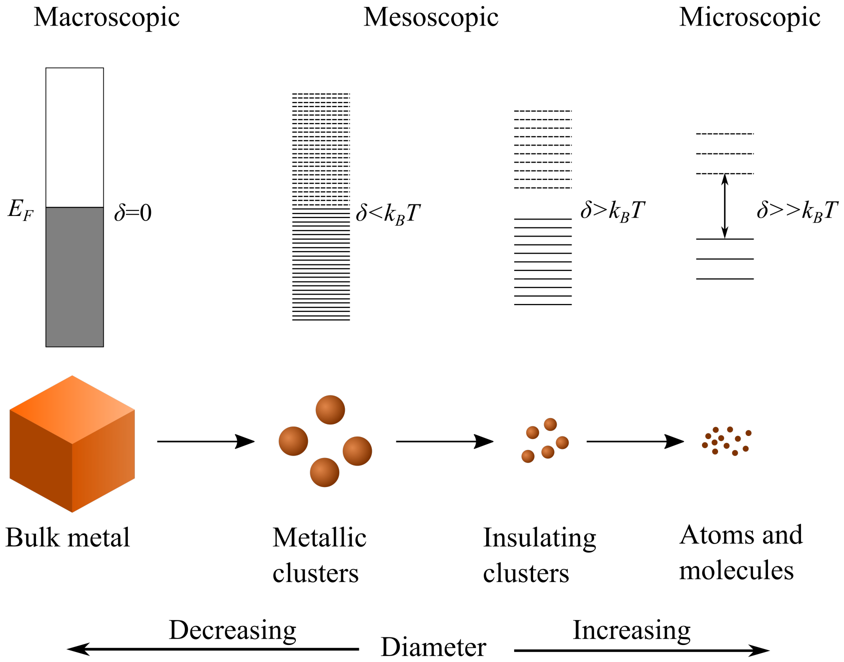

Figure 2.6. Schematic drawing showing the evolution of electronic structure in metals during size reduction. The size-induced metal-insulator transition takes place in the mesoscopic regime.[18]

Starting in the macroscopic regime, bulk metal is characterized by infinitesimally separated energy levels, and the electronic structure can be described by means of the band theory. Metals have one or more partially filled energy bands, with the Fermi level (E_F) representing the highest occupied electronic state at the absolute zero point ($T = 0\,\mathrm{K}$). Directly above E_F, there is a number of empty states which can be easily populated even at low temperature, providing a high electrical conductivity.[45, Ch. 4.8] However, with decreasing size of the metal down to the mesoscopic regime, the energy levels become discrete and there is a finite energy level spacing (δ) at E_F which increases during further size reduction. Now, the question arises at which size the size-induced transition from metallic to insulating state occurs. According to Kubo, the cluster possesses metallic conductivity when the thermal energy is sufficiently high to excite electrons into empty states. Thus, the transition takes place when the thermal energy is equal to δ according to[46]

$$\delta = k_B T = \frac{4E_F}{3N}, \tag{2.18}$$

where k_B is the Boltzmann constant, and δ is also called Kubo gap. As an example, Cu clusters ($E_F(\mathrm{Cu}) = 7\,\mathrm{eV}$) exhibit metallic conductivity at room temperature ($T = 293\,\mathrm{K}$) when $N > 369$. Within the SCA, this corresponds to a cluster diameter ($d = 2R_c$, see Eq. 2.10) of about 2 nm. This result has to be taken with care since the SCA and Eq. 2.18 are only approximations, but it gives a guiding value.

Percolation

The other considered insulator-metal transition (or vice versa) occurs in an insulating medium (e.g. polymer matrix) in which metal NPs are embedded in a disordered manner. As a starting point for the discussion, a metal-insulator composite obtained by immersion of the deposited metal NPs into the insulating matrix is considered. Starting with a low initial surface coverage (before immersion, p), the consecutive stages of a metal film in an insulating matrix with increasing p are schematically depicted in Fig. 2.7.

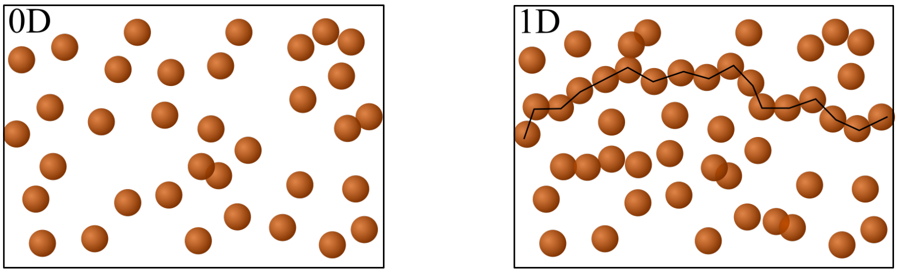

(a) Insulating regime ($p < p_c$). **(b)** Transition regime ($p \approx p_c$).

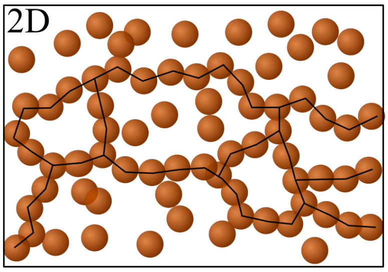

(c) Percolation regime ($p > p_c$).

Figure 2.7. Schematic representation of the consecutive growth stages of a metal film in an insulating matrix and the corresponding condcution regimes.[47]

As shown in Fig. 2.7 (a), the clusters are first separated from each other so that no current can flow (0D conduction). Thus, the composite possesses the electrical conductivity of the insulating material which is zero. When the critical coverage (p_c) corresponding to the percolation threshold is reached, the first percolation path along the deposited clusters forms (1D conduction, see Fig. 2.7 (b)) and a sharp conduction onset occurs[48]. With increasing p, more paths become available and the percolating film evolves from a 1D to a 2D conductor (see Fig. 2.7 (c)), leading to a strong increase in the electrical conduction over several orders of magnitude. According to the 2D percolation theory[49], the conductivity (σ) of the metal-insulator composite follows the relationship

$$\sigma \propto (p - p_c)^{\mu}, \tag{2.19}$$

where μ is the critical exponent. σ is commonly also written in the alternative form[48,50]

$$\sigma \approx \sigma_0(\phi - \phi_c)^{\mu}, \tag{2.20}$$

where σ_0 is a proportionality constant, ϕ is the normalized metal concentration, and ϕ_c is the critical concentration or percolation threshold. There is general consensus that μ takes values smaller than 2 in the percolating regime. However, it should be noted that electron transport in the metal-insulator composite can also occur via tunneling or a combination of percolation and tunneling below but near ϕ_c. In those cases, some isolated percolating paths are formed between which tunneling conduction can be observed below a certain separation distance, see Fig. 2.8.

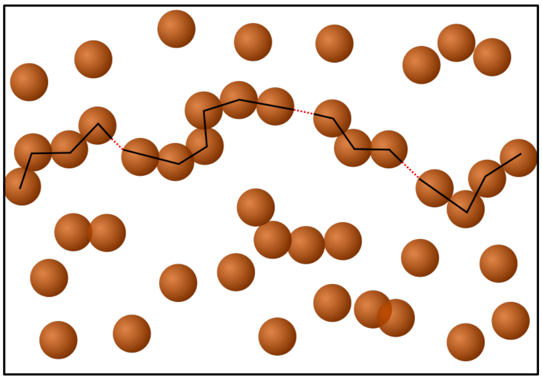

Figure 2.8. Schematic drawing of the tunneling-percolation regime in a metal-insulator composite with p just below p_c.[10]

In this tunneling-percolation regime, the critical exponent μ is greater than 2. It is also interesting to note that the tunneling current and, thus, the conductivity depend exponentially on the cluster separation[10,51]. This can used for sensing applications, in which it is taken advantage of this phenomenon. For instance, Brown *et al.*[10] produced H_2 sensors by deposition of Pd clusters on SiO_2-coated Si substrates. Upon absorption of H_2, the Pd clusters expand and decrease the gap between the isolated conduction paths, thus, causing a huge increase of the current which could be measured.

The percolation threshold (ϕ_c) can vary considerably for different metal-insulator composites, and values between 0.01 and 0.5 can be found in literature[50]. For example, low-energy implantation of Au into PMMA revealed a percolation threshold of about 0.45[48], while low-energy implantation of Au and Ti in polydimethylsiloxane (PDMS) with high fluences yielded critical metal concentrations of 0.06-0.08 for Au and 0.11-0.13 for Ti[52]. Finally, it is also worth mentioning that the resistivity evolution of cluster-assembled metallic thin films deviates strongly from the one of atom-assembled films as it was demonstrated by Barborini *et al.*[47]. They used supersonic cluster beam deposition for formation of W, Mo, Nb, Pd and Fe cluster-assembled films and measured the current as a function the film thickness. Surprisingly, the corresponding resistivity curves showed considerably higher resistivity evolution compared to the one reported for atom-assembled films. In addition, the results revealed an increasing asymptotic trend with rising thickness (reaching the 3D conduction regime) instead of decreasing values converging to the bulk ones as it is reported for atom-assembled films[53]. The authors ascribed the discrepancy in the resistivity between cluster- and atom-assembled films to the minimal cluster-cluster contact area and nanoscale grain boundaries, while they attribute the increasing asymptotic trend to an increased surface roughness and accompanied worsened topological connection of the uppermost layers.

2.3.3. Optical Properties

Localized Surface Plasmon Resonance

Metal NPs have fascinating optical properties which differ strongly from their bulk counterpart. For instance, when illuminated by white light they appear in different colors depending predominantly on their size and shape. This is directly linked to the localized surface plasmon resonance (LSPR) whose applications in physics, biology, or medicine are extensively explored nowadays. However, this optical phenomenon is nothing new as it was already applied in the stained glasses of old church windows, giving them their glimmering colors[54]. This subsection is intended to give a basic understanding of the LSPR in metal NPs. Some of the key equations are given and the physical meaning is explained as well. For a more detailed discussion of the LSPR and applications, the reader is referred to [55, 56].

When a metal NP is exposed to an electromagnetic wave (whose wavelength is assumed to be much larger than the spatial dimension of the NP), the electric field polarizes the particle and displaces the electron cloud relative to the nucleus. Subsequently, the resulting restoring force, which arises from the Coulomb attraction between electrons and nuclei, leads to oscillation of the conduction electrons about the core, see Fig. 2.9.

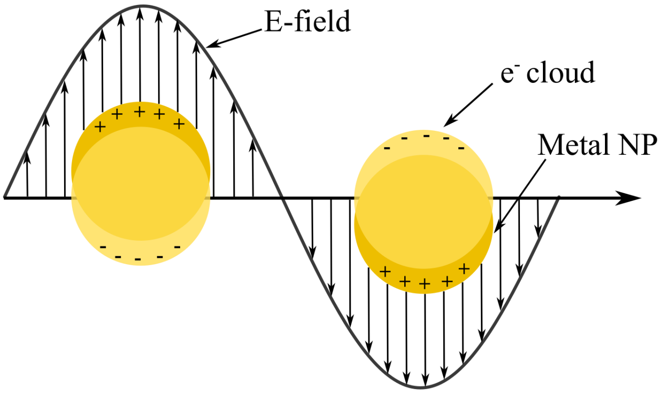

Figure 2.9. Schematic drawing of the LSPR in metal NPs. Under exposure to the electric field, the electron cloud becomes displaced relative to the core, leading to collective oscillations of the conduction electrons.

When the frequency of the light matches the frequency of the oscillating conduction electrons, the resonance condition is established, and the light is strongly absorbed and/or scattered.

In the following, the interaction between the electromagnetic field and a particle is treated within the *quasi-static approximation* which is valid when the particle diameter is much smaller than the wavelength of light[56, Ch. 5]. In this case, the phase of the electromagnetic field is approximated to be constant over the entire particle. Thus, the problem can be approached by assuming a homogeneous, isotropic sphere of radius a located at the origin in a static electric field $\mathbf{E} = E_0\hat{\mathbf{z}}$, see Fig. 2.10. Here, $\hat{\mathbf{z}}$ denotes the unit vector in z-direction, ε_m is the dielectric constant of the surrounding medium (which is isotropic and non-absorbing), and $\varepsilon(\omega) = \varepsilon_1 + i\varepsilon_2$ is the dielectric function of the sphere.

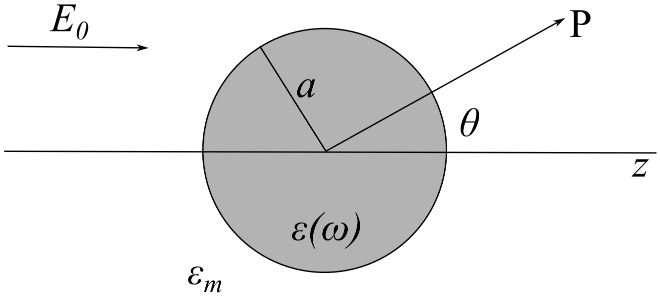

Figure 2.10. Schematic drawing of a homogeneous sphere located at the origin in an electrostatic field.

First, the Laplace equation for the potential, $\nabla^2 = 0$, has to be solved. Due to the symmetry of the problem, the solutions for the potential inside (Φ_{in}) and outside (Φ_{out}) the sphere are of the form

$$\Phi_{in}(r,\theta) = \sum_{l=0}^{\infty} A_l r^l P_l(\cos\theta) \tag{2.21a}$$

$$\Phi_{out}(r,\theta) = \sum_{l=0}^{\infty} \left[B_l r^l + C_l r^{-(l+1)}\right] P_l(\cos\theta), \tag{2.21b}$$

where $P_l(\cos\theta)$ are the Legendre Polynomials of order l, and θ is the angle between the position vector $\mathbf{r}$ at point P and the z-axis (see Fig. 2.10). After applying the boundary conditions ($\Phi_{out} \to -E_0 z = -E_0 r\cos\theta$ as $r \to \infty$; equality of tangential components of electric field and normal components of displacement field for $r = a$), the coefficients A_l, B_l, and C_l can be determined, and the potentials evaluate to[56, Ch. 5]

$$\Phi_{in} = -\frac{3\varepsilon_m}{\varepsilon + 2\varepsilon_m} E_0 r\cos\theta \tag{2.22a}$$

$$\Phi_{out} = -E_0 r\cos\theta + \frac{\mathbf{p}\cdot\mathbf{r}}{4\pi\varepsilon_0\varepsilon_m r^3} \tag{2.22b}$$

$$\mathbf{p} = 4\pi\varepsilon_0\varepsilon_m a^3 \frac{\varepsilon - \varepsilon_m}{\varepsilon + 2\varepsilon_m}\mathbf{E_0}, \tag{2.22c}$$

for $l = 1$. ε_0 is the vacuum permittivity, and $\mathbf{p}$ is the dipole moment. Eq. 2.22b means physically that Φ_{out} is a superposition of the applied field and that of a dipole located at the NP center. In other words, the applied field induces a dipole moment inside the sphere that is proportional to $|\mathbf{E_0}|$. Next, the (complex) polarizability (α) can be introduced via the relation $\mathbf{p} = \varepsilon_0 \varepsilon_m \alpha \mathbf{E_0}$ yielding

$$\alpha = 4\pi a^3 \frac{\varepsilon - \varepsilon_m}{\varepsilon - 2\varepsilon_m}. \tag{2.23}$$

It should be emphasized that this is an important result within the quasi-static approximation. When $|\varepsilon - 2\varepsilon_m|$ is a minimum, the polarizability is resonantly enhanced. Assuming a small or slowly varying $\mathrm{Im}[\varepsilon]$ around the resonance, the resonance condition simplifies to

$$\mathrm{Re}[\varepsilon(\omega)] = -2\varepsilon_m, \tag{2.24}$$

which is also called the *Fröhlich condition* for the dipole surface plasmon in a metal NP. Taking an Ag NP in air ($\varepsilon_m = 1$) as an example, the condition becomes $\varepsilon_1 = -2$. From the dielectric data given in [57], it can be easily seen that this condition leads to a LSPR at about 355 nm, which is in fairly good agreement with experimental studies[14, 16]. Furthermore, Eq. 2.24 states that the resonance frequency is dependent on the dielectric environment: For instance, an increased value of ε_m requires a decreased value of ε_1 in order for the Fröhlich condition to be fulfilled. Since ε_1 typically decreases with increasing wavelength in the spectral range of interest[57], this leads to a redshift (to higher wavelengths) of the absorption peak. Another implication of the resonantly enhanced polarizability is the improved efficiency of the metal NP in scattering and absorbing light. This is represented by the according cross sections for scattering (C_{sca}) and absorption (C_{abs}), which are written as

$$C_{sca} = \frac{k^4}{6\pi}|\alpha|^2 = \frac{8\pi}{3}k^4 a^6 \left|\frac{\varepsilon - \varepsilon_m}{\varepsilon - 2\varepsilon_m}\right|^2 \tag{2.25a}$$

$$C_{abs} = k\mathrm{Im}[\alpha] = 4\pi k a^3 \mathrm{Im}\left[\frac{\varepsilon - \varepsilon_m}{\varepsilon - 2\varepsilon_m}\right], \tag{2.25b}$$

where k denotes the wave vector. For small NPs with $a \ll \lambda$, C_{abs}, which scales with a^3, dominates, and scattering can be neglected. For example, calculations of El-Sayed *et al.*[58] using the dipole approximation method showed that for Au NPs, no scattering occurs for $a \leq 20$ nm. However, with increasing size, the magnitude as well as the relative contribution of C_{sca} increases as it scales with a^6. From Eqs. 2.25 it follows that absorption and scattering are resonantly enhanced when the Fröhlich condition is fulfilled (see Eq. 2.24). The sum of both contributions gives the extinction cross-section within the quasi-static limit[56, Ch. 5]

$$C_{ext} = 9\frac{\omega}{c}\varepsilon_m^{3/2} V \frac{\varepsilon_2}{[\varepsilon_1 + 2\varepsilon_m]^2 + \varepsilon_2^2}, \tag{2.26}$$

with V and c denoting the volume of a sphere and the speed of light, respectively. With increasing V (or size), the intensity of the resonance peak increases as well. In addition to the NP size, dielectric environment, and particle species, there are more factors affecting the spectral position and intensity of the plasmon band, e.g. particle shape, surface roughness, or interparticle distance. However, they are not further addressed here as this would be beyond the scope of this work.

Chapter 3

Cluster-Surface Interaction

This chapter is concerned with the cluster-surface interaction in the low-energy regime. After describing the soft landing of clusters on the surface, diffusion mechanisms as well as possible scenarios upon collision of these clusters are discussed. Here, both experimental and theoretical results from literature are presented to verify the accuracy of the presented model.

After formation of clusters in the cluster source, they can be put into interaction with the substrate surface upon impact. Here, the kinetic energy (E_{kin}) of the beam is an important parameter to define the regime of cluster-surface interaction. A reasonable approach is to divide the cluster-surface interaction into *low-* and *high-energy* ones[1]. In the former regime, the kinetic energy per atom (E_{at}) is smaller than the binding (cohesive) energy (E_{coh}, can be on the scale of eV/atom for metal clusters) of the cluster constituent atoms. Thus, the clusters typically preserve their composition, i.e. do not fragment, and there is no atom exchange with the surface[59]. However, the shape of the cluster can be slightly distorted by plastic deformation, especially when E_{at} is close to E_{coh} or when the cluster-surface interaction is high. The low-energy regime is also called soft landing or deposition, see Fig. 3.1 (a).

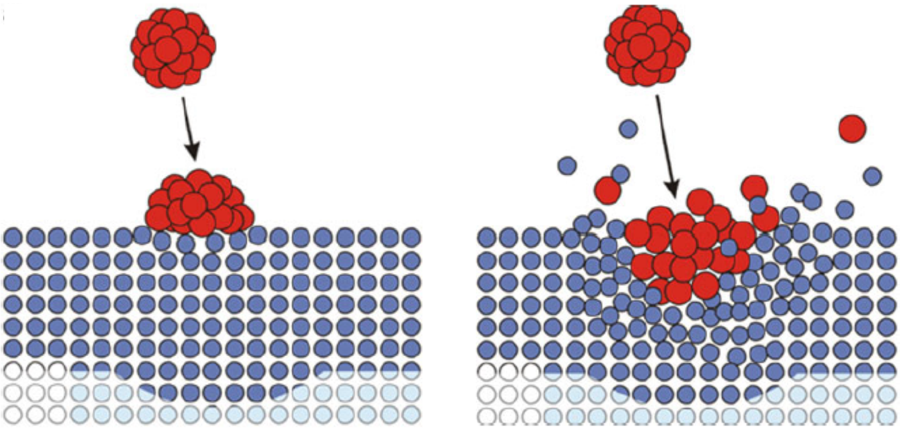

(a) Cluster deposition. **(b)** Cluster implantation.

Figure 3.1. Illustration of the kinetic regimes for cluster-surface interaction.[60]

If E_{at} is larger than E_{coh}, this corresponds to the high-energy regime. Depending on the magnitude of E_{at}, there are different possible processes to occur. If E_{at} slightly exceeds

E_{coh}, the impact induces strong plastic deformation and minor fragmentation, but most of the constituent atoms stay intact. With increase in E_{at}, the clusters decompose and fragment. These fragments can either be backscattered from the surface or implanted in the surface, if the locally transferred energy is larger than the penetration threshold energy, see Fig. 3.1 (b). Even higher E_{at} can lead to erosion of the surface, i.e. sputtering of surface atoms or crater formation.[1]

3.1. Soft Landing

Since the cluster source was only used in the low-energy regime of cluster-surface interaction in the experiments, this section addresses only cluster deposition (or soft landing) in more detail. The main idea of soft landing is the conservation of the properties of clusters. If immobilized on the surface after deposition, it is convenient to study them in terms of their properties or possible applications.[1] As already mentioned, material exchange between cluster and substrate as well as fragmentation can be kept to a minimum or completely prevented. In general, the cluster-surface interaction is very complex in the low-energy regime and many factors need to be considered, e.g. cluster size and material, and substrate properties such as surface energy, hardness, corrugation, temperature, and polarizability[61].

The degree to which the structure of the cluster is altered during impact is strongly related to the cluster-surface interaction energy. It is defined as the energy gain after deposition compared to the preceding situation of the cluster separated from the surface, and it depends on the binding energy of cluster constituents to the substrate, and surface and interface energies[1]. Examples of very high cluster-surface interaction energies are Ag_7 and Ag_{19} on Pd(100) and Pd(111), respectively. MD simulations have shown that these clusters are partly implanted and atomic site exchange occurs, even at low E_{kin} (close to zero)[62]. Generally, high substrate temperatures or soft landing at step edges promote wetting of the substrate. However, the former have stronger impact on smaller clusters since these possess epitaxial order with respect to the crystal structure of the substrate already at lower temperatures compared to larger ones. This is experimentally demonstrated for Fe clusters on W(110) using reflection high energy electron diffraction (RHEED)[63]. Since the cluster-surface interaction energy is more important compared to E_{kin} for smaller clusters, restructuring of these clusters is often unavoidable and the conservation of their properties is not always given.

With increasing cluster size, structural deformation and atomic exchange becomes less important compared to E_{kin}. As mentioned before, the penetration threshold energy has to be overcome for implantation. Since the energy available for each atom decreases with increasing cluster size, the atomic exchange mechanism becomes less probable.[59] Thus, conservation of the unique properties is more likely for larger clusters compared to smaller ones. For instance, Hanif *et al.*[16] used magnetron sputtering to deposit size-selected Ag clusters with mean size of 13 nm ($N = 67047$ and $R_{WS}(\mathrm{Ag}) = 0.16\,\mathrm{nm}$[64], see Eq. 2.10) on thin polymer films. Using both AFM and TEM, they showed that the NPs almost preserved their spherical shape as they slightly flattened upon impact with

E_{at} on a scale of a few meV. In this case, succeeding in soft landing might also be related to the low interaction of the metal NPs with the polymer.

3.2. Surface Diffusion, Aggregation and Coalescence

After deposition on the substrate, the clusters can diffuse on the surface if the activation barrier is overcome. Furthermore, collision of two clusters can lead to coalescence or aggregation. In this context, coalescence represents the merging of two particles and the formation of a larger one with eventually altered shape. It should not be confused with the definition used in the description of cluster growth, see Sec. 2.1.1. On the other hand, clusters can collide and stick irreversibly to form an immobilized island. This process is called aggregation and is typically observed for larger clusters[1]. A typical morphology observed for aggregated clusters is depicted in Fig. 3.2 (a), showing a TEM micrograph of Sb_{2300} deposited on graphite (by thermal evaporation).

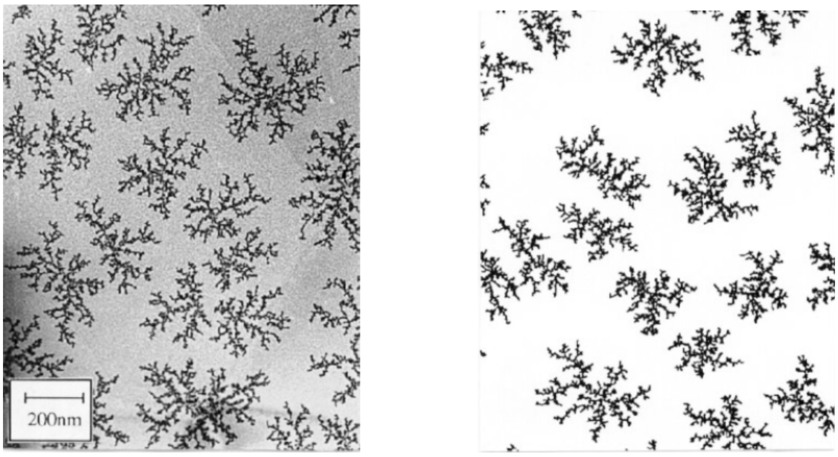

(a) TEM micrograph of Sb_{2300} on graphite.

(b) Simulation using DDA model.

Figure 3.2. Experimentally (a) and theoretically (b) obtained results for deposition of Sb_{2300} on graphite.[65]

In order to understand the mechanisms leading to the formation of these ramified island, Perez *et al.*[65] developed the *deposition-diffusion-aggregation* (DDA) model which is defined as follows.

1. Deposition: Clusters arrive randomly on the surface with a flux (F) and per unit surface per unit time.
2. Diffusion: During the diffusion time (τ), isolated clusters move by their diameter (d) in random directions.
3. Aggregation: When two clusters meet, they stick irreversibly and the formed islands are assumed to be immobile.

It should be noted that these are dynamic processes which are simultaneously present during the experiment. It is convenient to introduce the normalized flux (ϕ), which is defined as the number of clusters deposited per site (projected area of cluster on surface) and per unit time, as

$$\phi = \frac{F\tau\pi d^2}{4}. \tag{3.1}$$

Furthermore, the cluster diffusion coefficient is governed by

$$D = \frac{d^2}{4\tau}. \tag{3.2}$$

During the initial phase of film growth, the number of islands grows while their average size changes slightly. At the next stage, the island size increases as well, and the number of islands reaches a maximum and saturates.[61] As predicted by the DDA model, the saturation island density depends on the normalized flux according to

$$N_{isl} = 0.5\phi^{\chi} \qquad \chi = 0.36. \tag{3.3}$$

From comparison of the experimentally obtained results (see Fig. 3.2 (a)) with the simulated ones using the DDA model (see Fig. 3.2 (b)), it can be seen that the obtained island morphologies resemble each other quite well. Furthermore, from experimental observation of the island size distribution and the evolution of N_{isl}, Jensen *et al.*[66] concluded that dimers (islands containing two clusters) do not move on the substrate.

The combination of Eqs. 3.1, 3.2, and 3.3 yields the following expression for the diffusion coefficient:

$$D = \frac{F\pi d^4}{16}\left(\frac{0.5}{N_{isl}}\right)^{1/\chi} \tag{3.4}$$

While increasing the substrate temperature stepwise, Perez *et al.* measured the corresponding values of N_{isl} in order to determine D. After plotting the diffusion coefficient versus the temperature, they fitted the obtained data by an Arrhenius law of the form

$$D = D_0 exp\left(-\frac{E_a}{k_B T}\right), \tag{3.5}$$

where D_0 is a constant prefactor and E_a is the activation energy. The results revealed high prefactors close to $10^4\,\mathrm{cm}^2\,\mathrm{s}^{-1}$ for Sb_{2300} and Au_{250} on graphite. Since these values are considerably higher than the ones for atomic diffusion ($D_0 = 10^3\,\mathrm{cm}^2\,\mathrm{s}^{-1}$[67]), the authors ruled out atomic diffusion mechanisms such as periphery diffusion and evaporation-condensation diffusion suggested for 2D islands[68]. Instead, they assumed the diffusion of the clusters as a whole. One possible mechanism is rotation which would explain the immobilization of two clusters after collision as their rotational degrees of freedom would freeze upon contact. In fact, rotation has already been observed for C_{60} clusters which were moved by a scanning tunneling microscope (STM) tip[69]. MD studies of Au_N on graphite have showed that the clusters predominantly move by a combination of translation and rotation[70]. Furthermore, motion by rolling has also been reported for carbon nanotubes on highly ordered pyrolytic graphite (HOPG) when both are in commensurate contact[71]. In general, the surface diffusion of the clusters is enhanced for weak cluster-surface interaction. In addition, the diffusion coefficient is also increased when cluster and substrate are incommensurate, i.e. when the atoms in the contact facet are not congruent with the surface, since the activation barrier is reduced in this case[72].

Perez *et al.*[65] also suggest a critical size for the transition from coalescence to aggregation. More precisely, they assume two diffusing clusters to merge when at least one of them is smaller than the critical size. As discussed in Sec. 2.3.1, the melting point of metal clusters is size-dependent and is strongly decreased on the nanoscale. If one assumes that at least one of the merging clusters has to be liquid-like, the critical size could be equated with the melting size of the cluster. However, this assumption needs to be refined and a detailed explanation of the critical size has yet to be made.

So far, the role of surface defects was not taken into account. However, it should be noted that defects can have a strong influence on the film morphology. Yoon *et al.*[73] investigated this influence for Sb_{2500} deposited on HOPG which was exposed to ion irradiation. They observed that the film morphology evolved from ramified islands to random packing as the number of defects increased. Moreover, Carroll *et al.*[74] investigated the influence of steps in the surface of graphite on the growth of Ag_{400}. Similar to the case of adatom diffusion, they observed trapping of the clusters at the step edges.

Chapter 4

Metal-Polymer Nanocomposites

After giving a short overview of alternative preparation methods for the formation of metal-polymer nanocomposites, the approach used in the current project is addressed in more detail. In particular, thermodynamics and kinetics of the immersion of metal NPs into thin polymer films are discussed both qualitatively and quantitatively, and experimental studies of this process are presented regarding the embedding process as well as the polymer surface dynamics. Finally, state-of-the-art approaches for formation of metal-polymer nanocomposites are described which enable independent control of polymer properties, and NP size distribution and filling factor.

4.1. Preparation Methods

Aside from the preparation method utilized in the current project, there are several other ways to produce metal-polymer nanocomposites. In the following, the most commonly used methods are presented and briefly explained.

4.1.1. Vapor Phase Deposition

There are already various preparation methods based on vapor phase deposition which are applied for the formation of metal-polymer nanocomposites. In general, they constitute co- or tandem deposition of metallic and organic components, with the metal NPs being formed via self-organization and embedded in the polymer matrix. Vapor phase deposition is commonly characterized by good process control. One of the key benefits is the possibility to control the filling factor of the metal NPs in the polymer matrix over the entire range from zero to unity. In addition, careful modification of the metal/polymer deposition rates (R_m/R_p) enables the formation of layers with filling factor gradients. In most cases, however, the NP size increases simultaneously with increasing filling factor. This means that an independent control of the particle size is limited.[51]

Evaporation: Co-evaporation of metal-polymer nanocomposites is carried out from two separate evaporation sources. Examples for the formation of the polymer matrix are evaporation of monomers and subsequent condensation on the substrate[75], or thermal cracking of polymers into fragments which repolymerize partially on the substrate[76]. Compared to the co-sputtering approach, the kinetic energy of the metal atoms reaching the polymer surface is much lower. Therefore, the metal volume fraction of the composites strongly depends on the sticking coefficient of the metal atoms on the polymer, and on the ratio R_m/R_p; It rises with increasing value of R_m/R_p[77]. Drawbacks of the co-evaporation technique are the limited selection of suitable polymers, low condensation probability of metal atoms on polymers with low surface energy, and a strong decline of the molecular weight after deposition resulting in poor mechanical properties.[51]

Sputter Deposition: Another sub-category of vapor phase deposition is co- and tandem sputtering for the formation of metal-polymer nanocomposites. This approach is a combination of rf magnetron sputtering of polymers from a polymer target and dc sputtering from a metal or alloy target. In contrast to co-evaporation, the polymers are crosslinked after deposition, leading to enhanced mechanical properties compared to the original polymers. However, as with co-evaporation, only certain polymers are suited for sputter deposition. Here, the decisive point is the competition between crosslinking and chain scission of the polymers. It is expected that polymers with high sputter rate possess a low crosslinking tendency. For example, excellent candidates are Teflon and Nylon. The films obtained by co-sputtering deposition are similar to the ones prepared by plasma polymerization, but sputtering of polymers like Teflon enables the formation of films with higher thickness and reduced internal stress.[51]

Laser Ablation: This is a new approach which can be carried out in vacuum or in solution. Under vacuum conditions, the formation of the nanocomposites is carried out by laser ablation from a metallic and polymeric target. Thus, it resembles somewhat the co-sputtering process. For the approach in solution, the metal target is surrounded by a liquid in which the NPs directly form. The liquid also contains dissolved monomer and polymer molecules for the formation of the polymeric matrix.[51] The nanocomposites obtained using this method were mainly used for medical applications so far[78].

4.1.2. Ion Implantation in Polymers

In this method, metal NPs are synthesized in polymers by implantation of metal ions with kinetic energies on the scale of a few tens keV, thus, leading to the formation of metal-polymer nanocomposites. Above a certain fluence threshold (typically about $10^{16}\,\mathrm{cm}^{-2}$ for majority of polymers[50]), the implanted metal ions nucleate in a process including accumulation leading to supersaturation, formation of nuclei, and their growth resulting in metal clusters. Nucleation is favored due to the high metal cohesive energy and the low metal-polymer interaction energy. Advantages of this technique include the possibility to obtain high metal filling factors, to produce any metal/dielectric nanocomposites, and to form the NPs at specific depths in the polymer. The independent control of the NP size is limited. One of the disadvantages of ion implantation is that the metal NPs are not uniformly distributed over the depth of the polymer. Since larger NPs are formed at the depth corresponding to the highest concentration of metal ions this also leads to size dispersion in the polymer that is often observed to widen with increasing ion fluence.[50] Due to the high kinetic energy of the ions the polymer is severely damaged by ion stopping, leading to a number of effects accompanying the structural evolution of the polymer matrix, e.g. breaking of chemical bonds and scission of polymer chains resulting in degassing of volatile compounds, or cross-linking. In carbon-based polymers, i.e. in most polymers, ion implantation causes carbonization along with formation of conjugated bonds. On the one hand, this can lead to a favored change in properties, e.g. increased electrical conductance. On the other hand, the accompanied change in dielectric properties of the matrix can cause unwanted quenching of the LSPR of the metal NPs[79].

4.1.3. Wet Chemical Techniques

Regarding wet chemical techniques, both in situ and ex situ processes are used. In the former approach, which is applied more often, the NPs are formed within the polymer matrix by reduction of metal salts, or by decomposition of metal complexes. In the ex situ method, the NPs are produced separately by means of chemical methods allowing the control of size and shape of the particles. Subsequently, they are dispersed in a polymer or monomer solution for the following polymerization. Contrary to vapor phase deposition, wet chemical techniques are not restricted to thin films, but it is also possible to prepare bulk samples.[51]

4.2. Embedding of Nanoparticles into Thin Polymer Films During Thermal Annealing

In the current study, metal-polymer nanocomposites are obtained by embedding of metal NPs into thin polymer films via thermal annealing of the samples. In this section, this immersion process is examined more carefully in matters of the thermodynamic driving force and experimental observations giving information about the embedding mechanism, surface dynamics of polymers, and the kinetics.

4.2.1. Thermodynamics

The following discussion treating the thermodynamics of the embedding process refers to the work of Kovacs *et al.*[80,81]. As a starting point, a system of a rigid sphere of radius a and a rigid substrate is considered, see Fig. 4.1 (a). According to Kovacs *et al.*[80], the thermodynamically preferred state of this system is the one with the lowest Helmholtz free energy (F) which is the state function used to describe isothermal, isochoric processes. For simplification, the volume contribution of F is assumed to be constant, while only the surface contribution varies with the film-substrate configuration. Furthermore, the materials are assumed to be homogeneous with isotropic surface tensions.

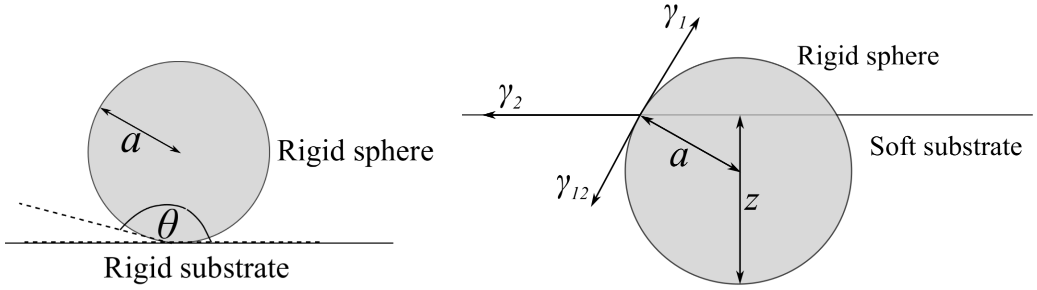

(a) Rigid sphere on rigid substrate.

(b) Partially embedded, rigid sphere in soft substrate.

Figure 4.1. Illustration of sphere-substrate system before and after embedding.

As can be seen in Fig. 4.1 (a), the sphere is merely sitting on the rigid substrate. However, if the substrate is softened (e.g. by thermal annealing), the particle becomes embedded to a certain depth (z) until the equilibrium configuration is reached, see Fig. 4.1 (b). The corresponding variation in the surface free energy (F_s) is given as[80]

$$F_s(z) = 2\pi a z \gamma_{12} + 2\pi a(2a - z)\gamma_1 - \pi z(2a - z)\gamma_2, \tag{4.1}$$

where γ_1 and γ_2 are the surface tensions of the sphere and the substrate, respectively, and γ_{12} is the interfacial tension. For a non-embedded particle (see Fig. 4.1 (a)), γ_{12} is governed by[82]

$$\gamma_{12} = \gamma_2 - \gamma_1 \cos(\theta). \tag{4.2}$$

The driving force for embedding is the reduction of F_s, and the equilibrium position of the immersed sphere corresponds to the minimum of the surface free energy ($F_{s,min}$). Hence, by differentiating Eq. 4.1 and setting it equal to zero, the maximum depth (z_{max}) according to $F_{s,min}$ can be determined as

$$z_{max} = \frac{a(\gamma_1 + \gamma_2 - \gamma_{12})}{\gamma_2} = 2a\frac{W_{12}}{W_{22}}. \tag{4.3}$$

Here, $W_{12} = \gamma_1 + \gamma_2 - \gamma_{12}$ is the work of adhesion and constitutes the required work to separate the materials at their interface, while $W_{22} = 2\gamma_2$ is the work of cohesion[80]. Now, a final configuration of a completely embedded sphere requires $z_{max} > 2a$ so that the following condition follows

$$W_{12} > W_{22} \tag{4.4a}$$

$$\gamma_1 > \gamma_{12} + \gamma_2. \tag{4.4b}$$

Thus, if the surface tension of a rigid sphere is larger than the sum of the surface tension of the substrate and the interfacial tension, complete embedding can be expected. In this study, metal NPs are deposited on thin polymer films using cluster beam technique. While metals are crystalline solids with high packing density, noncrosslinked polymers constitute large, covalently bonded macromolecules connected by weak, mostly van der Waals-type interactions, in an open network[83, Ch. 7]. Consequently, metals exhibit high cohesive energies and correspondingly high surface tensions which are typically 2 orders of magnitude larger than the ones of polymers[16, 84]. Hence, Ineq. 4.4 is suspected to be satisfied for these materials and complete embedding of the metal NPs into a polymer film is expected. In fact, full immersion of metal NPs into polymers has already been reported several times[16, 80, 85–87]. However, there are also contradictory publications reporting only partial immersion of the NPs[88, 89]. For instance, Amarandei *et al.*[88] argue that the interaction between the NPs and the substrate below the polymer has to be considered as well for thin polymer films. They implemented the free energy change related to NP-substrate interaction in the calculation of the total free energy change during particle immersion. Based on the theoretical results, they predicted whether the NPs will embed into the polymer or reside on the polymer surface. The experimental results with Au NPs on PS and PMMA films, respectively, showed good agreement with the predictions.

4.2.2. Nanoparticle Embedding as a Probe for Polymer Surface Dynamics

As mentioned before, metal NPs are expected to immerse into polymer films due to the driving force arising from the large difference in the surface tensions of metal NPs and polymers. Furthermore, from the kinetic point of view, embedding requires long-range mobility of the polymer chains which is acquired at the glass transition temperature (T_g). Hence, the onset of the immersion process, which can be experimentally obtained by several techniques, can be used to probe T_g in the near-surface region of polymers. Before some examples are given, it is worth noting that the results have to be treated with care as some studies reveal controversial results. This may be related to a number of factors, e.g. differences in the depth resolutions of applied methods, in the kind of interface (polymer/vacuum or polymer/air), film thickness, the molecular weight (M_w), effects of polymer-substrate interaction, etc.[85, 90].

Faupel *et al.*[85] used X-ray photoelectron spectroscopy (XPS) to monitor in situ the embedding process of Cu and Au NPs (average radii of 1.2 nm) into PS films of about 200 nm thickness. Based on the measured XPS intensity ratio of the main metal lines and the C 1s line ($r = I(\text{metal})/I(\text{C 1s})$), the onset embedding temperature (T^*) could be identified by a considerable change in r. As long-range chain mobility of the polymer occurs at T^* and by definition at T_g, the authors interpreted the onset embedding temperature as an upper limit for the glass transition temperature in the near-surface region. The results revealed a depression of the surface T_g compared to the bulk T_g. This difference between the surface and bulk values was found to increase with M_w up to a value of about 8 K for $M_w \approx 300\,\text{kg/mol}$, before it decreased again with further rising M_w. They explained this observation with intrinisic models for a surface zone of enhanced chain mobility. Furthermore, the authors derived the surface viscosities for different temperatures from isothermal embedding experiments and showed that their values are well below the bulk viscosities. Finally, Faupel *et al.* reported an increasing surface T_g with increasing nominal metal thickness and correspondingly rising cluster size for clusters in the range of 1 nm and 3 nm. They suggested three main reasons for their observation. First, the smaller clusters, which are on a similar scale as the persistence length (distance on which polymer can be considered a freely rotating chain[86]) of PS (1.54 nm[91]), affect the mobility of the polymer much less than the larger ones. Secondly, an increased nominal metal thickness is not only accompanied by larger cluster sizes, but also by a higher surface coverage. In this case, the embedding process does not depict the mobility of the free polymer surface anymore. Finally, as mentioned in the previous subsection, the driving force for immersion of the NPs arises from the difference in the surface tensions of polymers and metal NPs. Since the surface tension of the clusters depends reciprocally on R_c, the driving force for embedding is larger for smaller clusters.

Another method for studying the dynamics in the near-surface region of polymers is based on X-ray reflectivity measurements as it was demonstrated by Weber *et al.*[86]. Using this method, they investigated in situ the embedding process of Au clusters (radii in the range 0.9-1.8 nm) into PS films of 80-100 nm thickness. By evaluating the reflectivity measurements and the near-surface parts of the resulting electron density profiles, Weber *et al.* determined a reduction of the surface T_g by about 37 K (22 K) compared to the bulk value for $M_w = 220\,\mathrm{kg/mol}$ ($M_w = 3.7\,\mathrm{kg/mol}$). Thus, similar to the aforementioned studies of Faupel *et al.*, the reduction of the surface T_g became more pronounced for increasing molecular weight of the polymer. Furthermore, the authors also reported an increase of the embedding temperature with rising cluster coverage which they related to strong short-range metal-polymer interaction that suppresses the kinetics of the NP immersion into the polymer. Therefore, they concluded that embedding of NPs can only be used as a probe of the surface T_g of polymers when the nominal metal layer thickness is sufficiently low.

In general, there is consensus on the reduction of the surface T_g in PS and potentially other polymers. However, the origin is not entirely clear yet although much effort has been put in the study of this phenomenon in the past years. On the basis of simulations, and ellipsometry and embedding studies of Au clusters (10 and 20 nm diameter) into PS films of 180 nm thickness, Forrest *et al.*[92] suggested the existence of a liquid-like layer in the near-surface region of the glassy PS film. This is confirmed in a recent study by Forrest *et al.*[93] in which they produced stepped PS films and employed AFM in order to probe the mobility above and below the bulk T_g. The results indicated a sharp transition from whole-film flow to thin-film flow localized in the surface layer at the bulk T_g and an enhanced mobility of the liquid-like layer. These results are in excellent agreement with an analytic thin-film model which the authors used to describe flow in the surface region. Ediger *et al.*[94] have determined the thickness of the mobile layer at the surface of supported PS and PMMA films. The results revealed an increase of the thickness with the temperature up to about 7 nm for PS and 4 nm for PMMA. They were obtained using a very low concentration of fluorescent probe molecules which were dissolved in the polymer of interest, and by observing the reorientation of these probe molecules with temperature-ramping anisotropy measurements based on photobleaching. Supported by the assumption that the ensemble of probes reflects the segmental dynamics in the polymer, the authors assigned the observed comparatively fast reorientation below the bulk T_g to an enhanced mobility in the near-surface region. The fraction of fast probes could then be converted into the thickness of the mobile layer which was independent of molecular weight, polymer film thickness, and probe identity.

4.2.3. Direct Observation of Nanparticle Embedding into Polymer Melt

As mentioned in the previous subsections, metal NPs are typically observed to immerse completely into polymer films above their glass transition temperature. Deshmukh *et al.*[95] reported direct observation of the immersion of Au NPs (20 nm diameter) into PS films ($\approx$ 500-700 nm thickness) above T_g. Three selected steps of the embedding process are schematically depicted in Fig. 4.2.

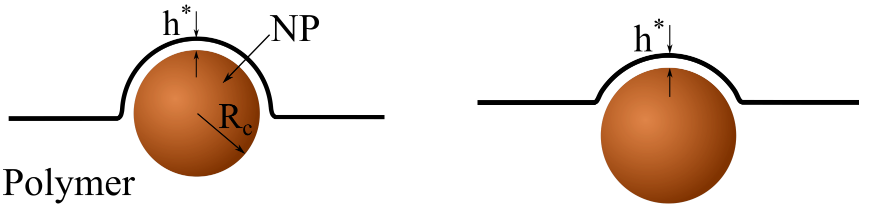

(a) Partially embedded NP.

(b) Nearly completely embedded NP.

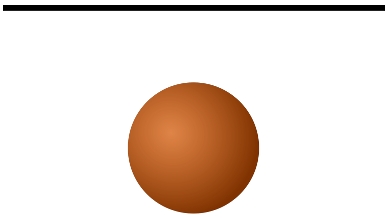

(c) Completely embedded NP.

Figure 4.2. Schematic representation of the embedding mechanism proposed by Deshmukh *et al.*[95].

Employing TEM, Deshmukh *et al.* observed the formation of a polymer wetting layer covering the NP already in the early phase of the immersion process (see Fig. 4.2 (a)) whose thickness stayed constant throughout all stages. They proposed that the curvature of the wetting layer provokes a net capillary pressure $[\gamma_2/(R_c + h^*)]$ driving the NP deeper into the polymer melt until it becomes completely embedded, see Fig. 4.2 (c). Furthermore, the experiments showed that h^* varied only slightly between 1.3 nm for M_w = 6 kg/mol and 1.8 nm for M_w = 900 kg/mol. This independence of h^* on the molecular weight was confirmed by a model which takes the spreading coefficient, long-range van der Waals interactions, and entropic chain stretching into account. Finally, the authors assume the observed formation of a polymer wetting layer to be a generic mechanism occurring during immersion of NPs into a polymer melt.

4.2.4. Kinetics

In order to extract the kinetics from the immersion process, Ruffino *et al.*[87] studied the embedding of Au and Ag NPs into 100 nm thick PS (M_w = 223.2 kg/mol) and PMMA (M_w = 540 kg/mol) films employing AFM. Regarding the sample preparation, the polymer films were spin-coated on Si wafers from $CHCl_3$ solutions and covered with Au and Ag (nominal thickness of 10 nm) by sputtering from metal targets. Due to the aforementioned considerably higher cohesive energy of metals compared to polymers and the relatively weak metal-polymer interaction, metals do not wet polymer surfaces and form clusters in the initial phase of polymer metallization. The four different obtained systems (Ag-Ps, Ag-PMMA, Au-Ps, Au-PMMA) were annealed at constant temperatures above T_g in N_2 environment for up to 3 hours. In between, the samples were analyzed several times using AFM in order to acquire images and information about the surface morphology. Thereby, the authors derived graphs constituting the NP mean height ($<h>$) (averaged over 200 NPs) as a function of annealing time (t_a) for three different annealing temperatures (T_a). The results exhibited a characteristic time at the beginning of the annealing process for which $<h>$ remained constant. Ruffino *et al.* interpreted this initial period as the coating time in which a thin wetting layer covers the NP as it was suggested by Deshmukh *et al.*, see Sec. 4.2.3. As expected, this coating time (t_0) decreased with increasing T_a due to the enhanced mobility of the polymer chains. After the described stage, $<h>$ decreased linearly with t_a until the NPs were completely embedded. Thus, the slope of the linear fit is equal to the embedding velocity (v) which was determined for the different metal-polymer nanocomposites and annealing temperatures. For instance, the coating time and embedding velocity for Ag-PMMA and $T_a = 120\,°\mathrm{C}$ were found to be $t_0 = 3632\,\mathrm{s}$ ($\approx 1\,\mathrm{h}$) and $v = 0.12\,\mathrm{nm/min}$. These results can be compared to the study of Hanif *et al.* who deposited Ag clusters on 25-50 nm thick PMMA films using magnetron sputtering. Here, 10 minutes annealing of the samples in ambient atmosphere at 125 °C already lead to a reduction of $<h>$ from initial 13.4 nm to 5.9 nm. Assuming a linear decrease, this would correspond to an embedding velocity of 0.75 nm/min, i.e. about 6 times the one for Ag-PMMA determined by Ruffino *et al.*. Considering the minor difference in the annealing temperatures, this is a drastic difference which is not expected. Furthermore, the suggested formation of a polymer wetting layer must proceed in much shorter period of time in the latter case, i.e. within seconds or minutes rather than within one hour as reported by Ruffino *et al.*. The origins for these described differences are not clear. Comparing the preparation methods of the samples, a considerably higher mean height of the as-deposited Ag NPs can be found in the study of Ruffino *et al.* ($<h> \approx 21\,\mathrm{nm}$) compared to the experiments of Hanif *et al.* ($<h> = 13.4\,\mathrm{nm}$). As discussed in Sec. 4.2.2, the embedding temperature has been reported to increase with cluster size due to stronger metal-polymer interaction and resulting suppression of the kinetics. Thus, the embedding velocity is expected to be lower for larger clusters. However, this alone may not be sufficient to explain the discrepancy in t_0 and v for the Ag-PMMA nanocomposites in the mentioned studies.

4.3. State-of-the-Art Approaches for Formation of Metal-Polymer Nanocomposites

As introduced in Sec. 4.1, several methods for the formation of metal-polymer nanocomposites already exist which have shown to yield good results. However, in most of the approaches (e.g. co-sputtering or co-evaporation), the formation of metal NPs and polymer matrix proceeds simultaneously, i.e. these processes are coupled. Decoupling of them can be realized by production of the NPs prior to their incorporation in the polymer matrix which allows to control size and amount of NPs independently. The aim of this section is to give an overview of state-of-the-art approaches for the formation of metal-polymer nanocomposites which enable independent control of filling factor and size distribution of the NPs, but also of the properties of the polymer matrix. Compared to the aforementioned wet chemical techniques, the following methods also represent environmentally friendly ways as they do not require the use of any harsh chemical substances.

4.3.1. Deposition of Metal-Plasma Polymer Nanocomposites

In this approach, the metal NPs are first formed separately and then included in the growing polymer matrix which is produced by plasma-enhanced chemical vapor deposition (PECVD). In recent years, Biedermann *et al.* have demonstrated successfully the implementation of this method for the formation of different metal-polymer nanocomposites, e.g. Al-C:H hard plasma polymer[96], Ag-C:H[97], or Cu-nylon[98] nanocomposites. Fig. 4.3 represents a schematic drawing of the experimental setup that Biederman *et al.* have used for one of their latest studies on the formation of Cu-a-C:H nanocomposite films. As can be seen, the Cu NPs are first produced in a water-cooled gas aggregation source (GAS) (working pressure 0.4 mbar) based on magnetron sputtering and then collimated into the deposition chamber (pressure 1.5×10^{-2} mbar) where they are deposited on the simultaneously growing plasma polymer. Using the mixture Ar/n-hexane 4:1, reactive plasma species are first created in the vicinity of the planar radio frequency (RF) electrode which form new stable compounds (plasma chemical gas conversion) that are finally deposited as thin films on the substrate (plasma polymerization)[99]. In contrast to long chains of repeating monomer units in common polymers, plasma polymers constitute short, randomly branched chains with high degree of cross-linking. Their properties can be widely tuned by varying the deposition parameters, e.g. precursor, pressure, working gas mixture, etc.[100]. It should be noted that the terms *plasma polymerization* and *PECVD* both describe the same physical process.

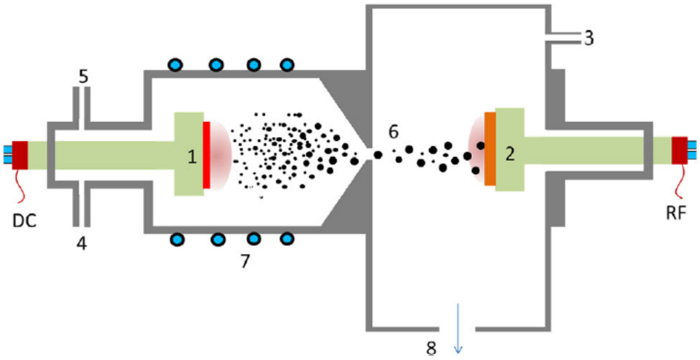

Figure 4.3. Schematic drawing of the experimental setup used by Biederman *et al.* for the formation of Cu-a-C:H nanocomposite films. 1. Moveable DC magnetron for NPs production; 2. RF electrode with substrate holder for a-C:H deposition; 3. Monomer inlet; 4. Ar inlet; 5. Vacuum gauge; 6. Output orifice of GAS; 7. Aggregation chamber with water cooling; 8. Vacuum pumps. Drawing and description are taken from [101].

Regarding the experimental setup depicted in Fig. 4.3, the Cu NPs only reach the substrate when the RF electrode is turned off. Therefore, Biederman *et al.* operated the RF discharge in pulsed regime with duty cycle 50% in order to ensure alternating deposition of a-C:H polymer matrix and Cu NPs. Besides that, they have also used slightly varying experimental setups in other studies, e.g. vertical alignment of GAS and RF magnetron with respect to each other and a rotating substrate holder between GAS and magnetron for simultaneous deposition of plasma polymer and NPs[97]. In a recent study of Biedermann *et al.*[102], they have produced Ag-hexamethyldisiloxane (HMDS) and Ag-SiO_x nanocomposites with multi-layered sandwich structures by moving the substrate between GAS and RF electrode, enabling sequential deposition of plasma polymer matrix and Ag NPs. As demonstrated, the Ag^+ ion release could be tuned by varying the amount of incorporated Ag NPs and the type of used polymer matrix. Thus, the presented method represents an efficient way to produce antimicrobial coatings with adjustable antimicrobial efficiency.

4.3.2. Supersonic Metal Cluster Beam Implantation in Polymer Films

Another recent approach is called supersonic cluster beam implantation (SCBI) which has been demonstrated by Milani *et al.*[17]. As seen from the schematic drawing showing the experimental setup in Fig. 4.4, the (neutral) clusters are first produced in a pulsed microplasma cluster source (PCMS) (for details, see [17]) at high pressure (40 bar) and then expanded through a nozzle into the low pressure (10^{-6} mbar) expansion chamber. Due to the high pressure difference between PCMS and expansion chamber, the cluster beam is accelerated during the supersonic expansion and becomes highly collimated by the aerodynamic focuser. Finally, the central part of the beam passes through the skimmer and enters the deposition chamber (10^{-5} mbar) where it strikes the polymeric substrate on the motorized substrate holder. By displacement of the holder in x- and y-direction the clusters can be uniformly embedded in the polymer.

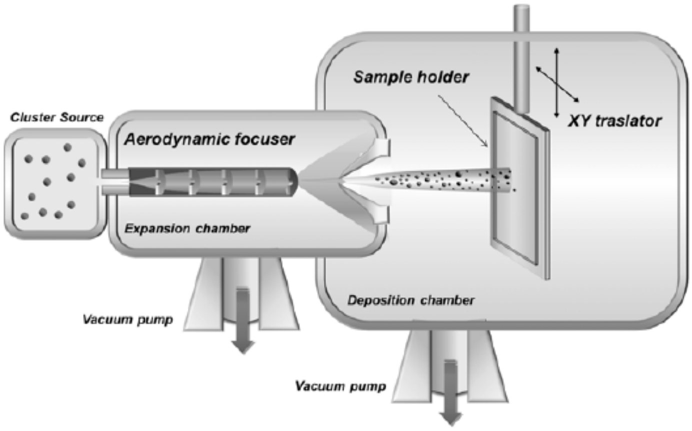

Figure 4.4. Schematic drawing of the experimental setup used by Biederman *et al.* for the formation of Au-PDMS nanocomposites.[17]

During SCBI, the clusters are accelerated to a mean velocity of 1000 m/s which corresponds to a kinetic energy of about $E_{at} = 0.5\,\mathrm{eV}$. This energy is sufficient for the NPs to penetrate the polymer surface and become implanted. In contrast to negative side effects such as electrical charging or carbonization for ion implantation in polymers (see Sec. 4.1.2), this method leaves the polymeric structure largely unaffected after implantation. However, AFM study of surface morphology for Au-PDMS nanocomposites produced by SCBI revealed swelling of PDMS on the order of tens of nm. Furthermore, extensive MD simulations of the implantation process showed that cluster impact leads to local temperature increase and crater formation on the polymer surface with lateral dimensions similar to the cluster radii.

All in all, SCBI represents a promising method for the formation of metal-polymer nanocomposites in a range of applications, e.g. as elastomeric electrodes with improving conductivity upon cyclic stretching[11], or stretchable nanocomposite films with mechanically tunable LSPR[103]. For instance, regarding the latter example, Milani *et al.* have produced Au-PDMS nanocomposites by SCBI and characterized their LSPR evolution during cyclic stretching by measuring the absorbance spectra. Evaluation of those measurements revealed a redshift of the plasmon peak which increased with the elongation up to 180 nm for 50% deformation. The authors ascribed this observation to rearrangement and reorganization of the embedded clusters. Furthermore, prepared samples with Au volume fraction larger than 30% preserved a stable redshift for more than 5000 stretching cycles. Thus, this preparation method can be used to produce stretchable metal-polymer nanocomposites applied as components for stretchable optical devices.

4.3.3. Deposition of Metal Nanoparticles on Polymer Films

The third approach has already been demonstrated by Hanif *et al.*[16] and it can be basically subdivided into three fabrication stages. First, a thin polymer film (e.g. PMMA or PS) is deposited on a substrate which is then transferred into the deposition chamber of the magnetron sputtering cluster apparatus (MaSCA). In the second stage, metal clusters are produced by means of a gas condensation source (working pressure of a few mbar) and deposited on the polymer film under vacuum conditions (10^{-5} mbar). Cluster kinetic energy is kept in the low-energy regime (on the scale of a few meV) so that the clusters almost preserve their spherical shape upon impact on the surface[16, 41]. In the last production phase, the sample is annealed on a hot plate in ambient atmosphere and above the polymer T_g in order that the metal NPs can immerse into the polymer.

In contrast to the two previous methods, only ionized clusters are soft-landed which are size-selected using an electrostatic quadrupole mass selector (EQMS) prior to deposition. Thereby, a narrow cluster size distribution can be achieved which is, however, accompanied by lower deposition rate as only a fraction of all clusters is deposited. Using this preparation approach, Popok *et al.*[14] have produced Ag-PMMA nanocomposites and demonstrated their applicability as transducers for optical sensing of proteins.

In this study, metal-polymer nanocomposites are fabricated using the same preparation method and machines. The controlled immersion of Cu clusters into thin PMMA and PS films is studied and the formation of ordered arrays of Ag NPs on polymethylglutarimide (PMGI) is investigated. Therefore, the fabrication steps and the experimental setup for cluster deposition (MaSCA) will be explained in more detail in Chap. 5.

Chapter 5

Methodology

This chapter is concerned with the experimental work during the project. In particular, preparation of the samples with the corresponding fabrication steps, the magnetron sputtering cluster apparatus for deposition of the metal clusters, and the employed characterization techniques for investigation of the samples are described.

5.1. Materials and Sample Preparation

Three different polymers were used in the experiments: A 9% solution of PMMA in chlorobenzene ($M_w = 950\,000\,\text{g/mol}$, $T_g = 105\,^\circ\text{C}$[16]) purchased from MicroChem, PS ($M_w = 280\,000\,\text{g/mol}$, $T_g = 100\,^\circ\text{C}$ as stated by supplier) provided by Sigma-Aldrich in form of pellets, and a solution of PMGI in cyclopentanone and tetrahydrofurfuryl alcohol (PMGI SF3) obtained from MicroChem ($T_g \approx 190\,^\circ\text{C}$ as specified by supplier, M_w not given). While the PMMA solution was diluted down to 1 vol.% (for Cu-deposited samples) and 1.5 vol.% (for Ag-deposited samples) in chlorobenzene, a 1 wt.% solution of PS was prepared by dissolving of the pellets in toluene and stirring for about 12 hours to ensure a homogeneous mixture. For deposition of metal clusters by means of the MaSCA (see Sec. 5.2), high-purity Cu (99.99%) and Ag (99.99%) sputtering targets, which were both purchased from Goodfellow Cambridge Ltd, were used.

In principal, the experimental work of the project can be subdivided into the preparation of Cu-deposited and Ag-deposited samples. In the first part, Cu NPs were deposited on bare substrates or on polymer-coated substrates towards the formation of metal-polymer nanocomposites. In the second part, Ag NPs were deposited on a patterned surface in order to fabricate ordered arrays of those NPs. In the following, the involved experimental steps for preparation of the samples are described in detail for both parts.

5.1.1. Copper-Deposited Samples

The consecutive experimental steps for preparation of the Cu-deposited samples are schematically shown in Fig. 5.1. The depositions of the polymer films and the metal NPs were carried out on 1 x 1 cm large Si or quartz glass wafers. First, those substrates were thoroughly cleaned by ultrasonic treatment in acetone (5 minutes) and isopropanol (IPA, 2 minutes) followed by baking of the wafers on a hot plate at 150 °C (5 minutes) in order to let remaining IPA evaporate. Next, Cu NPs were either deposited on bare substrates or on polymer-covered substrates. In the latter case, thin polymer films were prepared by spin-coating of the PMMA and PS solutions using a Laurell WS-650S-23NPP/C2/IND spin coater. Subsequently, the PMMA and PS samples were annealed on a hot plate at 100 °C and 95 °C for 5 minutes, respectively, in order to solidify the polymer films and let most of the remaining solvents evaporate.

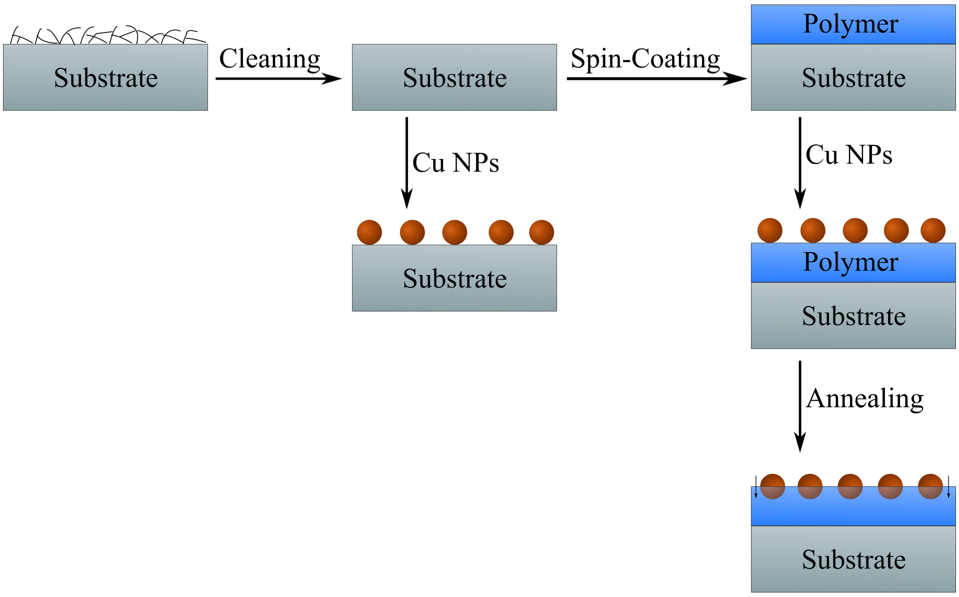

Figure 5.1. Schematic drawing showing the succesive experimental steps for preparation of Cu-deposited samples.

During the spin-coating process, the revolutions per minute were adjusted such that the final thickness of the polymer films was about 50 nm. The film thickness was measured on the Si samples with a spectroscopic ellipsometer (Sentech SE 850) in the spectral range 350-820 nm. For that purpose, a model taking into account the refractive indices of the layers (e.g. Si/PMMA/air) was created which was was then fitted to the experimental data at each wavelength. Since the ellipsometry measurements could not be carried out on the transparent quartz samples, the polymer film thickness was assumed to be the same or very similar compared to the one on the Si substrates. This assumption is most likely valid as the spin-coating parameters were identical for both substrates. After deposition of Cu NPs on the polymer-covered samples using the MaSCA, the samples were annealed on a hot plate for 5 minutes above the respective glass transition temperature (T_g) of the polymer so that the NPs immersed into the polymer. Some samples were also treated in ozone environment using an UV ozone cleaner from Bioforce Nanosciences. The specific treatments of the different Cu-deposited samples will be listed in Sec. 6.1.1. Before and after the treatments, the samples were characterized utilizing AFM (see Sec. 5.3.1) and OS (see Sec. 5.3.2).

5.1.2. Silver-Deposited Samples

As outlined above, the second part of the experimental work dealt with the fabrication of ordered arrays of Ag NPs. The involved experimental steps are schematically shown in Fig. 5.2. As with the preparation of the Cu-deposited samples, the substrates (same substrates, i.e. 1 x 1 cm large Si and quartz glass wafers) were first cleaned using the same procedure.

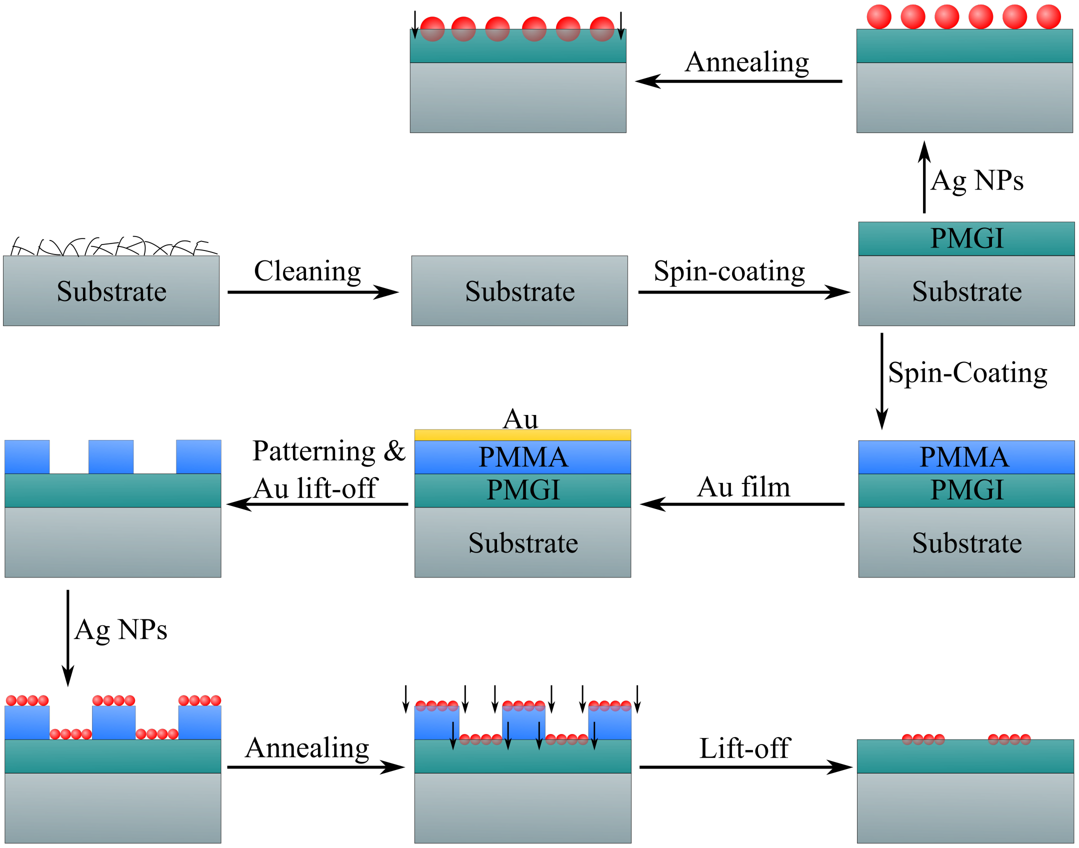

Figure 5.2. Schematic drawing showing the succesive experimental steps for preparation of ordered arrays of Ag NPs.

Then, either of two preparation processes was executed, see Fig. 5.2. In the first one, Si substrates were covered with a PMGI film of about 100 nm thickness by spin-coating of the solution. Afterwards, the samples were baked on a hot plate at 190 °C for 5 minutes. Next, they were transferred to the deposition chamber of the MaSCA in order to deposit Ag NPs on the polymer films. Subsequent annealing of the samples around the T_g of PMGI ($\approx$ 190 °C) should facilitate immersion of the NPs into the polymer which was studied using AFM.

The other preparation process was intended for the formation of stripes of Ag NPs, see Fig. 5.2. For this purpose, a PMGI (100 nm thickness) and a PMMA (110 nm) layer were spin-coated consecutively on quartz substrates which were subsequently annealed at 190 °C for 5 minutes. Next, a 10 nm thick Au layer was deposited on the samples by e-beam evaporation using a Cryofox Explorer PVD coater. This step was necessary in order to avoid charge accumulation on the sample surface during the following electron beam lithography (EBL). For EBL, a Zeiss 1540 XB scanning electron microscope (SEM) was used in combination with the lithography system Raith Elphy Plus to create the desired pattern and carry out the e-beam writing. The SEM was operated with acceleration voltage of 20 kV and aperture size of 20 µm. After EBL, the Au layer was removed using a gold etchant (ca. 15 s), and the samples were developed in a mixture of methyl isobutyl ketone (MIBK) and IPA (1 minute, molar ratio 1:1) and subsequently rinsed in IPA (30 seconds) to stop dissolution of the exposed PMMA. As depicted in Fig. 5.3, a 2 x 2 mm pattern was created in the center of each sample, consisting of ca. 120 nm wide PMGI trenches separated by PMMA layers with lateral dimensions varying between 150-400 nm depending on the sample. The specific dimensions will be given for each sample in Sec. 6.3.1.

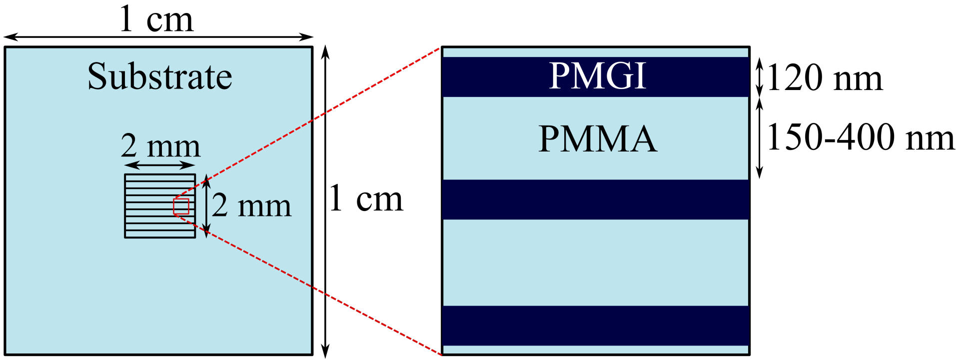

(a) Top view.

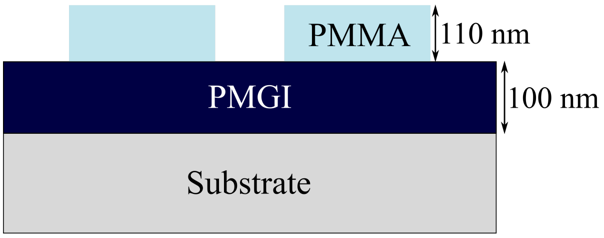

(b) Side view.

Figure 5.3. Schematic drawing of the sample with given dimensions of the structures after EBL and devoloping.

After fabrication of the patterns on the polymer films, the samples were transferred to the deposition chamber of the MaSCA for deposition of Ag NPs for which a surface coverage of about 1 monolayer (ML) was aimed. Thereafter, the samples were annealed at 190 °C to enable immersion of the NPs into the polymer films and, thus, enhance adhesion of the NPs. In the final step, the samples were first treated in acetone at 60 °C followed by an ultrasonic bath in acetone (see Tab. 6.4 for details about lift-off conditions of the specific samples). During this lift-off, PMMA was dissolved and removed so that the samples were left with the acetone-resistant PMGI film covered with stripes of Ag

NPs in the sample center, see last panel in Fig. 5.2.

5.2. Magnetron Sputtering Cluster Apparatus

For deposition of Cu and Ag clusters on the prepared substrates, the magnetron sputtering cluster apparatus (MaSCA) was used. A schematic top view of the MaSCA is depicted in Fig. 5.4. It should be noted that the ion optics in the source chamber were not used for focusing of the cluster beam. Instead, an Einzel lens was employed to focus the beam after mass-selection by the electrostatic quadrupole mass selector (EQMS).

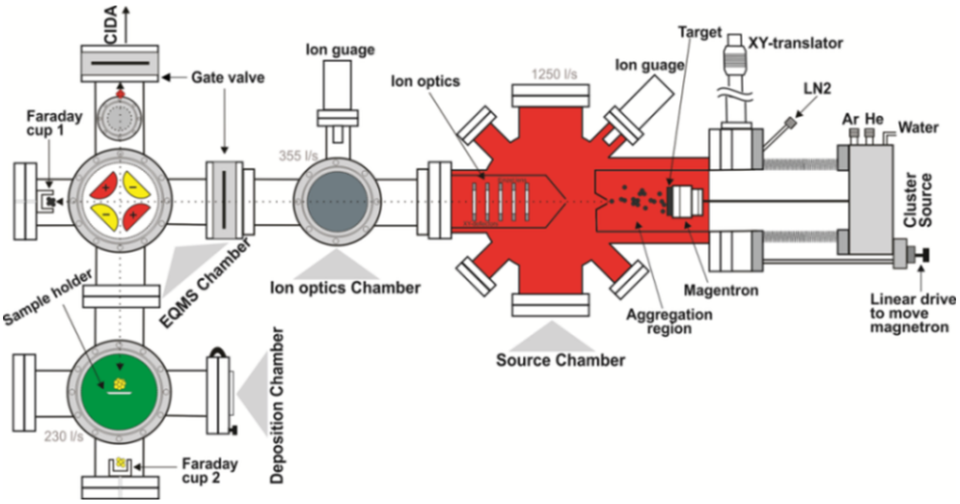

Figure 5.4. Schematic top view of the MaSCA.

This section is intended to overview the experimental execution and settings during operation of the MaSCA. For details about the different parts of the apparatus and their working principles, the reader is referred to [41, 104]. In brief, the processes of cluster formation, size selection, and deposition were executed as follows: In the presence of the sputter and aggregation gases (Ar and He), metal atoms were sputtered in a DC magnetron (equipped with the target) which then nucleated and formed clusters in the aggregation region (see Sec. 2.1.1 for the theory). The nucleation process was facilitated by cooling of the gases using liquid N_2, leading to a temperature of about $-20\,^{\circ}\mathrm{C}$ in the cluster source. Due to the pressure difference between aggregation region (a few mbar) and source chamber (operation pressure 10^{-3} mbar), the formed clusters were then expanded through the nozzle into the source chamber (subsonic expansion) where the cluster beam was collimated by the skimmer. Since a high fraction of the clusters was ionized, an EQMS was employed to select the charged clusters according to their mass (size). Variation of the applied voltage to the EQMS (U_{QP}) and the polarity of the pairs of electrodes enabled to select the size and the charge of the clusters (cations or anions) which were deflected by 90° and finally deposited on the sample in the deposition chamber (operation pressure 10^{-5} mbar). By modification of the voltage applied to the Einzel lens (U_L), which is placed between EQMS and sample holder, the beam could be focused on a small spot or spread over the entire sample to ensure homogeneous coverage. Two samples were mounted on the sample holder whose position could be controlled in x-, y-, and z-direction using a linear translator. Thus, the position of the sample holder with respect to the cluster beam could be easily switched between samples (for cluster deposition) and ion current measurements with a Faraday cup in order to monitor the beam intensity.

Generally, a high beam intensity is favorable as this enables higher deposition rate and, thus, more time-efficient cluster deposition. Therefore, the intensity was maximized prior to each deposition by variation of He and Ar gas flows, magnetron power, and aggregation length (distance between target surface and nozzle). Those parameters were not identical for each deposition, but varied considerably so that it was not possible to create "recipes" for optimal beam intensity at each applied U_{QP}. However, the experiments revealed a tendency to increasing Ar/He gas flow ratio and increasing aggregation length for increasing cluster sizes. The surface coverage on the samples could be controlled via variation of the deposition time, i.e. the coverage increased with deposition time. Finally, only negatively charged clusters were deposited.

5.3. Characterization Techniques

The prepared samples were characterized using atomic force microscopy (AFM) and optical spectroscopy (OS). In the following, these characterization techniques will be shortly introduced along with description of experimental details.

5.3.1. Atomic Force Microscopy

AFM, introduced by Binnig *et al.*[105] in 1986, is a powerful tool to examine the surface topography of materials with high resolution on the order of fractions of a nm. Its working principle is based on the scanning of the sample surface with a probe made of an elastic cantilever with a sharp tip at the end, and the resulting interactive force between tip and surface. Depending on the utilized SPM mode, the interactive forces can be of different nature, e.g. chemical bonding, magnetic, electrical, or van der Waals forces, and they lead to bending of the cantilever. The cantilever deflection can then be measured to acquire the topography of the sample during the scanning process. In many cases, AFM measurements are based on the van der Waals force and the tip-surface interaction can be approximated by the Lennard-Jones potential which is given as[106]

$$U_{LJ} = U_0 \left[-2 \left(\frac{r}{r_0} \right)^6 + \left(\frac{r}{r_0} \right)^{12} \right], \tag{5.1}$$

where r is the distance between the outmost atom of the tip and the surface atom, and U_0 is the minimum energy corresponding to the equlibrium distance (r_0) between the atoms. The first term of the sum describes the attractive van der Waals forces having dipole nature (for large r), while the second term considers repulsion due to overlapping of electron shells of atoms for short r (Pauli exclusion principle). As depicted in Fig. 5.5, there are three common methods which can be used to acquire AFM images: contact mode (repulsive regime of U_{LJ}), semi-contact or tapping mode (repulsive and attractive regime), and non-contact mode (attractive regime).[106]

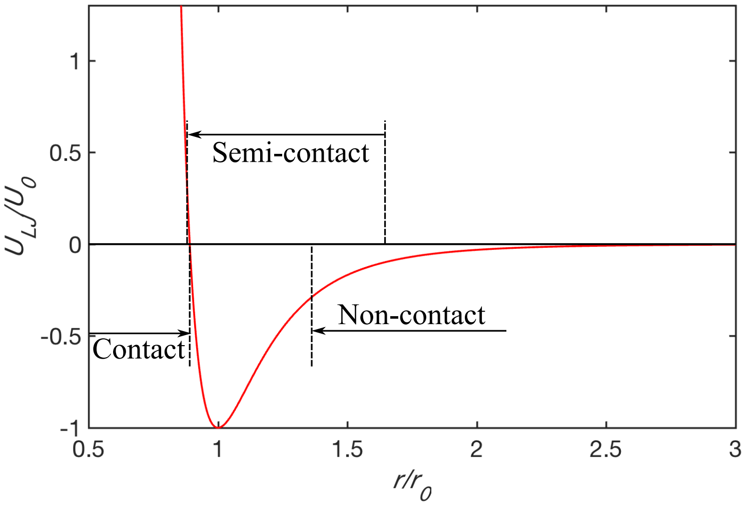

Figure 5.5. Lennard-Jones potential as a function of interatomic distance, and the three interaction regimes.

In the current work, the samples were analyzed by AFM using Ntegra Aura nanolaboratory (from NT-MDT) in tapping mode. In tapping mode, the cantilever is excited by a piezo element to oscillate near its resonance frequency. During the bottom swing, the tip gets in contact with the surface (tapping) corresponding to the repulsive regime, while the top swing corresponds to the attractive regime. A crucial parameter for appropriate sample acquisition is the set point which controls the contribution of repulsive force to the tip-surface interaction. In this project, the set point was adjusted for each measurement depending on resonance frequency of the cantilever and hardness of the sample surface (e.g. polymer-covered or bare Si substrate). During scanning, amplitude and phase changes of the cantilever were recorded and processed by the system, and translated into height and phase images. While the height images revealed information about surface coverage, height distribution of the metal clusters, and the arrangement of the clusters on the surface (e.g. tendency to form aggregates), the phase images could give additional information about material properties of the sample surface. For further details about AFM and tapping mode, see [106]. The measurements were carried out in ambient atmosphere. Commercial cantilevers, having resonance frequencies between 70-400 kHz, with sharp Si tips (radius of curvature $< 10\,\mathrm{nm}$) were used. For analysis and editing of the AFM images, the program *Image Analysis* from NT-MDT was employed. Furthermore, a MATLAB script was used to compare the height distributions of all particles on the polymer-covered substrates before and after annealing of the samples, see App. B.

5.3.2. Optical Spectroscopy

In general, OS deals with measurement of transmittance (temporarily denoted as T), absorptance (A), and reflection of light within the spectral range 200-1500 nm (UV-VIS-NIR)[107]. In this project, a Perkin Elmer Lambda 1050 UV/VIS/NIR spectrometer was employed to carry out transmittance measurements on the prepared quartz samples. In the first step, a reference beam was used which directly encountered a photodetector in order to collect the transmittance values (100%) at each wavelength within the selected range. Then, a test beam with identical properties as the reference beam passed the sample and encountered the photodetector which measured the irradiance at each wavelength. By comparison with the collected values of the reference beam, the transmittance values for the sample were obtained for each wavelength. The transmittance measurements were carried out on quartz substrates (either bare or covered with thin polymer film, see Sec. 5.1) both with ($T_{cluster+substrate}$) and without ($T_{substrate}$) soft-landed metal clusters in order to determine the relative absorptance (A_{rel}) according to

$$A_{rel} = (1 - T_{cluster+substrate}) - (1 - T_{substrate}). \tag{5.2}$$

As already mentioned in Sec. 2.3.3, the NPs do not only absorb light, but also scatter it. Therefore, A_{rel} constitutes both absorption and scattering contributions and will be called relative extinction from now on. Finally, it should be noted that the measurements on Cu-deposited samples were carried out in the wavelength range 350-800 nm, while the spectrum for Ag-deposited varied between 250-1400 nm depending on the investigated sample. In addition, the measurements on the samples with ordered arrays of Ag NPs were executed using linearly polarized light. The specific polarization (i.e. s- or p-polarized light) for each sample will be given in Sec. 6.3.2.

CHAPTER 6

Results and Discussion

In this chapter, the results of the experiments are presented and discussed both for the Cu-deposited and Ag-deposited samples. In particular, immersion of the Cu NPs into thin polymer films is thoroughly discussed together with the accompanied evolution of the plasmonic properties, while the produced ordered arrays of Ag NPs are examined regarding their overall quality and plasmonic properties.

6.1. Samples and Experimental Parameters

Prior to the presentation and discussion of the results, this section is designated to give an overview of the prepared samples with the corresponding parameters used during operation of the MaSCA. Furthermore, additional information about the post-deposition treatment of the Cu-deposited samples and the lift-off conditions for the Ag-deposited samples is given. The specified sample labeling given in the Tabs. 6.1 and 6.3 will be used throughout the entire thesis.

6.1.1. Copper-Deposited Samples

In Tab. 6.1, the MaSCA parameters during deposition of the Cu NPs are listed for the respective samples.

Table 6.1. Tabular overview of experimental parameters during operation of the MaSCA for the Cu-deposited samples. U_{QP} and U_L are voltages applied to the EQMS and electrostatic lenses, respectively, I_{cl} is the measured average cluster current, and t_{dep} is the deposition time.

Sample	U_{QP} [V]	U_L [V]	I_{cl} [pA]	t_{dep} [min.]
Si+PMMA+Cu (Cu01)	±500	−490	≈ −105	8
Quartz+PMMA+Cu (Cu02)	±500	−560	≈ −67	10
Quartz+PMMA+Cu (Cu03)	±500	−460	≈ −88	15
Quartz+PS+Cu (Cu04)	±500	−460	≈ −138	30
Quartz+PS+Cu (Cu05)	±500	−460	≈ −75	40
Si+PMMA+Cu (Cu06)	±500	−470	≈ −15	17
Quartz+Cu (Cu07)	±1000	−890	≈ −64	12

Sample	U_{QP} [V]	U_L [V]	I_{cl} [pA]	t_{dep} [min.]
Quartz+Cu (Cu08)	± 1000	-900	≈ -15	35
Quartz+PS+Cu (Cu09)	± 1000	-900	≈ -21	45
Quartz+Cu (Cu10)	± 1000	-900	≈ -18	35
Quartz+Cu (Cu11)	± 1000	-890	≈ -25	26
Quartz+PS+Cu (Cu12)	± 1000	-900	≈ -15	46

The post-deposition treatment of selected samples is specified in Tab. 6.2. As already mentioned in Sec. 5.1.1, the samples were treated in ozone environment and/or thermally annealed on a hot plate. When both treatments were carried out on one sample, ozonation was always executed first.

Table 6.2. Tabular overview of the post-deposition treatment of the Cu-deposited samples. Values separated by arrows depict the successive ozonation times (t_{oz}), and the consecutive annealing temperatures (T_a) with the corresponding annealing times (t_a).

Sample	t_{oz} [min.]	T_a [°C]	t_a [min.]
Cu02	/	$125 \rightarrow 125 \rightarrow 180$	$5 \rightarrow 5 \rightarrow 5$
Cu03	/	$125 \rightarrow 125 \rightarrow 180$	$5 \rightarrow 5 \rightarrow 5$
Cu04	/	125	5
Cu05	/	$90 \rightarrow 90$	$5 \rightarrow 5$
Cu06	/	$125 \rightarrow 125 \rightarrow 125 \rightarrow 125 \rightarrow 125$	$5 \rightarrow 5 \rightarrow 10 \rightarrow 20 \rightarrow 20$
Cu07	/	$100 \rightarrow 100 \rightarrow 120 \rightarrow 120$	$5 \rightarrow 5 \rightarrow 5 \rightarrow 5$
Cu09	/	120	1
Cu10	$10 \rightarrow 15 \rightarrow 20$		
Cu11	20	$120 \rightarrow 120 \rightarrow 120 \rightarrow 120 \rightarrow 120$	$5 \rightarrow 5 \rightarrow 5 \rightarrow 5 \rightarrow 5$
Cu12	20	$120 \rightarrow 120$	$5 \rightarrow 5$

6.1.2. Silver-Deposited Samples

The MaSCA parameters for the deposition of Ag NPs are listed in Tab. 6.3 for the respective samples.

Table 6.3. Tabular overview of experimental parameters during operation of the MaSCA for the Ag-deposited samples.

Sample	U_{QP} [V]	U_L [V]	I_{cl} [pA]	t_{dep} [min.]
Quartz+PMGI+Ag (Ag01)	± 800	-670	≈ -68	6
Quartz+PMGI+Ag (Ag02)	± 800	-670	≈ -60	8
Quartz+PMGI+PMMA+Ag (Ag03)	± 800	-670	≈ -59	5
Quartz+PMGI+PMMA+Ag (Ag04)	± 800	-670	≈ -20	20
Quartz+PMGI+PMMA+Ag (Ag05)	± 800	-670	≈ -10	35

The post-deposition treatment of the samples is summarized in Tab. 6.4. As already described in Sec. 5.1.2, all samples were annealed at 190 °C to facilitate immersion of Ag NPs into PMGI. Regarding the lift-off, the samples were first submerged in acetone at 60 °C for several minutes (t_{ac}) followed by an ultrasonic bath in the same heated acetone (t_{us}).

Table 6.4. Tabular overview of the post-deposition treatment of the Ag-deposited samples. In case that a second lift-off was carried out on the same sample, the corresponding parameters are given in brackets.

Sample	t_a [min.]	t_{ac} [min.]	t_{us} [min.]
Ag01	2	/	/
Ag02	5	/	/
Ag03	2	8 (8)	1 (3)
Ag04	2	10	3
Ag05	3	10	1

6.2. Copper-Deposited Samples

In this section, the results obtained from AFM and OS measurements on the Cu-deposited samples are presented and discussed.

6.2.1. Atomic Force Microscopy

Cluster Size Selection

In order to examine the cluster height dependence on the EQMS voltage (U_{QP}) and precision of the size selection, a series of Cu_N depositions on Si substrates was performed using the MaSCA, in which U_{QP} was increased stepwise. From AFM measurements on the samples, the correlation between cluster mean height ($<h>$) and U_{QP} was determined. The obtained data are listed together with the absolute and relative standard deviations for the respective values of $<h>$ in Tab. 6.5.

Table 6.5. Tabular overview of the measured Cu cluster mean heights with their standard deviations and the respective EQMS voltages.

U_{QP} [V]	100	250	500	750	1000	1250	1500	2000	2500	2900
Mean height [nm]	7.7	11.5	14.2	18.2	19.6	20.8	21.4	23.4	26.1	29.2
Abs. std. dev. [nm]	0.7	0.8	0.9	1.1	1.6	1.7	1.6	2.0	2.0	2.6
Rel. std. dev. [%]	9.5	7.3	6.1	5.9	8.3	8.0	7.4	8.7	7.6	8.9

Fig. 6.1 shows the resulting graph with the measured data and a nonlinear fit carried out with MATLAB. The error bars indicate the absolute standard deviations for each measurement.

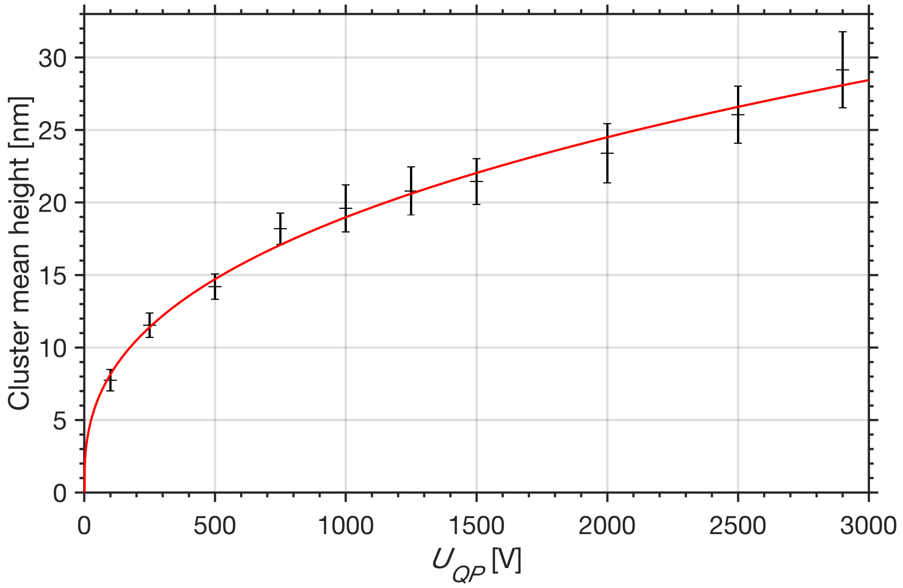

Figure 6.1. Measured Cu cluster mean height as a function of applied EQMS voltage. The fitting curve follows roughly $(U_{QP})^{1/3}$ law. The error bars show the absolute standard deviations.

As can be seen in Fig. 6.1, the fitting curve shows good agreement with the measured data and roughly follows $(U_{QP})^{1/3}$ dependency. Furthermore, the absolute values of the standard deviations increase with rising U_{QP}. As an example, the cluster height distributions for a low ($U_{QP} = 250\,\mathrm{V}$) and a high ($U_{QP} = 2500\,\mathrm{V}$) applied EQMS voltage are shown in Fig. 6.2.

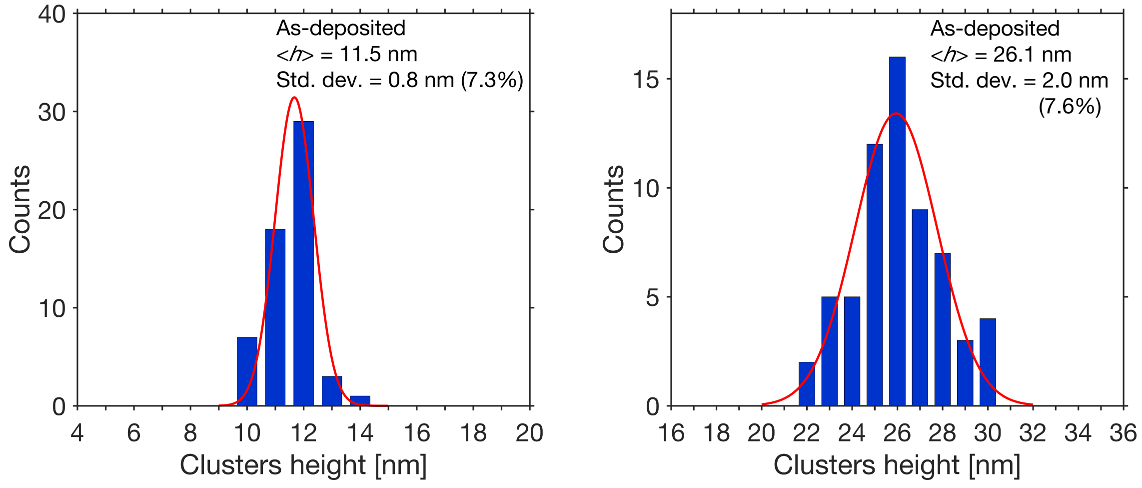

(a) $U_{QP} = 250\,\mathrm{V}$. **(b)** $U_{QP} = 2500\,\mathrm{V}$.

Figure 6.2. Height histograms of Cu clusters on Si for low and high U_{QP}, fitted with Gaussian distributions.

It can be seen that the absolute standard deviation is considerably higher for the larger clusters selected with higher voltage, indicated by a wider Gaussian distribution. However, the relative standard deviations are very similar with values around 7.5%. Over the entire range of applied EQMS voltage, the relative standard deviations of the cluster height stay more or less constant and vary only between 6.0-9.5%. Thus, the size selection of the employed MaSCA is reasonably good and stays constant irrespective of U_{QP} with a ±6.0-9.5% precision of the height. Similar results of the size selection of the EQMS have already been presented for Ag clusters on Si ($\approx 7.0\%$) using the same cluster source (see [16]), thus, confirming the reliability of size selection for different metals.

Deposition of Clusters on Polymer Films

In order to investigate the focusing capability of the MaSCA and the cluster size selection on polymer films, Cu clusters (Cu01) were soft-landed on PMMA applying a relatively high absolute voltage ($U_L = -490\,\mathrm{V}$, see Tab. 6.1) to the electrostatic lenses. AFM images taken in the center and at the edge of the sample are presented in Figs. 6.3 (a) and 6.3 (b), respectively.

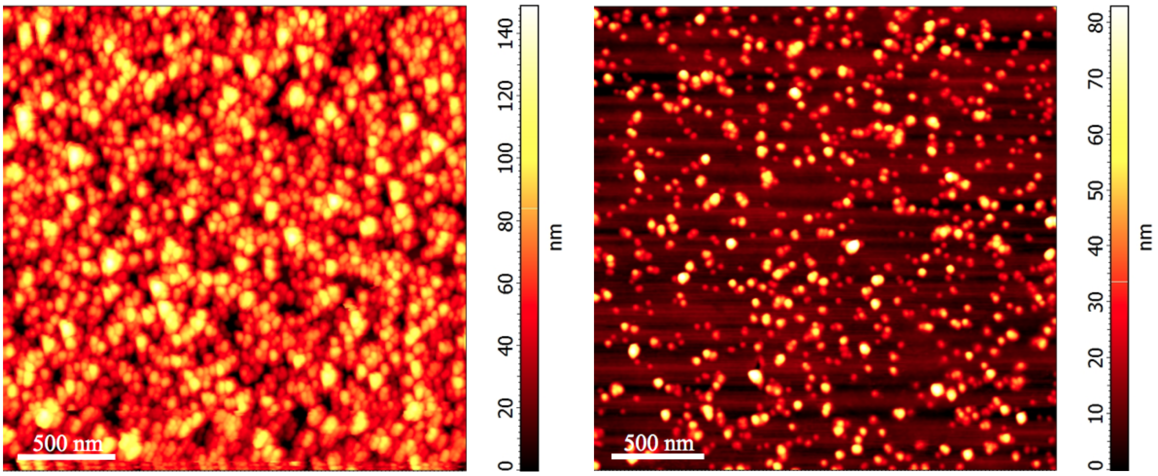

(a) Sample center.

(b) Sample edge.

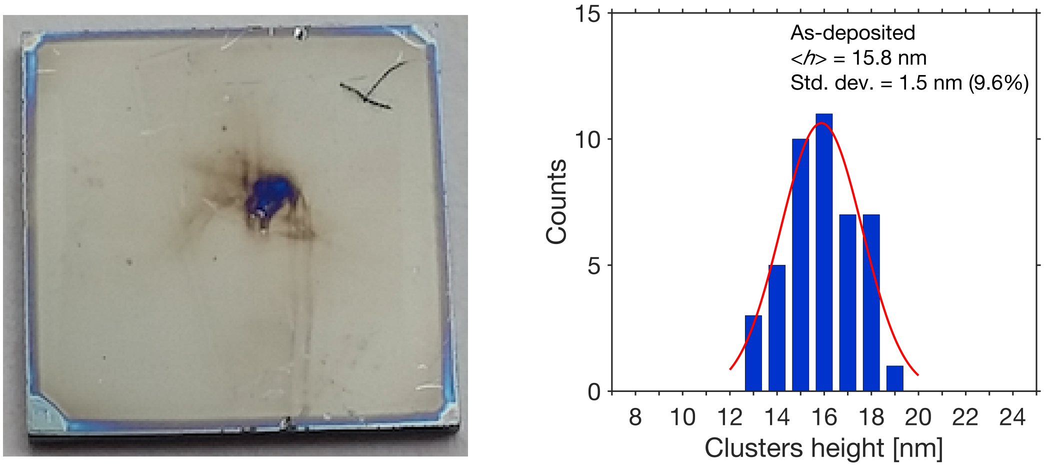

(c) Picture of sample.

(d) Height histogram.

Figure 6.3. AFM images of as-deposited Cu NPs on PMMA taken (a) in the center and (b) at the edge of the sample (Cu01) reveal regions of clearly different surface coverage. (c) A picture of the sample shows a dark spot of about 2 x 2 mm in the sample center, indicating strong focusing of the cluster beam on this area. (d) The height histogram corresponds to the individual clusters measured in (b).

It can be clearly seen that the surface coverage is considerably higher in the sample center, with about 1-2 MLs, while it is well below a ML at the sample edge. Thus, the MaSCA is capable of focusing the cluster beam onto a small area of the sample for an increased absolute lens voltage (U_L). This is confirmed by a picture of the sample (Fig. 6.3 (c)) taken after cluster deposition, which shows a dark spot of about 2 mm diameter in the center that corresponds to the are area of increased coverage. Conversely, the cluster beam could be spread over a larger region of the sample, e.g. when a more uniform coverage is required, by reduction of U_L. The height histogram in Fig. 6.3 (d) was obtained from height measurements of the individual NPs, i.e. aggregates were excluded. The determined mean height of 15.8 nm with the corresponding standard deviation of 1.5 nm agrees with the expected values presented in Fig. 6.1 and confirms the reasonably good size selection. While AFM enabled precise measurement of cluster height, the lateral diameter of the clusters could not be determined accurately as tip convolution effects increased the apparent lateral dimensions of the particles. However, as already mentioned in Sec. 3.1, the soft-landed NPs are assumed to preserve almost spherical shape as previously reported by Hanif *et al.*[16]. Therefore, the lateral diameter is presumed to be only slightly larger than the cluster height.

In Fig. 6.4, an AFM image and the corresponding height histogram with Gaussian fit for Cu NPs deposited on PMMA (Cu02) are shown. Similar to Cu01, the mean height accords well with the determined value for $U_{QP} = \pm 500\,\mathrm{V}$ given in Fig. 6.1, while the relatively narrow Gaussian distribution confirms good size selection of the clusters.

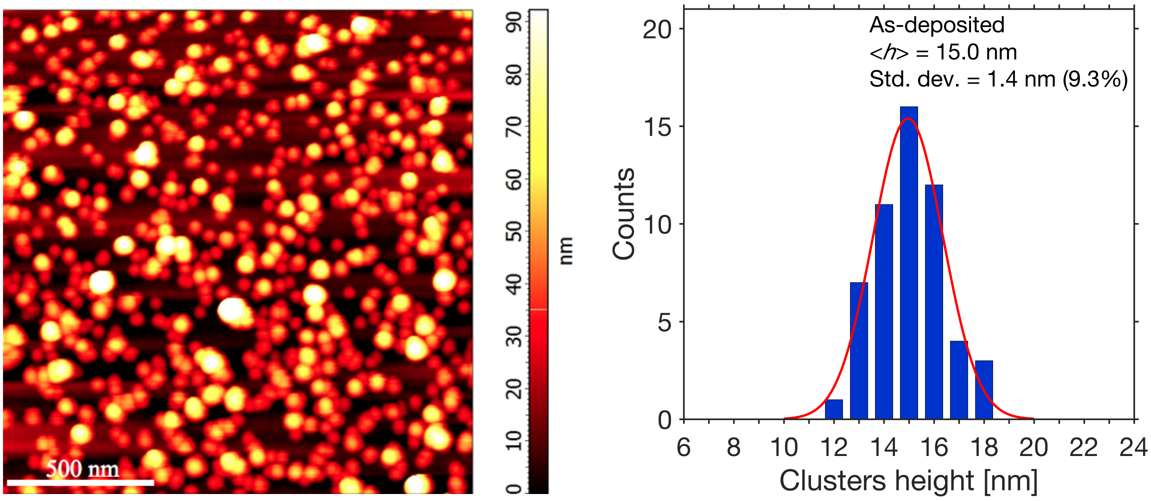

(a)

(b)

Figure 6.4. (a) AFM image of as-deposited Cu NPs on PMMA (Cu02) and (b) corresponding height histogram with Gaussian fit.

The surface coverage is ca. 0.5 ML, and some aggregates of NPs can be seen on the surface of PMMA. They could have either been formed prior to (e.g. in the aggregation region of the MaSCA) or after deposition and diffusion on the surface. Naturally, formation of aggregates is enhanced for higher coverage and thus lower interparticle distances since the particles have to diffuse a shorter distance until they encounter another particle. For instance, the AFM image of Cu01 in the region of high coverage (see Fig. 6.3 (a)) reveals an increased number of aggregates on the surface compared to the AFM image of Cu02. Regarding the AFM image of Cu02, it is also conspicuous that the cluster size seems to increase from the top to the bottom of the image, accompanied by an overall worsened quality (blurry image). This is probably related to a decreasing sharpness of the cantilever tip during the top down scanning of the sample.

Besides the deposition on PMMA films, Cu clusters were also soft-landed on thin films of PS. In Fig. 6.5, an AFM image of as-deposited Cu NPs on PS and the corresponding height histogram are presented.

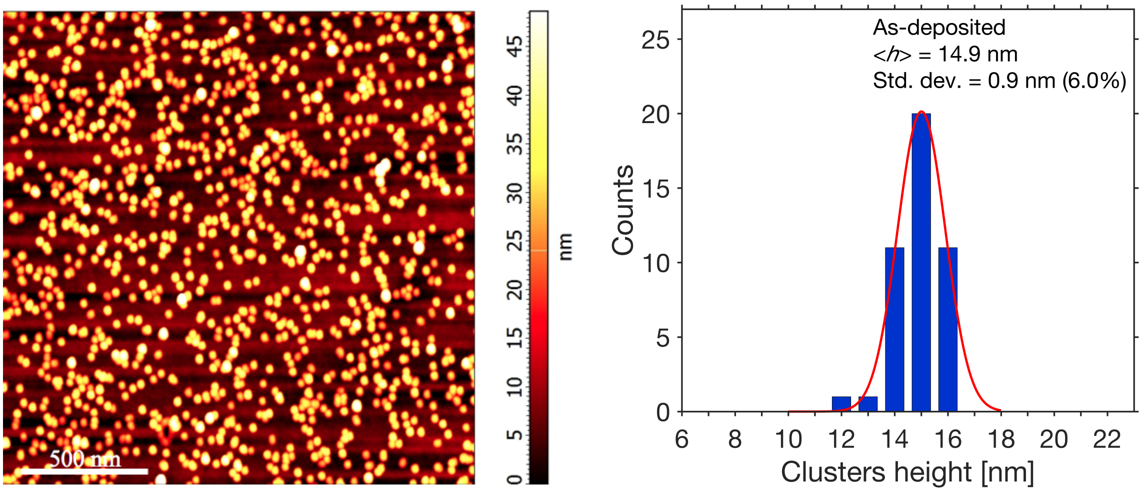

(a) **(b)**

Figure 6.5. (a) AFM image of as-deposited Cu NPs on PS (Cu04) and (b) corresponding height histogram with Gaussian fit.

Again, $<h>$ lies within the calculated error for $U_{QP} = \pm 500\,\mathrm{V}$ (cf. Tab. 6.5 and Fig. 6.1), and the narrow Gaussian distribution confirms good size selection for the clusters ($\pm 6\%$). Comparing the AFM images of Cu02 and Cu04, a similar coverage of about 0.5 ML can be seen. Considering the high cluster current and relatively long deposition time for both samples (see Tab. 6.1), this is a surprisingly low coverage. For instance, the deposition of clusters on Cu04 was carried out with the highest beam intensity of all samples, and the deposition time was about four times the one used for Cu01 which exhibits high coverage in the center region. Albeit the cluster beam was focused more strongly for Cu01 (higher absolute U_L), more than a ML of NPs would be expected for Cu02 and Cu04. Both Cu02 and Cu04 have in common that the deposition of the polymer films and clusters was carried out on quartz substrates instead of Si. In fact, the described phenomenon of low coverage was observed for all polymer-covered quartz substrates. The origin is not clear. It may play a role that quartz glass is a dielectric material, i.e. a bad electrical conductor. During operation of the MaSCA, deposition of the charged cluster ions could lead to accumulation of static electric charge on the substrate. Hence, further incoming clusters may become deflected and the formation of high coverage would be prevented. Additional depositions on polymer-covered quartz substrates suggested a method which could be used to obtain higher coverage. After the first deposition resulting in low coverage, the sample was unloaded and stored in ambient atmosphere for several hours. Then, a second deposition was conducted which lead to considerably higher coverage on the sample. It is supposed that the storage in ambient atmosphere efficiently removes most of the static charge, thus, enabling a more efficient second deposition. However, it remained challenging to obtain high coverage on polymer-covered quartz substrates and further investigations are required to solve the problem.

Immersion of Clusters into Polymer Films

After deposition of Cu clusters on the polymer-covered substrates, the samples were thermally annealed above the polymer T_g in order to enable immersion of the NPs into the polymer films (see Tab. 6.2 for annealing conditions of the respective samples). In Fig. 6.6, AFM images of Cu02 with Cu NPs on PMMA before and after annealing are presented.

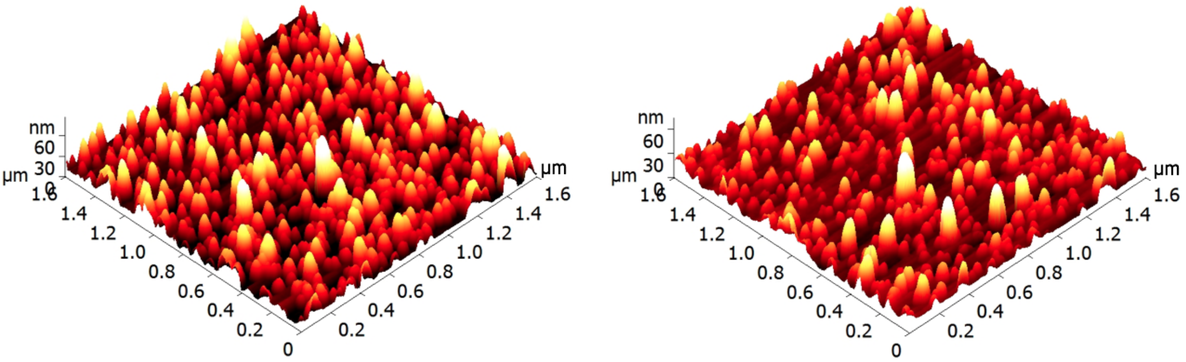

(a) As-deposited.

(b) After 1st annealing.

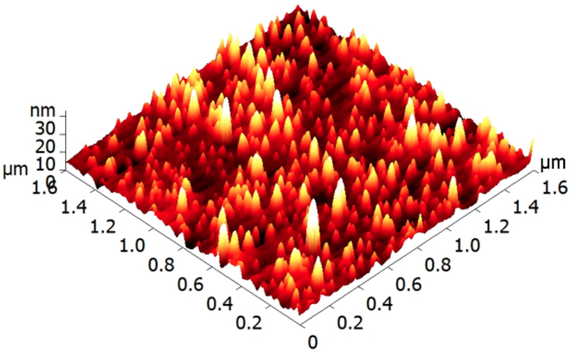

(c) After 3rd annealing.

Figure 6.6. AFM images of Cu NPs on PMMA (Cu02) (a) before and (b)-(c) after thermal annealing.

After first annealing at 125 °C, some NPs are partially embedded, while larger aggregates still clearly protrude from the polymer surface. The particles are further immersed after third annealing at even higher temperature (180 °C), however, it cannot be clearly seen whether some NPs are fully embedded. The immersion of the clusters is confirmed by the height distributions of the Cu clusters before and after thermal annealing, which are shown in Fig. 6.7.

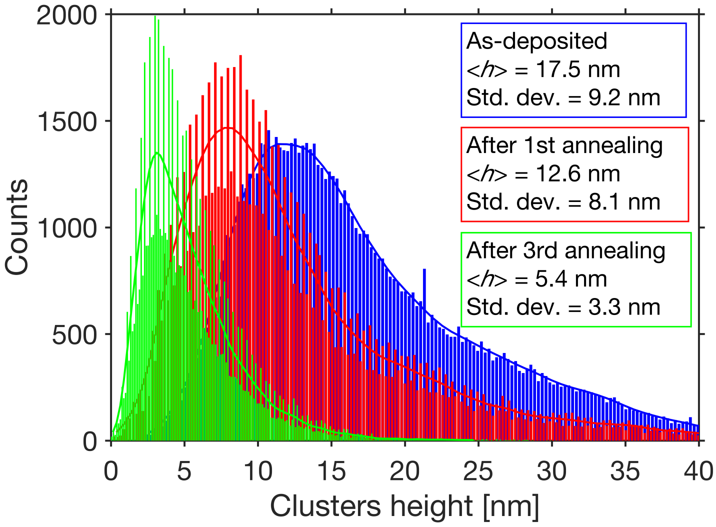

Figure 6.7. Height distributions of Cu NPs on PMMA (Cu02) before and after thermal annealing.

For the calculation of the respective mean heights and plotting of the height distributions, a MATLAB script was used, see App. B. According to the calculation, $<h>$ decreased from 17.5 nm for as-deposited NPs to 12.6 nm after first annealing and finally 5.4 nm after third annealing. As discussed in Sec. 4.2.2, the immersion process requires long-range mobility of the polymer chains, which is acquired at the glass transition temperature (T_g). Since the sample was annealed at temperatures way above the T_g of PMMA (105 °C), this condition was fulfilled. As already addressed in Sec. 4.2.1, the driving force for the immersion is the reduction of the surface free energy (F_s). Recalling Eq. 4.3 for the maximum embedding depth (z_{max}) of a rigid particle in a soft substrate

$$z_{max} = \frac{a(\gamma_1 + \gamma_2 - \gamma_{12})}{\gamma_2}, \tag{6.1}$$

it can be inferred that z_{max} increases with increasing difference in the surface tensions of the particle (γ_1) and the substrate (γ_2). In the literature, values of $\gamma_1 \approx 1650\,\mathrm{mJ/m^2}$[108] and $\gamma_2 \approx$ 30-40 $\mathrm{mJ/m^2}$[87] can be found for the surface tensions of Cu NPs and PMMA, respectively. Due to the large difference in those surface tensions, there is a strong driving force for immersion of the Cu NPs into the PMMA film, resulting in NP embedding as observed on the AFM images and confirmed by the height analysis. However, the MATLAB script employed for analysis of the height decrease is not precise enough to give a conclusion whether some NPs are fully immersed. First of all, all particles are included in the height analysis, i.e. also larger aggregates of clusters with the two- or threefold of the individual cluster size. Secondly, the height is not only measured at the highest point of each particle, but also on several other spots with lower height. In fact, all features (or pixel values) above a certain, specified height threshold (i.e. the foreground) are taken into account for the height distribution. This also explains the high overall number of counts for the height distributions in Fig. 6.7, which is equal to the number of pixels in each corresponding AFM image. Altogether, this means that no final conclusion about full immersion of single NPs can be drawn from the height distributions in Fig. 6.7. The used MATLAB script for height analysis can only be used to obtain information about NP immersion into the polymer substrate and to get a rough idea about the degree of embedding.

AFM images of Cu NPs deposited on PS (Cu04) before and after thermal annealing at 125 °C are shown in Fig. 6.8.

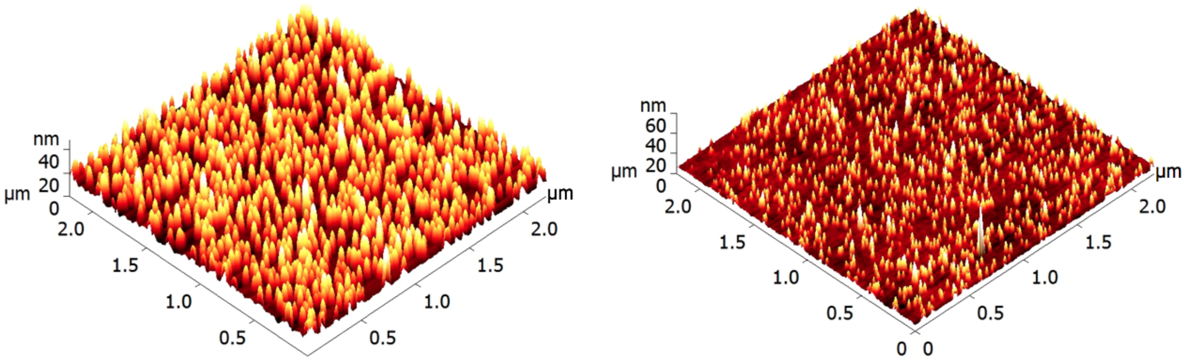

(a) As-deposited.

(b) After annealing.

Figure 6.8. AFM images of Cu NPs on PS (Cu04) (a) before and (b) after thermal annealing.

As can be clearly seen from the AFM images, the Cu NPs are partially immersed into PS after annealing. This is confirmed by the height distributions of the Cu NPs before and after annealing, which are presented in Fig. 6.9.

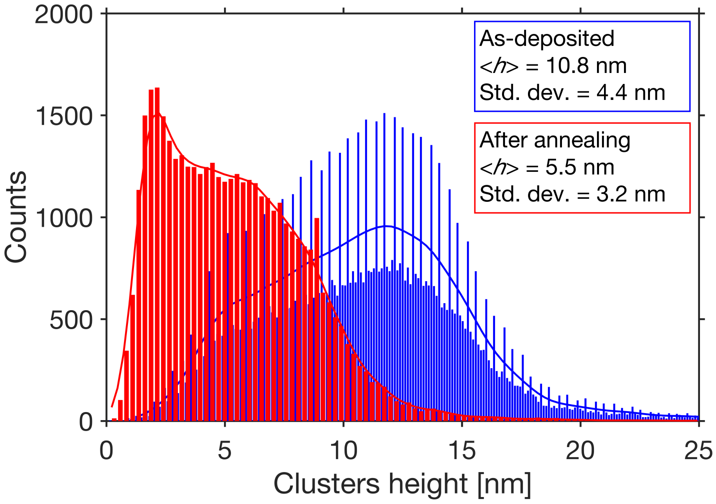

Figure 6.9. Height distributions of Cu NPs on PS (Cu04) before and after thermal annealing.

Again, the polymer film acquired the required enhanced chain mobility for NP immersion as the sample was annealed about 25 °C above the T_g of PS. Since PS also has a surface tension of about 30-40 mJ/m^2, a similarly strong driving force for NP embedding can be expected, resulting in a similar embedding depth (z_{max}). Comparing the height distributions of as-deposited Cu NPs on PMMA (Cu02) and PS (Cu04) in the Figs. 6.7 and 6.9, respectively, a significantly lower mean height can be observed for Cu04. This may be linked to the lower number of aggregates on PS (see Fig. 6.8 (a)) compared to PMMA (see Fig. 6.6 (a)) which are included in the height analysis. Consequently, the calculated mean cluster height is reduced.

So far, the immersion of Cu NPs with about 15 nm mean height into thin PMMA and PS films of ca. 50 nm thickness could be verified by AFM study of the as-deposited and immersed NPs. However, no final statement about the precise degree of immersion could be made due to insufficient accuracy of the applied method for height analysis of the clusters. Therefore, additional experiments were carried out with the aim to investigate the immersion of specific Cu NPs into a PMMA film. For that purpose, two standard 1 x 1 cm large Si substrates were used which were marked using focused ion beam (FIB) milling prior to the thin film deposition. In doing so, a ca. 20 x 20 µm large cross was milled into the center of each sample (see dimensions of the cross in Fig. 6.10).

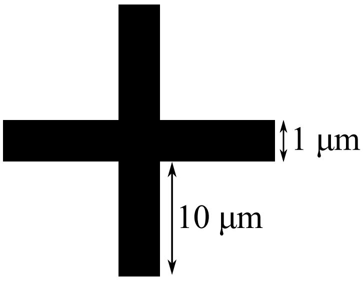

Figure 6.10. Schematic drawing showing the rough dimensions of the cross in the center of the Si substrate made by FIB milling.

After the following spin-coating of PMMA, it was possible to find the marked area using the optical microscope included in the AFM setup. Having this orientation mark on the sample, deposited NPs close to this mark could be easily recognized for each AFM measurement so that the height evolution of the identical Cu NPs could be studied before and after several annealing steps. The clusters were deposited with a low coverage $<$ 0.5 ML in order to minimize formation of aggregates and facilitate the height measurement on the single NPs. In the following, the results are only presented for one of the two prepared samples (Cu06) since they were very similar for both samples.

AFM images of the Cu NPs on PMMA were taken in two specific areas of the sample before and after the annealing steps in order to follow the immersion of the NPs in those areas. The two areas are shown in the AFM images in Fig. 6.11 for the as-deposited Cu clusters.

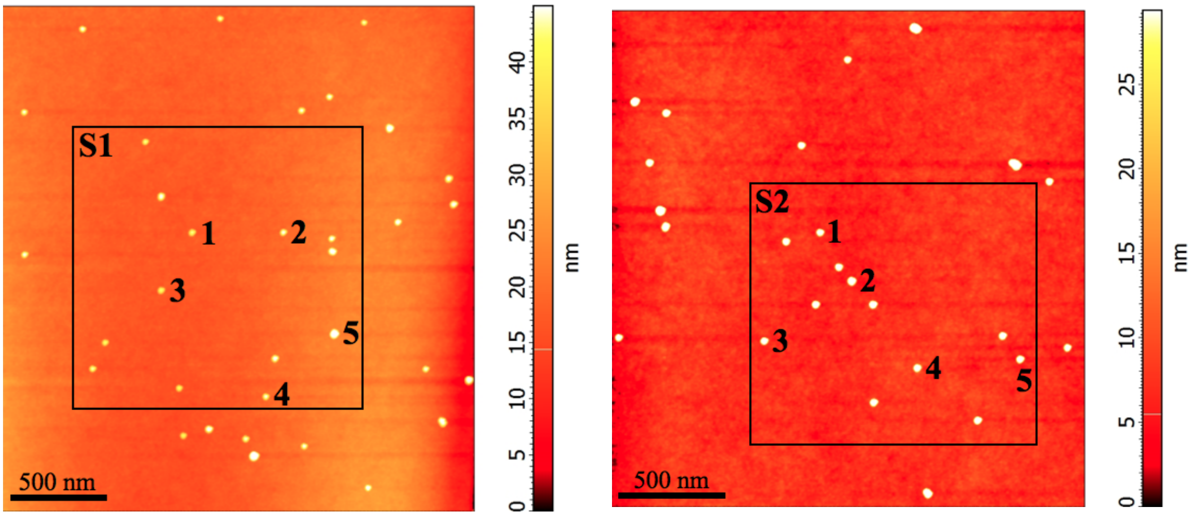

(a) First area.

(b) Second area.

Figure 6.11. AFM images of as-deposited Cu NPs on PMMA in two specific areas of the sample (Cu06). The marked sections (S1 and S2) are presented in Fig. 6.12 before and after the respective annealing steps. In addition, the height evolution of the labeled NPs is given in Tab. 6.6.

All in all, 41 NPs from both areas were taken into account for the respective height measurements from which height histograms with the corresponding mean values ($<h>$) were created, see Fig. 6.13. Furthermore, AFM images of the sections S1 and S2 (see Figs. 6.11 (a) and 6.11 (b)) are presented for the as-deposited NPs and after the annealing steps in Fig. 6.12. Finally, the measured height values of the numbered NPs are listed for each section in Tab. 6.6 in order to show the height evolution of specific NPs with increasing annealing time. For detailed information about the annealing conditions of Cu06, see Tab. 6.2.

From comparison of the AFM images before and after first annealing, the NPs are observed to be already embedded by a large fraction. As presented in Figs. 6.13 (a) and 6.13 (b), the cluster mean height calculated for all 41 clusters is decreased from 16.8 nm to 3.9 nm. Thus, most of the NPs are already immersed by about 3/4 of their height, see for instance NPs no. 3 and 4 in S2. Further immersion of the Cu clusters after additional annealing steps cannot easily be seen on the respective AFM images as it progresses very slowly. In fact, the height analysis of all NPs reveals that $<h>$ decreases by 0.3 nm after second and third annealing (overall 20 minutes annealing time), respectively, and only 0.1 nm after fourth and fifth annealing, respectively. Hence, the final cluster mean height averaged over 41 NPs is 3.1 nm after 60 minutes annealing time. Looking at the specific height evolution in Tab. 6.6, it can be seen that some NPs already reach their final embedding depth after first annealing, see for example NPs no. 3 and 5 in S1, and NP no. 1 in S2. On the other hand, other NPs keep embedding further and stop immersing into PMMA after second annealing (NP no. 4 in S2), third annealing (NPs no. 2 in S1 and no. 5 in S2), or after the last annealing step (e.g. NPs no. 1 in S1 and no. 3 in S2). Generally, the NP can be expected to be in thermodynamic equilibrium corresponding to the minimum of the surface free energy (F_s), when continuing annealing above T_g does not promote further embedding of the particle. Therefore, the aforementioned NPs, which reach their final embedding depth prior to the last annealing step, are assumed to be in thermodynamic equilibrium as there is no further driving force for immersion into the polymer. Since a few NPs are observed to keep immersing into the PMMA film after the last annealing step, no final conclusion can be given about their thermodynamic state. However, it can be presumed that most of the studied Cu NPs have reached their equilibrium embedding depth since the observed mean height decrease is only marginal during the last 40 minutes of annealing. For the other NPs, no or only slight immersion is expected for ongoing thermal annealing as the driving force for embedding seems to be very low at this point.

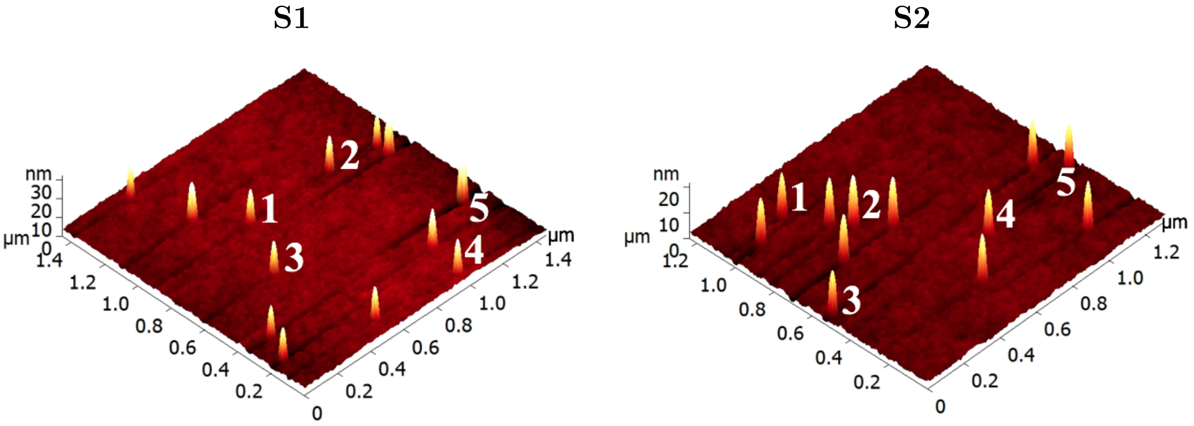

(a) As-deposited.

(b) As-deposited.

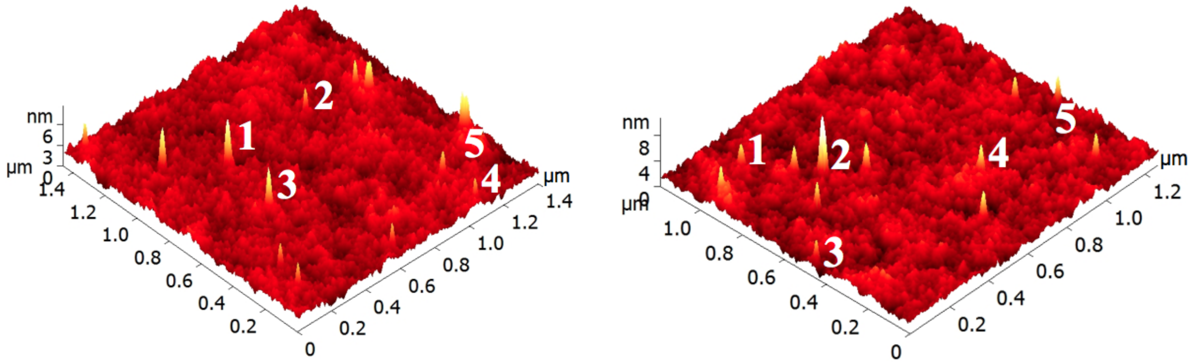

(c) After 1st annealing.

(d) After 1st annealing.

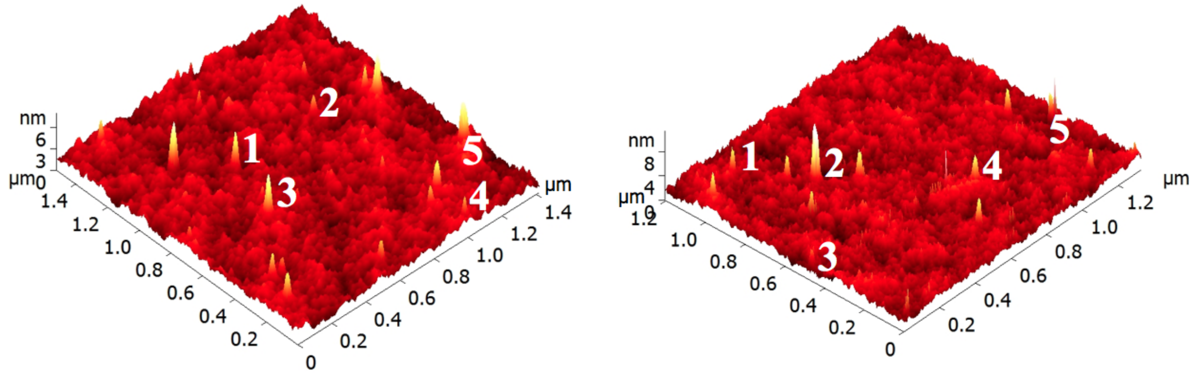

(e) After 2nd annealing.

(f) After 2nd annealing.

Figure 6.12. AFM images of specific Cu NPs on PMMA (Cu06) in the sections S1 (left column) and S2 (right column) before and after the corresponding annealing steps (see Tab. 6.2 for annealing conditions). The height decrease of the labeled NPs is given in Tab. 6.6.

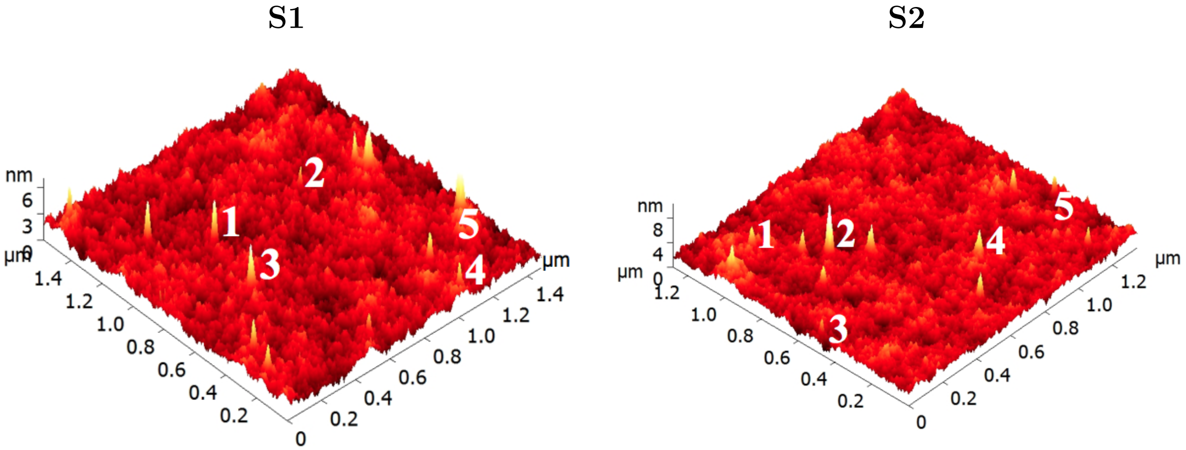

(g) After 3rd annealing.

(h) After 3rd annealing.

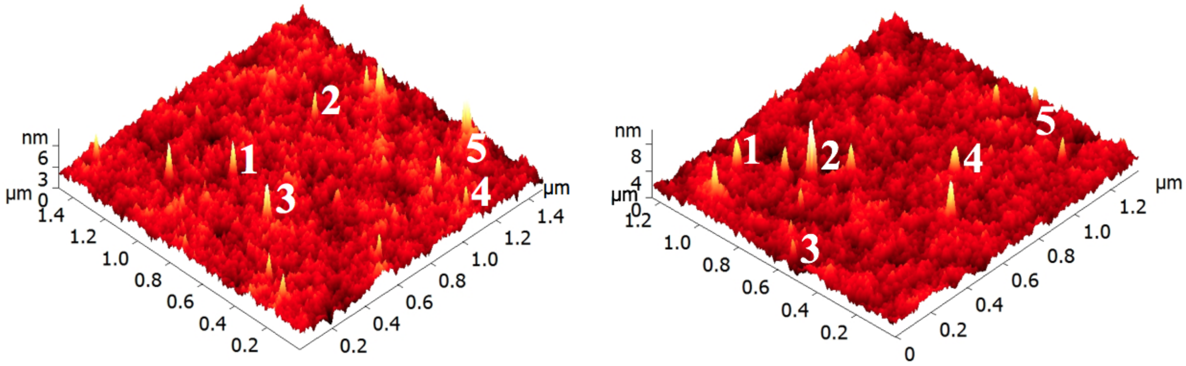

(i) After 4th annealing.

(j) After 4th annealing.

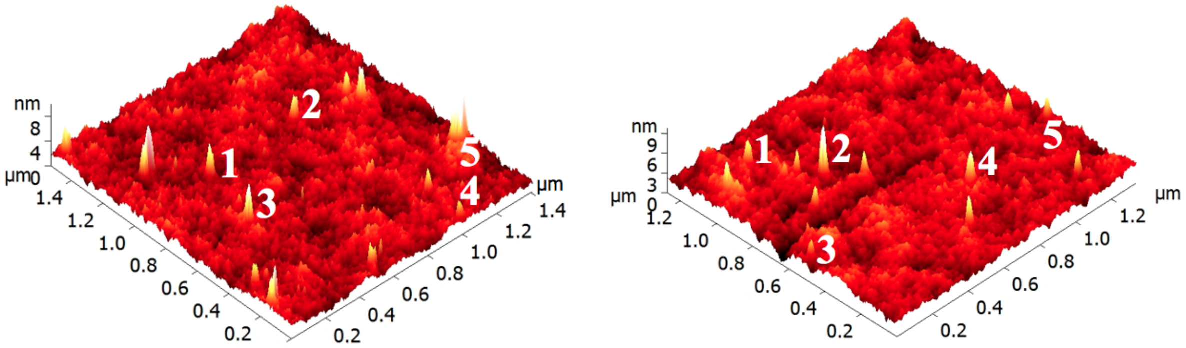

(k) After 5th annealing.

(l) After 5th annealing.

Figure 6.12. AFM images of specific Cu NPs on PMMA (Cu06) in the sections S1 (left column) and S2 (right column) before and after the corresponding annealing steps (see Tab. 6.2 for annealing conditions). The height decrease of the labeled NPs is given in Tab. 6.6.

Table 6.6. Tabular overview of the height evolution of the labeled Cu NPs on PMMA (Cu06) with increasing annealing time. See Tab. 6.2 for annealing conditions of the sample.

NP no.	Cluster height [nm]					
	As-deposited	After 1st anneal.	After 2nd anneal.	After 3rd anneal.	After 4th anneal.	After 5th anneal.
Section 1						
1	17	6	5	5	5	4
2	17	4	3	2	2	2
3	16	5	5	5	5	5
4	17	3	3	3	3	3
5	30	5	5	5	5	5
Section 2						
1	17	3	3	3	3	3
2	18	7	7	7	7	6
3	16	4	4	3	3	2
4	16	4	3	3	3	3
5	17	4	4	3	3	3

As the results for the study of the immersion of specific Cu NPs into PMMA reveal, the NPs do not become completely embedded, but immerse by about 5/6 of their height into the polymer film. This is in contradiction to a number of studies reporting full immersion of metal NPs into polymer films[16,80,85–87]. As discussed in Sec. 4.2.1, the condition for complete NP embedding is given as

$$\gamma_1 > \gamma_{12} + \gamma_2. \tag{6.2}$$

Apparently, Ineq. 6.2 is not satisfied for the studied Cu NPs immersion into PMMA. While values for γ_1 and γ_2 can be found in literature, γ_{12} is not well known for the Cu NP-PMMA system. However, inserting of the expression for γ_{12} from Eq. 4.2 into Eq. 6.2 and solving for the contact angle (θ, see Sec. 4.2.1) yields

$$\theta < \arccos\left(\frac{2\gamma_2}{\gamma_1} - 1\right). \tag{6.3}$$

With $\gamma_1 \approx 1650\,\mathrm{mJ/m^2}$[108] for the surface tension of Cu NPs and $\gamma_2 \approx 30\,\mathrm{mJ/m^2}$ ($40\,\mathrm{mJ/m^2}$)[87] for the surface tension of PMMA, Eq. 6.3 yields $\theta < 164°$ ($162°$). This means that the contact angle between the PMMA film and the Cu NPs prior to embedding needs to be smaller than 164° (162°) so that full immersion of the NPs is ensured. As evaluated before, the cluster mean height of the 41 studied Cu clusters decreased from 16.8 nm before annealing to 3.1 nm after 60 minutes annealing time. This amounts to an average maximum embedding depth (z_{max}, see Sec. 4.2.1) of 13.7 nm or $1.63a$, with a denoting the radius of the particle. Inserting this value into Eq. 4.3 and substituting γ_{12} with the expression given in Eq. 4.2, the equation can be solved for θ according to

$$\theta < \arccos\left(\frac{1.63\gamma_2}{\gamma_1} - 1\right). \tag{6.4}$$

Using the same values for γ_1 and γ_2 as before, θ amounts to 166° (163°). These are the calculated contact angles for the as-deposited Cu NPs on the PMMA film, and they are only slightly larger than the required ones for complete NP embedding. However, the calculated θ could not be verified on the deposited Cu NPs as it is not possible to determine the contact angle of the NPs from AFM measurements.

During the previous discussion, the literature values for γ_1 and γ_2 were presumed to be correct. In reality, however, there may be deviations from the reported values which could explain the discrepancy between expected (complete NP immersion) and observed results (partial NP immersion). There is generally consensus about the approximate value of the surface tension of PMMA which ranges between 30-40 mJ/m^2[87, 109, 110]. In fact, γ_2 approaches the lower limit with increasing temperature and is for instance reported to be 32 mJ/m^2 at 140 °C[110]. Since the studied samples are also annealed at an increased temperature ($T_a = 125\,°\mathrm{C}$), the surface tension of PMMA is not suspected to go beyond values of 40 mJ/m^2 and is, thus, assumed to be correctly stated in literature. In contrast, the surface tension of Cu NPs is an ongoing subject of debate and contradictory reports can be found about it. While some studies suggest an increase of γ_1 going from the bulk to nanosize regime[82, 111], others report a decreasing surface tension with size[108, 112]. Since the condition for complete NP immersion, Ineq. 6.2, is not satisfied in this study, a smaller value than the assumed bulk value can be supposed. This is due to the fact that a strongly decreased surface tension of the Cu NP may lead to invalidity of Ineq. 6.2 which would be in agreement with the observed results. It is known that Cu exhibits high chemical reactivity. After deposition of the Cu NPs on the substrate and following exposure to air, the NPs oxidize quickly. In addition, annealing of the sample might enhance the reactivity to other gaseous components which are present at very low concentration in ambient atmosphere, e.g. trace gases like SO_2 or CS_2. As will be discussed later, annealing of the Cu NPs is accompanied by vanishing plasmonic properties, thus, indicating degradation of the NPs. This may be a reason for a drastic decrease of the surface tension and consequential non-complete embedding of the Cu NPs in PMMA because the condition for complete embedding would not be satisfied. As a conclusion, the observed partial immersion of the Cu clusters into PMMA is in contradiction to a number of other studies reporting full NP immersion into polymers. A final conclusion about the origin cannot be drawn since γ_{12} is not known and the actual value for γ_1 might vary from the reported one due to nanosize effects or chemical reaction of the Cu NPs with ambient gases in the atmosphere during thermal annealing.

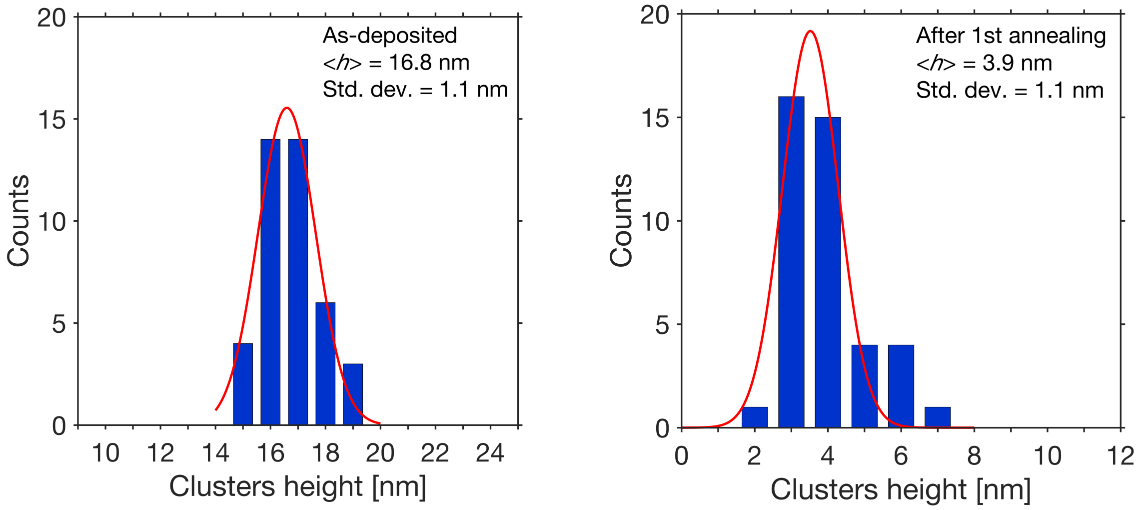

(a) As-deposited.

(b) After 1st annealing.

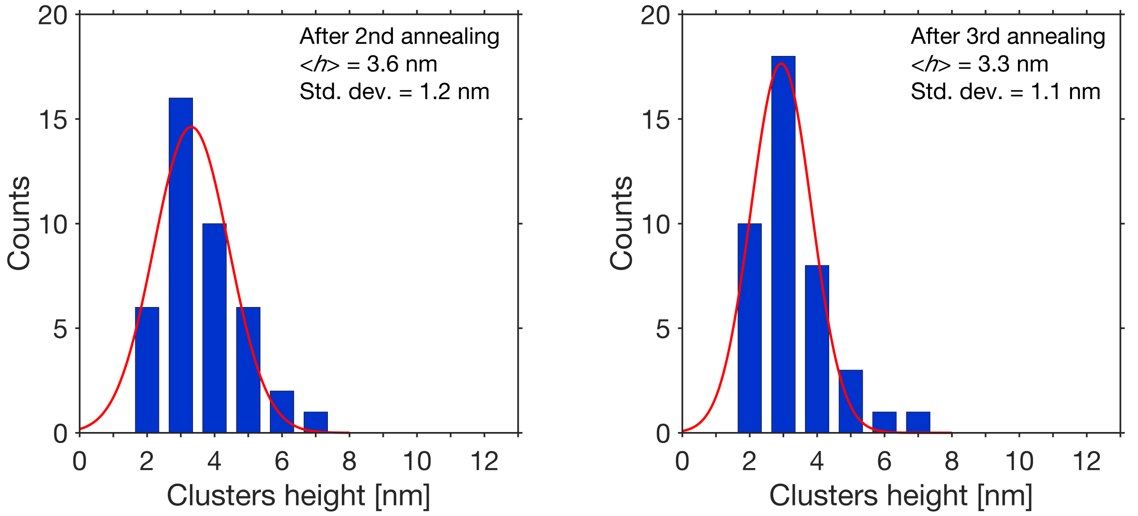

(c) After 2nd annealing.

(d) After 3rd annealing.

Figure 6.13. Height histograms with respective Gaussian fits for specific Cu NPs on PMMA (Cu06) (a) before and (b)-(f) after the corresponding annealing steps.

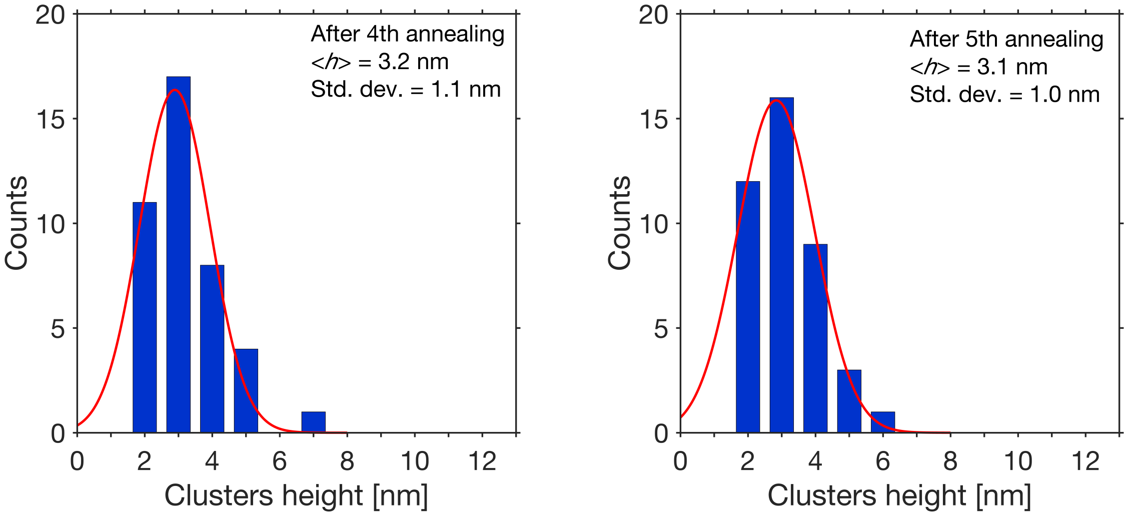

(e) After 4th annealing. **(f)** After 5th annealing.

Figure 6.13. Height histograms with respective Gaussian fits for specific Cu NPs on PMMA (Cu06) (a) before and (b)-(f) after the corresponding annealing steps.

Besides the thermodynamic aspect of the Cu NP immersion into PMMA, the kinetics of this process also needs to be considered.

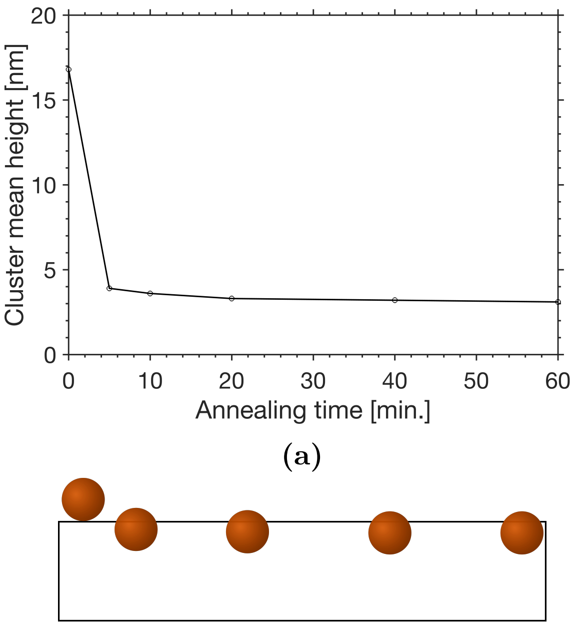

(a)

(b)

Figure 6.14. (a) Cu cluster mean height as a function of annealing time and (b) schematic drawing showing the corresponding embedding stages of the Cu NPs.

In Fig. 6.14 (a), the cluster mean height ($<h>$) is presented as a function of annealing time (t_a), while the corresponding embedding stages of the Cu NPs are schematically shown in Fig. 6.14 (b). As can be seen, the Cu NPs immerse quickly within the first 5 minutes into PMMA. Then, the immersion slows down drastically and the embedding velocity v approaches zero after 60 minutes annealing time. As already suggested, this is related to a decreasing driving force for further immersion since most of the NPs are already close to their thermodynamic equilibrium corresponding to the maximum embedding depth. The graphs in Fig. 6.14 suggest to subdivide the Cu NP immersion into two main stages. The first one proceeds within the first 5 minutes and is characterized by quick NP immersion into the polymer. Assuming the embedding velocity to be constant in this stage, v can be calculated to be ca. 2.5 nm/min. The second main stage constitutes the left 55 minutes annealing time during which $<h>$ decreases only slightly. As already mentioned in Sec. 4.2.4, Ruffino *et al.* have studied the kinetics of the NP immersion of Ag and Au NPs into thin PS and PMMA films. They observed a characteristic time at the beginning of the annealing process for which $<h>$ remained constant, which was followed by the NP immersion with roughly constant embedding velocity. For instance, t and v for Ag NPs on PMMA and $T_a = 120\,°\mathrm{C}$ were found to be $t_0 = 3632\,\mathrm{s}$ ($\approx 1\,\mathrm{h}$) and $v = 0.12\,\mathrm{nm/min}$. Comparison with the results of this study show a large difference in both the coating time and embedding velocity. While the formation of a wetting layer must proceed within seconds or few minutes instead of 1 hour, v is ca. 20 times higher in this study. This strong discrepancy in the kinetics of the immersion processes may originate from differences in the experimental conditions. While Ruffino *et al.* carried out annealing in N_2 environment and used clusters of about 21 nm mean height, the current experiments were conducted in ambient atmosphere with slightly smaller clusters. It was discussed in Sec. 4.2.2 that Faupel *et al.*[85] reported an increasing embedding temperature with cluster size due to stronger metal-polymer interaction and resulting suppression of the kinetics. Thus, the embedding velocity is expected to be lower for larger clusters. The role of the atmosphere is not clear, but not suspected to be decisive. As long as the sample is annealed considerably above the T_g, the required long-range chain mobility for NP immersion is given. Both samples were annealed at a very similar temperature. All in all, the larger cluster size alone does not explain the large difference in the kinetics between the studied immersion of Cu NPs and the work of Ruffino *et al.*. Hence, more details about the exact methodology and execution of the experiments in the study of Ruffino *et al.* are required to find the origin for the described discrepancy.

6.2.2. Optical Spectroscopy

After evaluation of the AFM results for the Cu-deposited samples, the results of the transmittance measurements are presented and discussed in this subsection. Emphasis is placed on the evolution of the plasmonic properties of the Cu NPs upon immersion into the polymer films.

Calculation within Quasi-Static Approximation

In Fig. 6.15, the extinction cross-sections of Cu spheres of different sizes and in different dielectric environments are shown. They were calculated within the aforementioned quasi-static approximation (see Sec. 2.3.3) according to

$$C_{ext} = 9\frac{\omega}{c}\varepsilon_m^{3/2}V\frac{\varepsilon_2}{[\varepsilon_1 + 2\varepsilon_m]^2 + \varepsilon_2^2}. \tag{6.5}$$

While the dielectric data for the metals is taken from the work of Johnson *et al.*[57], the dielectric constants of air ($\varepsilon_m = 1$) and the polymers PMMA and PS ($\varepsilon_m = 2.6$) are constant in the considered spectrum[113].

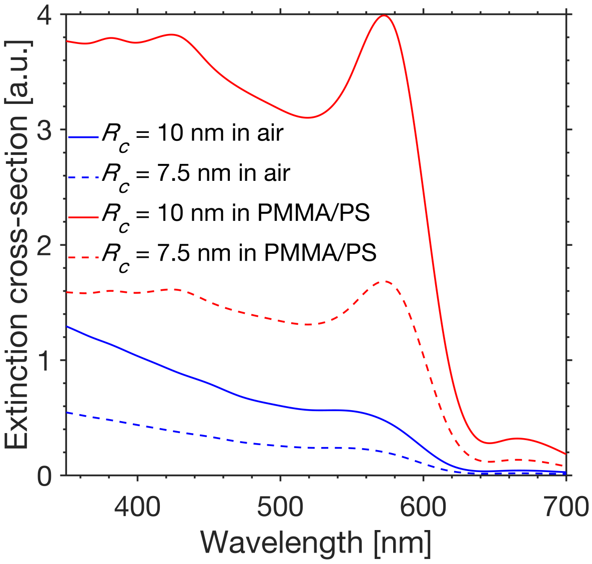

Figure 6.15. Extinction cross-section for Cu NPs in different dielectric environments, calculated using Eq. 6.5. Dielectric data are taken from [57].

As can be seen from Fig. 6.15, the extinction peaks for the Cu spheres in air are located at ca. $\lambda = 560\,\text{nm}$. Upon immersion into the polymer, the plasmon bands become redshifted to about 575 nm and their intensity is increased, accompanied by increased intensity of the bands. Further, the intensity of the plasmon band is also increased for larger particles. The increased LSPR peak intensity is readily understood upon consideration of Eq. 6.5. As shown, C_{ext} is proportional to the volume of the sphere (i.e. $\propto R_c^3$) and $\varepsilon_m^{3/2}$. Hence, increasing particle size and changing dielectric environment leads to an increased intensity of the LSPR peak. The redshift of the extinction peak can also be explained considering the term $[\varepsilon_1 + 2\varepsilon_m]^2$ in the denominator of Eq. 6.5. An increased value of ε_m requires a decreased value of ε_1 so that the resonance condition is still satisfied. Since ε_1 typically decreases with increasing wavelength in the spectral range of interest[57], this leads to a redshift of the absorption peak. In reality, the spectral position of the LSPR band is also affected by other factors like particle size, shape, surface roughness, or interparticle distance[114, 115].

Experimental Observations

First, the relative extinction spectra for Cu NPs deposited on PMMA before and after thermal annealing are presented in Fig. 6.16. As for all the Cu-deposited samples, the detailed annealing conditions for the respective sample are given in Tab. 6.2.

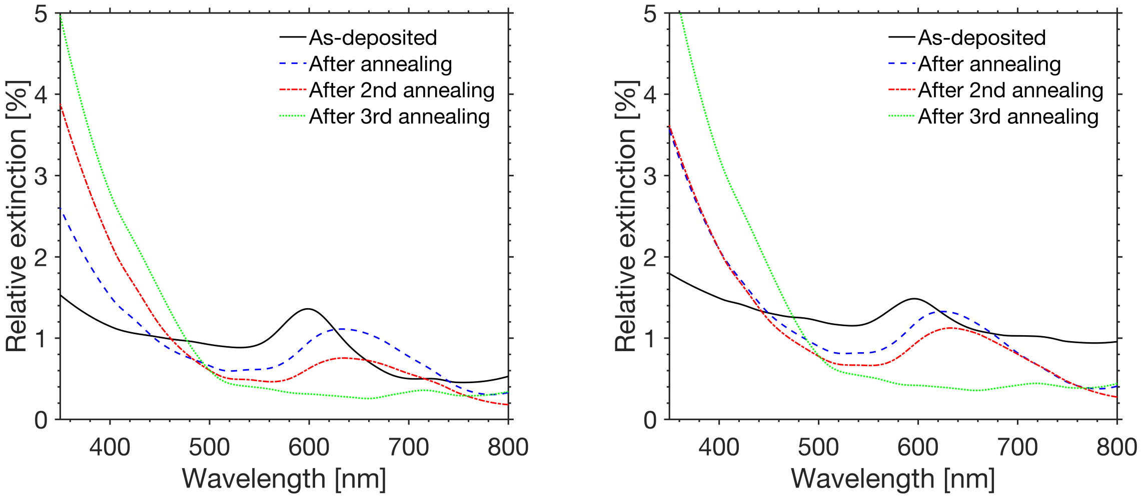

(a) Cu02.

(b) Cu03.

Figure 6.16. Relative extinction spectra for Cu NPs on PMMA before and after thermal annealing.

The spectra of both samples (Cu02 and Cu03) exhibit very similar characteristics. Before annealing, the LSPR peaks are located at ca. 595 nm for the as-deposited Cu NPs. In comparison to the calculated extinction cross-section for Cu spheres in air, this represents a redshift of about 35 nm of the plasmon band. Partly, this is due to the fact that the Cu NPs were deposited on a polymer substrate and, thus, partially have a different dielectric environment. In theory, this would require to take into account the so-called effective dielectric function[116] according to

$$\varepsilon_{eff} = \alpha\varepsilon_m + (1 - \alpha)\varepsilon_{air}, \qquad (6.6)$$

with α denoting the weighing factor, and $\varepsilon_{air} = 1$ denoting the dielectric constant of air. As shown in Fig. 6.15, even the calculated spectra for Cu nanospheres completely embedded in PMMA/PS ($\alpha = 1$) do not agree exactly with the experimental spectra for as-deposited Cu NPs regarding the position of the plasmon bands. This discrepancy may be explained with the simplicity of the used quasi-static approximation which neglects important factors such as particle shape and size. However, it is a useful method to obtain a rough prediction of the LSPR peaks for Cu NPs.

After first annealing, the plasmon bands for Cu02 and Cu03 are redshifted. This can be explained with the immersion of the Cu NPs into the PMMA film, which was confirmed in the previous subsection, and the accompanied increase of ε_{eff}. Immersion of the NPs should also lead to increasing intensity of the plasmon bands as discussed before. Instead, the intensity is decreased slightly after first annealing and decreases further after an additional annealing step. Finally, after third annealing at increased temperature ($T_a = 180\,°\text{C}$), the plasmon bands are completely damped. This is in contradiction to the presented theory and earlier studies of Ag NP immersion into PMMA where a strong increase of the LSPR band intensity was observed after thermal annealing and NP embedding[16]. The observed quenching of the plasmon band may be related to the high chemical reactivity of Cu. In particular, quick oxidation of Cu in ambient atmosphere is a well-known phenomenon[117–119] and may be enhanced at elevated temperatures. Consequently, this would result in quenching of the plasmonic properties. It is also possible that PMMA, whose monomeric units contain two oxygen atoms, contributes to the oxidation during thermal annealing.

The relative extinction spectra for Cu NPs on PS are shown before and after thermal annealing in Fig. 6.17.

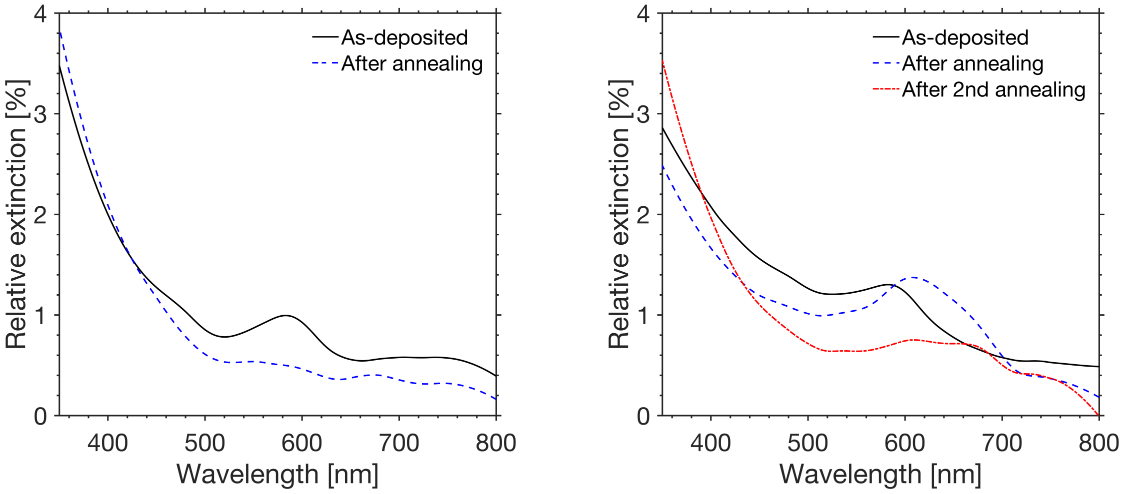

(a) Cu04.

(b) Cu05.

Figure 6.17. Relative extinction spectra for Cu NPs on PS before and after thermal annealing.

Similar to the Cu NPs on PMMA, the plasmon band of Cu NPs on PS (Cu04) vanishes after thermal annealing, this time already after first annealing. Instead, the intensity of the LSPR peak is increased for Cu05 after first annealing, accompanied by a redshift indicating immersion of the NPs. This may be related to the lower annealing temperature ($T_a = 90\,°\mathrm{C}$), which was 10 °C below the T_g of PS. It is suggested that the degradation of the Cu NPs proceeds slower at the lower temperature so that the plasmonic properties are preserved longer. However, a second annealing leads to damping of the plasmon band, confirming the experimental observations for the previous samples. It it interesting to note that the Cu NPs (Cu05) seem to immerse into PS even though the sample was annealed below the bulk T_g. This is in accordance with the presented theory about depression of the surface T_g in polymers and presence of a liquid-like layer in near-surface region with enhanced mobility (see Sec. 4.2.2). Since NP immersion requires long-range chain mobility, which is acquired at T_g, the described results suggest a reduction of the surface T_g by at least 10 °C for the prepared PS films.

In order to verify the made assumptions regarding oxidation of the Cu NPs and the role of the polymer, transmittance measurements were carried out on Cu NPs deposited on bare quartz substrates. In Fig. 6.18, the relative extinction spectra for Cu07 are shown before and after thermal annealing.

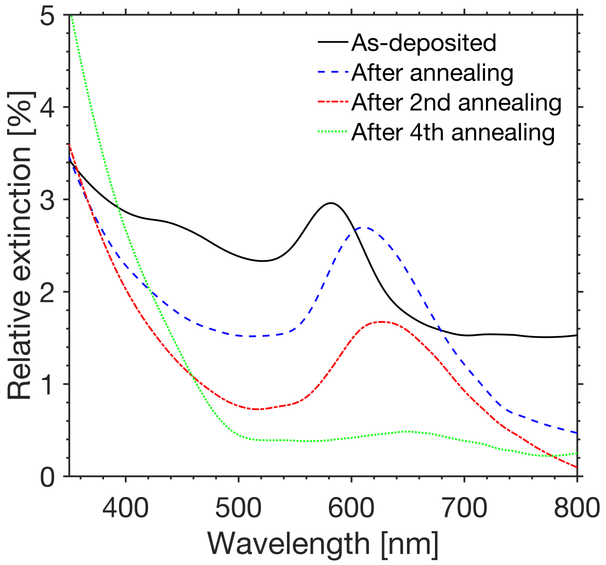

Figure 6.18. Relative extinction spectra for Cu NPs on quartz (Cu07) before and after thermal annealing.

The plasmon band of the as-deposited clusters has higher intensity than the previously presented samples. This is most likely due to the larger cluster size for Cu07 (about 19 nm mean height for $U_{QP} = \pm 1000\,\mathrm{V}$, cf. Fig. 6.1) which leads to enhanced extinction. After first annealing, the plasmon band is redshifted and the intensity is increased. This can be assigned to partial oxidation of the Cu NPs and the related formation of copper oxide, which corresponds to a different dielectric environment with increased ε_m. Additional annealing leads to a slight redshift and decreasing intensity of the band, indicating progressing oxidation of the Cu NPs. After fourth annealing, the plasmon band is almost completely quenched as the continuous conversion of Cu to copper oxide

NPs is supposed to lead to degradation of the particles. Since the observed quenching of the LSPR proceeds very similar for Cu-deposited samples with and without a polymer film, the role of the polymer can be neglected. Hence, it is expected to be a solely intrinsic effect of the Cu NPs.

Cu NPs were also deposited on a bare quartz substrate (Cu08) which was stored for several weeks in ambient atmosphere (room temperature and relative humidity of 30-50%) in order to test the stability of the LSPR. The relative extinction spectra for the as-deposited and the long-term stored Cu NPs are presented in Fig. 6.19.

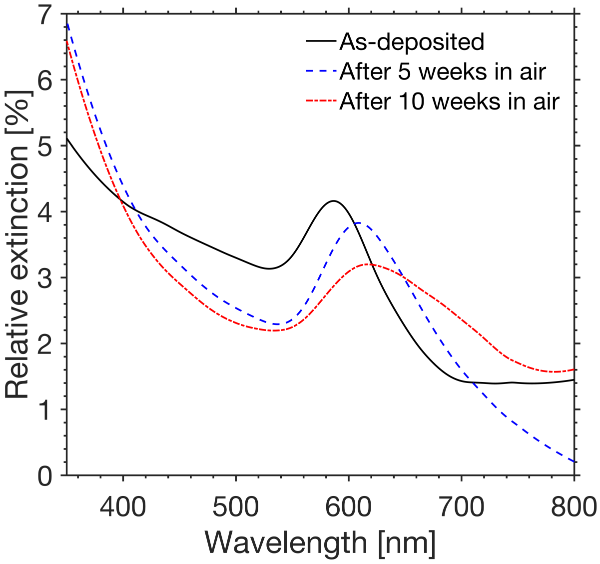

Figure 6.19. Relative extinction spectra for as-deposited Cu NPs on quartz (Cu08), and after long-term storage in ambient atmosphere.

In principal, the spectra look very similar to the one for Cu07, but the time scale is strongly prolonged for Cu08. After 5 weeks of storage in ambient atmosphere, a redshift and increased intensity of the plasmon band can be seen. After additional 5 weeks, the band is slightly redshifted, but the intensity is decreased. It can be expected that the LSPR will be completely quenched after additional 5-10 weeks storage in ambient atmosphere. The results show that the plasmonic properties of the non-annealed Cu NPs are preserved on a much longer time scale compared to the annealed Cu NPs. This is expected since the degradation (most likely oxidation) process is less efficient a room temperature and requires more time.

In the following, two different methods for preservation of plasmonic properties during NP immersion are suggested. In the first, Cu NPs are deposited on PS and the sample (Cu09) is annealed for only 1 minute in order to prevent strong oxidation of the NPs. The corresponding extinction spectra are shown in Fig. 6.20.

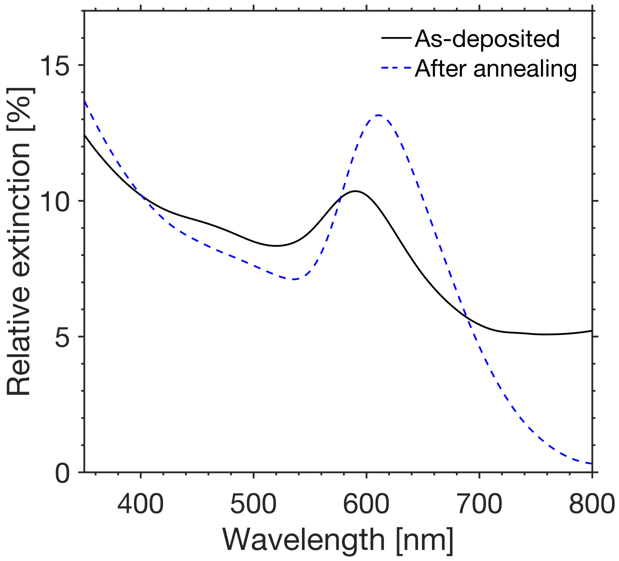

Figure 6.20. Relative extinction spectra for Cu NPs on PS (Cu09) before and after thermal annealing.

As can be seen, the plasmon band is redshifted and the intensity is strongly increased after annealing. Hence, it is expected that the NPs are already partially immersed into PS, while the particles were not oxidized sufficiently to quench the LSPR. In fact, height analysis with the MATLAB script revealed that the cluster mean height decreased considerably from 15.1 nm to 6 nm after annealing. Therefore, this could depict a possibility to produce Cu-polymer nanocomposites while conserving their plasmonic properties. However, as indicated for Cu08, the LSPR of the NPs is expected to be damped slowly on a long time scale if the sample is stored in ambient atmosphere.

As a second method, the formation of an oxide shell around the Cu NP core is suggested which should protect the Cu core from degradation during the annealing process. For formation of the oxide shell, quartz substrates with as-deposited Cu NPs were treated in ozone environment (see Tab. 6.2 for ozonation times of corresponding samples). In Fig. 6.21, the relative extinction spectra for Cu NPs on quartz (Cu10) are presented before ozone treatment, after ozone treatment, and following long-term storage in ambient atmosphere.

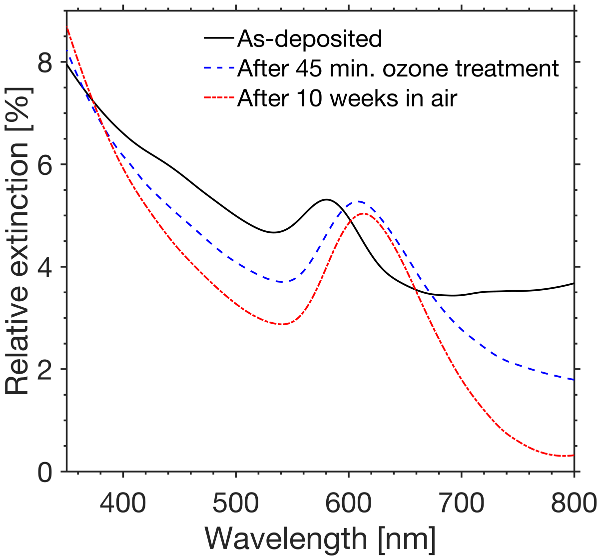

Figure 6.21. Relative extinction spectra for as-deposited Cu NPs on quartz (Cu10), after ozone treatment, and long-term storage in ambient atmosphere.

After ozone treatment, the plasmon band is redshifted and the intensity is increased, indicating the formation of an oxide shell around the Cu NP and the accompanied change of the dielectric environment. After 10 weeks of storage in ambient atmosphere, the intensity is not decreased, but further increased and the band is slightly redshifted. Hence, the LSPR of the Cu NPs is preserved and can be expected to be conserved for additional weeks in ambient atmosphere. Compared to the results for the sample with Cu NPs non-treated with ozone (Cu08) in Fig. 6.19, this shows that the proposed method for copper oxide shell formation could depict a reasonable approach to protect the Cu NPs from degradation during annealing. Thus, it was also applied to samples with Cu NPs which were annealed after ozone treatment. First, the relative extinction spectra for Cu NPs deposited on a bare quartz substrate (Cu11) are presented before and after ozone treatment, after thermal annealing, and following long-term storage in ambient atmosphere in Fig. 6.22 (a).

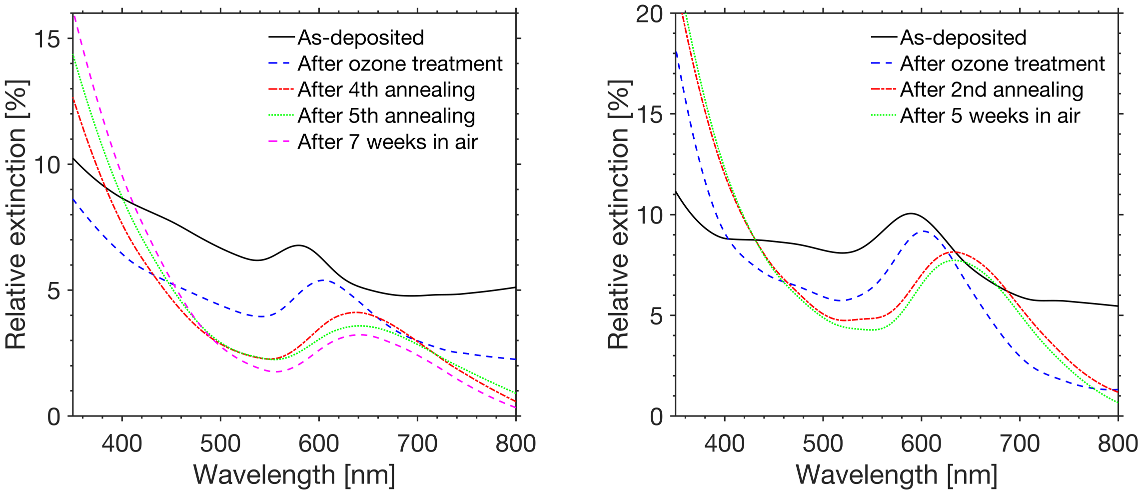

(a) (b)

Figure 6.22. Relative extinction spectra for as-deposited Cu NPs on (a) quartz (Cu11) and (b) PS (Cu12) after ozone treatment, following thermal annealing, and long-term storage in ambient atmosphere.

Again, increasing plasmon band intensity and a redshift of the band can be observed after ozone treatment. After 4th annealing, the band is further redshifted accompanied by an increased intensity, indicating progressing oxidation of the Cu NPs. Finally, a fifth annealing step leads to a marginal decrease of the intensity. Overall, the LSPR is preserved after 30 minutes annealing time, which implies a considerably higher stability compared to the non-ozonated Cu07 for which the plasmon band already vanished after 20 minutes annealing time. Furthermore, the LSPR of the Cu NPs of Cu11 is stable after 7 weeks storage in ambient atmosphere. A similar tendency is observed for the Cu NPs deposited on PS (Cu12, see Fig. 6.22 (b)) which were treated in ozone environment and thermally annealed, followed by storage in ambient atmosphere. Similar to Cu11, the plasmon band exhibits increased intensity after ozone treatment and is redshifted, and the following annealing causes a further redshift of the band. This may be partially related to further oxidation and partially due to immersion of the Cu NPs into PS. The LSPR is found to be conserved after 5 weeks of storage in ambient atmosphere.

All in all, the pre-annealing treatment of the Cu NPs in ozone environment turns out to be a suitable method to prevent quenching of plasmonic properties of the NPs during thermal annealing and to enhance the long-term stability of the LSPR. The results also suggest a difference in the dynamics regarding the oxidation during annealing and ozone treatment, respectively. It is supposed that thermal annealing leads continuous conversion of the Cu NP into a copper oxide particle with diminished plasmonic properties, while ozone treatment causes the formation of an oxide shell around the Cu NP which efficiently reduces the diffusion of oxygen atoms to the Cu core and thus slows down the degradation considerably. However, the dynamics of these processes have to be studied in more detail so that the made hypotheses can be directly proven or, if necessary, adjusted.

6.3. Silver-Deposited Samples

As already mentioned, the second part of the project dealt with the fabrication of ordered arrays of Ag NPs (see Sec. 5.1.2 for experimental procedure). In this section, the results from AFM and OS measurements are evaluated regarding the feasibility of the fabrication approach and the plasmonic properties of the obtained structures.

6.3.1. Atomic Force Microscopy

3 samples with different periodicity in the patterns were fabricated. They are listed in Tab. 6.7 together with the respective widths of the Ag stripes (d_{st}) and the gaps (d_{gap}) in between those stripes. Originally, these dimensions correspond to the widths of the PMGI trenches and the PMMA layers after EBL.

Table 6.7. Tabular overview of the samples prepared with EBL and cluster deposition, and the respective dimensions of the patterns.

Sample	d_{st} [nm]	d_{gap} [nm]
Ag03	120	400
Ag04	120	300
Ag05	120	150

During fabrication of the ordered arrays of Ag NPs on PMGI, the annealing step prior to the lift-off was very important in order to enable immersion of the NPs into PMGI and, thus, enhance the required adhesion to withstand the following lift-off. Therefore, two test samples (Ag01 and Ag02) were prepared with coverage of ca. 1-2 MLs, which were used to study the immersion of the Ag NPs into the PMGI films. The samples were annealed at 190 °C for 2 minutes (Ag01) and 5 minutes (Ag02), respectively, and subsequently analyzed using AFM. The height analysis with the aforementioned MATLAB script (see App. B) reveals a cluster mean height decrease of about 2 nm for Ag01 and ca. 4 nm for Ag02. This is expected to be enough to ensure sufficient adhesion of the Ag NPs to PMGI for the lift-off procedure. Therefore, the following samples (Ag03-Ag05) were annealed 2-3 minutes (see respective annealing times in Tab. 6.4) prior to lift-off.

It should also be noted that thermal annealing was carried out above the melting temperature (T_m) of PMMA which is about 160 °C. Consequently, the PMMA layers are expected to melt and collapse during annealing and, thus, form a more or less plane surface. This is confirmed by AFM images of a prepared sample before and after annealing for 2 minutes, which are presented in Fig. 6.23. The patterned surface of PMMA can be clearly seen in Fig. 6.23 (a), with the reddish lines representing PMMA and the black line denoting the PMGI trenches.

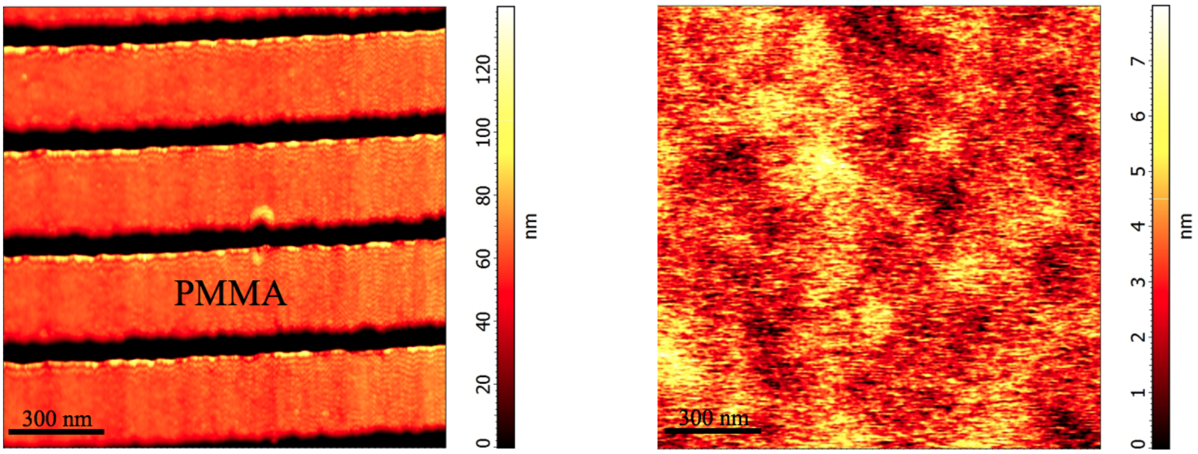

(a) (b)

Figure 6.23. AFM images of a sample, which was patterned using EBL, (a) before annealing and (b) after annealing at $T_a = 190\,°\mathrm{C}$ for 2 minutes.

After annealing, no pattern can be recognized. Instead, the surface roughness is on a scale of a few nm and resembles one of a polymer surface. Hence, it corresponds probably to the flat surface of the PMMA film which covers entirely the PMGI film. This collapse of the PMMA layers should not depict a problem for the lift-off in acetone as the PMMA can be easily reached and dissolved, while the PMGI film and the partially immersed Ag NPs should be unaffected. In Fig. 6.24 (a), an AFM image of Ag03 is presented after the lift-off.

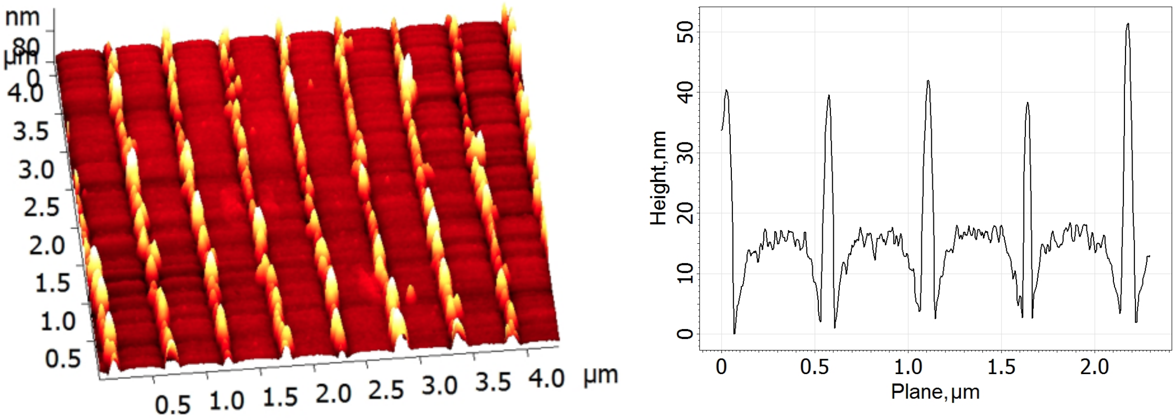

(a) (b)

Figure 6.24. (a) AFM image of Ag03 after lift-off showing arrays of Ag NPs with ca. 520 nm period, and (b) the height profile taken at an arbitray point across the arrays.

The AFM image clearly shows the desired arrays of Ag NPs on the surface of PMGI, thus, confirming the feasibility of the applied fabrication approach. According to the height profile taken at an arbitrary point across the Ag stripes, which is shown in Fig.

6.24 (b), the coverage is ca. 2 MLs of Ag NPs. Considering the width of the stripes ($d_{st} = 120\,\text{nm}$), the NPs seem to have a large lateral diameter as some individual NPs fill out the entire width of the respective trench. The reason might be that the clusters are still covered by a thin film of PMMA which could not be removed during the lift-off. Consequently, the apparent dimensions of the particles would be increased and single NPs could not be distinguished easily. Therefore, a second lift-off was carried out on the sample in order to prove the assumption (see Tab. 6.4 for lift-off conditions). An AFM image of Ag03 after the second lift-off is presented in Fig. 6.25.

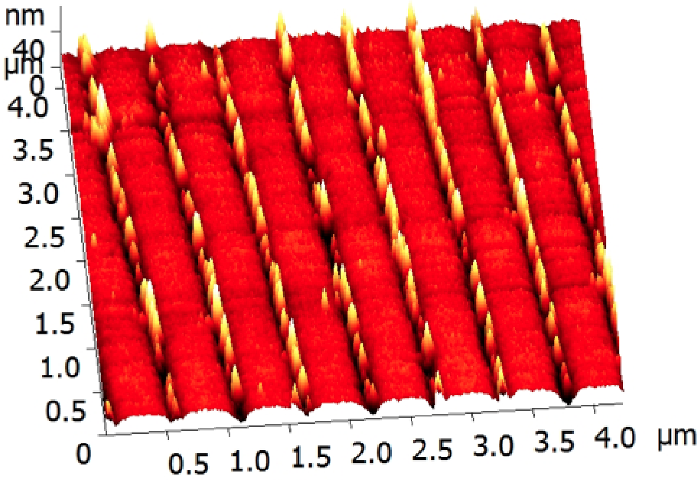

Figure 6.25. AFM image of Ag03 after the second lift-off.

Compared to the AFM image of Ag03 after the first lift-off, the cluster coverage is lower and some spots within the Ag arrays do not exhibit any NPs. Hence, the overall quality of the sample is worsened. This is probably related to the longer ultrasonic treatment in acetone (3 minutes) compared to the first lift-off (1 minute) which caused ripping out of some Ag NPs. This is also an indication that the adhesion of the clusters on PMGI was not sufficient to withstand the lift-off process. The size of the clusters is still relatively large. Since the AFM image was taken with a very sharp tip, tip convolution effects are ruled out and the large size of the particles appears to be correct. It is also possible that the low interparticle distance within the Ag stripes lead to the formation of aggregates with larger size compared to single NPs.

In Fig. 6.26, an AFM image of Ag04 is presented after the lift-off. The ordered arrays of Ag NPs are clearly seen and the overall quality is good. However, the stripes do not exhibit perfect continuity as they reveal some vacancies where the Ag NPs are missing. Again, it is assumed that those NPs were ripped out of the PMGI surface during the ultrasonic treatment which was relatively long for this sample ($t_{us} = 3\,\text{min}$). This could either be prevented by a shorter ultrasonic bath in acetone or a longer annealing time prior to lift-off in order to ensure stronger NP immersion and, thus, higher adhesion of the NPs. Consequently, the NPs would have a higher resistance against the wet chemical procedure and the final structure would have an enhanced quality regarding continuity of the stripes.

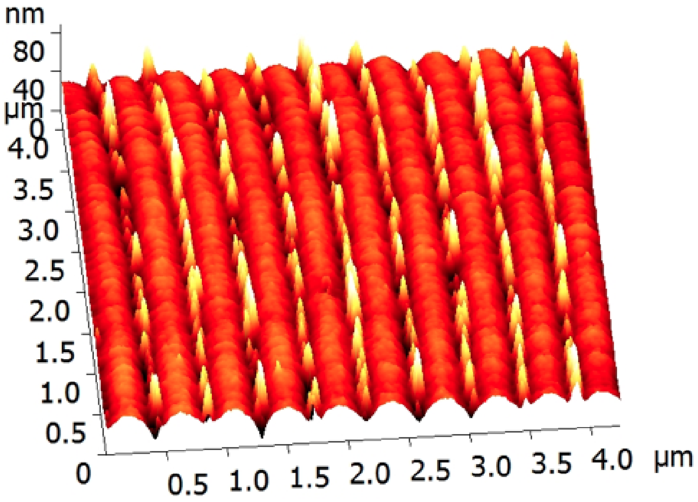

Figure 6.26. AFM image of Ag04 after lift-off showing stripes of Ag NPs with about 420 nm period.

The aforementioned vacancies along the stripes, which can be observed on the previous two AFM images, may also be related to imperfections in the patterned surface of PMMA after EBL. In particular, some areas of the exposed regions of PMMA (corresponding to the Ag stripes after cluster deposition and lift-off) may not be dissolved after developing in MIBK so that the PMGI trenches are not formed at those spots. As a result, the Ag NPs could not be deposited on PMGI but on PMMA so that these NPs would be lifted off together with PMMA, leaving behind a vacancy along the stripe of NPs.

Finally, an AFM image of the last prepared sample (Ag05) is shown in Fig. 6.27.

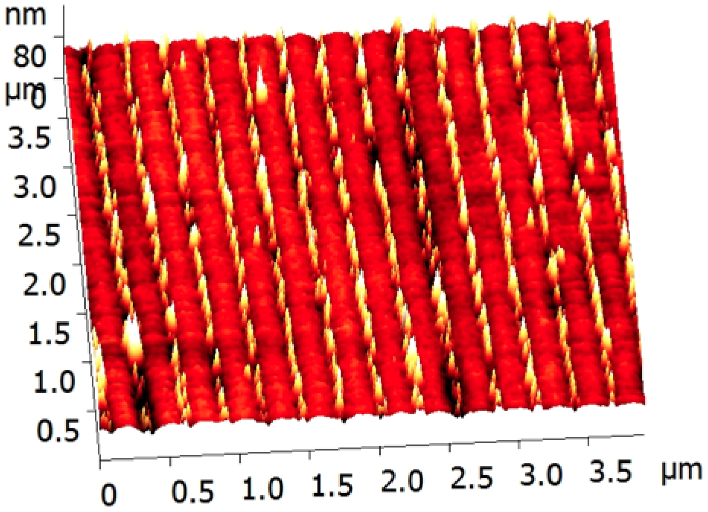

Figure 6.27. AFM image of Ag05 after lift-off showing stripes of Ag NPs with ca. 270 nm period.

The lower period for this structure (ca. 270 nm) is clearly indicated by the higher number of Ag stripes compared to the previous samples. Again, the quality of the obtained arrays is reasonable since a high fraction of the stripes is covered by Ag NPs. However, the AFM image also reveals some discontinuities along the arrays, where the Ag NPs are expected to be removed during the ultrasonic bath in acetone. Since the ultrasonic treatment was relatively short for Ag05 ($t_{us} = 1\,\mathrm{min}$), the insufficient resistance of the Ag NPs against the lift-off is probably related to the short annealing time ($t_a = 3\,\mathrm{min}$) prior to the lift-off. It is supposed that the resulting immersion of the Ag NPs into PMGI was not strong enough to ensure sufficient adhesion of the NPs. Since the AFM images of the previous samples revealed a similar tendency, a longer annealing time is suggested for the preparation of additional samples, provided that the plasmonic properties of the Ag NPs are not negatively affected. In addition, t_{us} or the ultrasonic power have to be slightly increased in order to remove the left NPs in between the stripes, as well.

6.3.2. Optical Spectroscopy

In this subsection, the plasmonic properties of the fabricated ordered arrays of Ag NPs are examined in view of potential features which distinguish them from randomly deposited Ag NPs. For instance, coupling between the NPs along and interaction between the stripes might lead to strongly enhanced local fields or the formation of additional extinction peaks in the measured spectra.

As already discussed in the previous subsection, Ag NPs were first deposited on PMGI in order to test the immersion during thermal annealing. The relative extinction spectra of both samples (Ag01 and Ag02) are presented in Fig. 6.28.

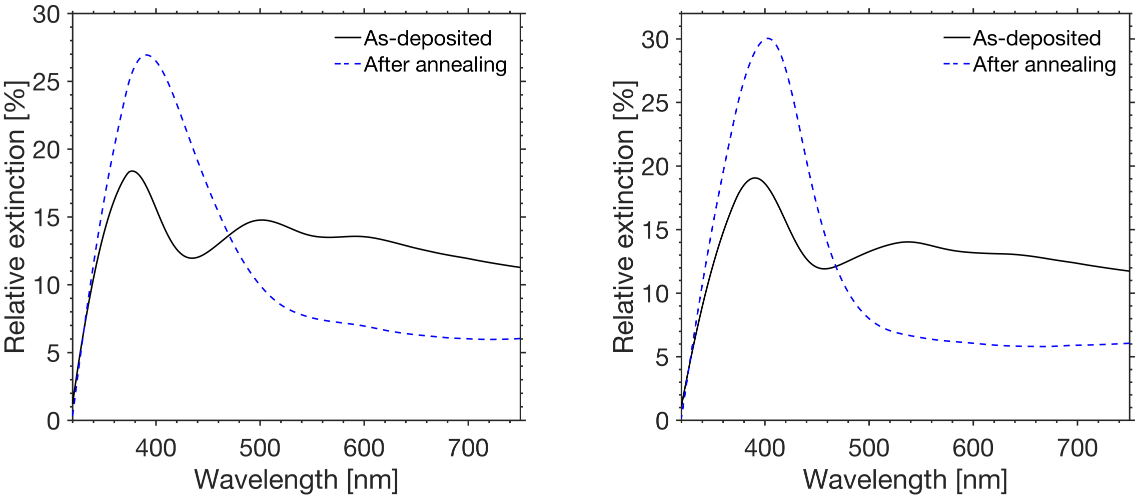

(a) Ag01. **(b)** Ag02.

Figure 6.28. Relative extinction spectra for Ag NPs on PMGI before and after thermal annealing. See Tab. 6.4 for annealing condtions.

Both Ag01 and Ag02 show pronounced plasmon bands before annealing which are redshifted after thermal annealing, accompanied by an increased intensity. Besides the confirmation for partial immersion of the Ag NPs into PMGI, the spectra also prove that the LSPR of the NPs is not damped during annealing at 190 °C for at least 5 minutes. Hence, if higher adhesion of the Ag NPs on PMGI is required for the lift-off, t_a can most likely be further increased without suppression of the LSPR.

Next, the relative extinction spectra for the samples Ag04 and Ag05 are evaluated. As already mentioned in Sec. 5.3.2, linearly polarized light (s- and p-polarized light) was used for the measurements in order to investigate the dependence of the plasmonic properties on polarization state and relative alignment of the Ag stripes. This is schematically depicted in Fig. 6.29.

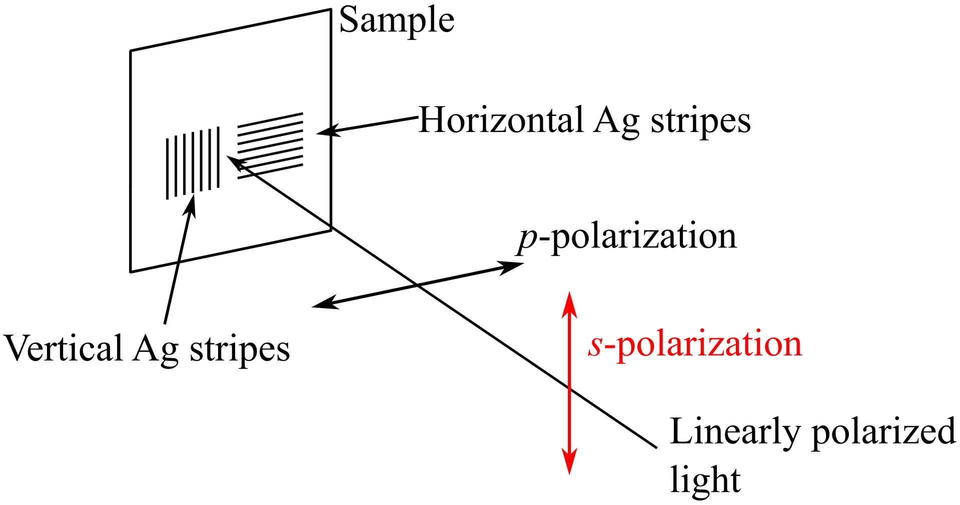

Figure 6.29. Schematic drawing showing the simplified setup for the transmittance measurements using linearly polarized light. While the arrows for the respective polarizations denote the oscillation directions of the electric field, the 2 different alignments of the Ag stripes are also shown. Hence, the measurements could be executed with 4 different combinations of polarization/Ag stripes alignment.

In Fig. 6.30, the relative extinction spectra of Ag04 are presented for the respective used light polarization and alignment of Ag NP arrays.

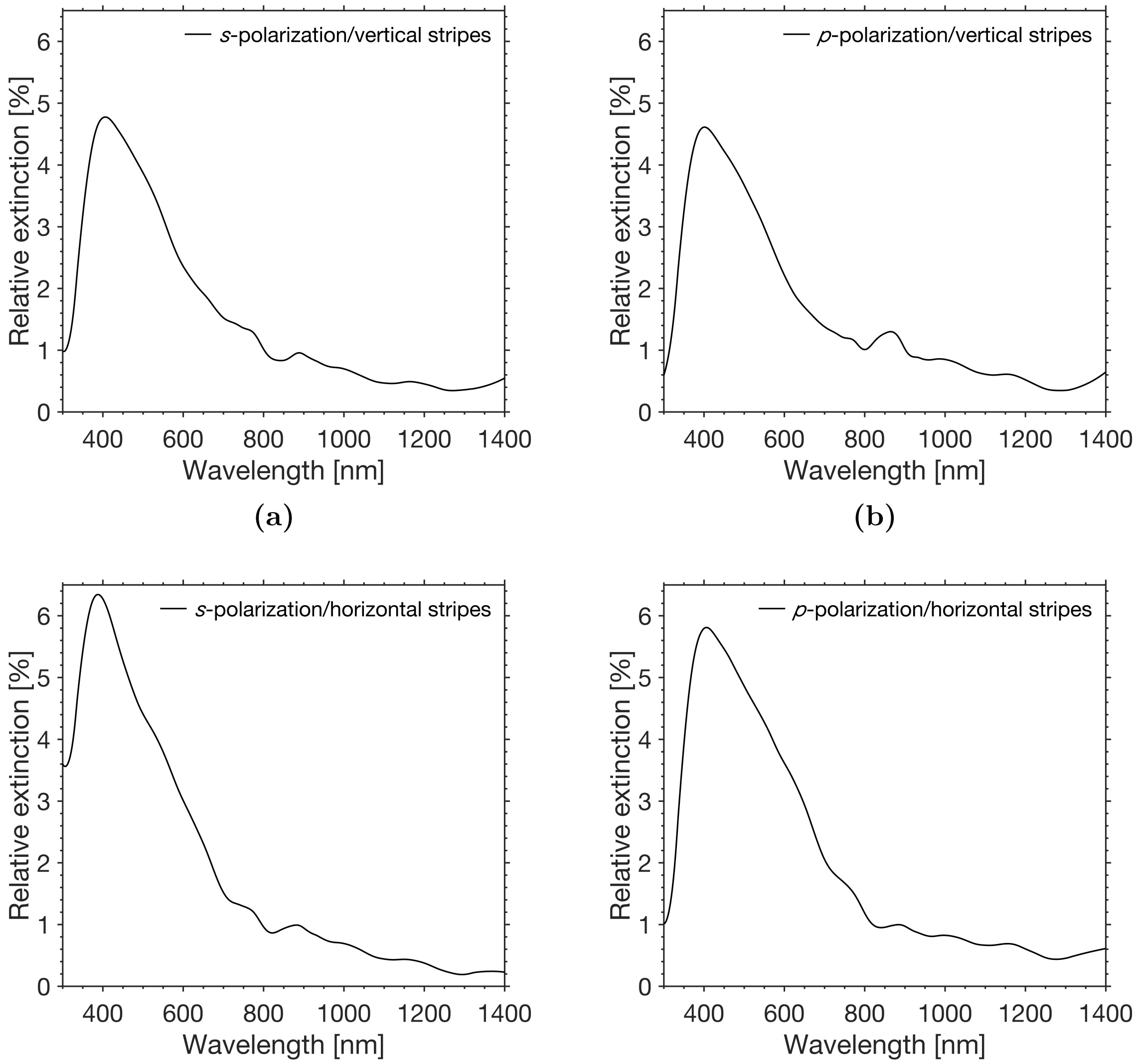

(a) **(b)**

(c) **(d)**

Figure 6.30. Relative extinction spectra of Ag arrays on PMGI (Ag04) for the 4 different polarization/array alignment combinations.

A wide wavelength range was chosen to test the spectra for potential peaks beyond the UV/VIS spectrum. All the 4 spectra show similar tendencies. First of all, the most pronounced peak located at around $\lambda = 400\,\text{nm}$ can be ascribed to the LSPR of Ag NPs. However, this peak is not symmetrical, but rather has a pronounced "shoulder" on the right hand side which is located at ca. 500-550 nm in all 4 spectra. Secondly, the spectra reveal a relatively small peak at ca. 850 nm which is related to increased noise during the measurements as the transition between the employed photodetectors occurred at this point. Hence, this peak is not considered for the further discussion. Finally, all 4 spectra exhibit relatively low intensity peaks located at ca. 1000 nm and 1180 nm, respectively. Altogether, the results in Fig. 6.30 show that the variation of polarization state and respective sample alignment does not affect the measured extinction spectra.

However, the spectra reveal the aforementioned "shoulder" at ca. 500-550 nm and two extinction peaks of relatively low intensity in the near-infrared (NIR) region. These features might be related to LSPR coupling in the investigated structure and, thus, need to be examined in more detail. First, the observed "shoulder" in the spectra of Ag04 is considered. The relative extinction spectra for Ag05 also show an asymmetrical LSPR peak with a pronounced "shoulder" at about 500-550 nm. In order to verify whether this observed feature can be assigned to coupling phenomena caused by the ordered alignment of Ag NPs (i.e. for Ag04 and Ag05), or whether it is a general phenomenon for randomly distributed Ag NPs (Ag01 and Ag02), the previous spectra are compared with the relative extinction spectra of Ag01, see Fig. 6.31.

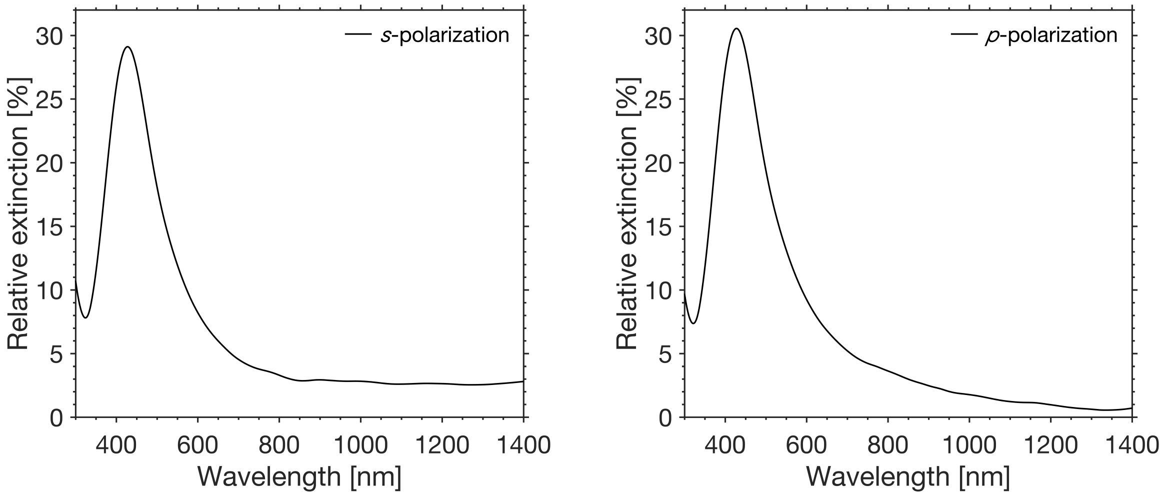

(a) **(b)**

Figure 6.31. Relative extinction spectra for partially immersed Ag NPs in PMGI (Ag01) using linearly polarized light.

The respective spectra obtained using *s*- and *p*-polarized light are very similar. Apart from the higher intensity of the plasmon band due to higher coverage, the LSPR peak is symmetrical and does not have a "shoulder". Hence, it may be suggested that the observed asymmetrical plasmon band for Ag04 and Ag05 can be assigned to the ordered alignment of Ag stripes. In particular, it is suggested that the observed "shoulder" in the extinction spectra originates from plasmonic coupling of dimers, i.e. aggregates of 2 clusters, which have formed within the arrays of Ag NPs. Consequently, the formation of dimers with elongated shape might lead to a longitudinal dipolar mode of these aggregates which results in a less pronounced plasmon band (i.e. the observed "shoulder") that is redshifted with respect to the plasmon band of the individual Ag NPs. This suggestion is supported by the extinction spectra for randomly as-deposited Ag NPs, which were presented in Fig. 6.28. It can be clearly seen that the spectra for the as-deposited Ag NPs on PMGI (Ag01 and Ag02) reveal a second plasmon band at ca. 500-550 nm, i.e. at a similar position as the above-mentioned "shoulder". Since the coverage is very high for Ag01 and Ag02 ($\approx$ 1-2 MLs), it is most likely that aggregates of 2 NPs have formed, leading to plasmonic coupling in those dimers and the observed second plasmon band. However, after annealing, the second band vanishes for the randomly deposited Ag NPs, see Fig. 6.28. The most probable reason might be that the aggregated NPs immerse individually into PMGI since this is energetically most favorable. Hence, the samples (Ag01 and Ag02) constitute exclusively (or almost exclusively) individual NPs after annealing so that plasmonic coupling is diminished and the additional plasmon band at 500-550 nm vanishes after annealing, see Fig. 6.28.

The second conspicuous feature in the presented extinction spectra of the Ag stripes (Ag04, see Fig. 6.30) includes the above-mentioned extinction peaks of relatively low intensity in the NIR region. They are examined in more detail in the wavelength range of interest (i.e. 900-1400 nm) and compared to the measured spectrum of Ag05. The obtained spectra using *p*-polarized light and vertical alignment of the Ag stripes are presented in Fig. 6.32.

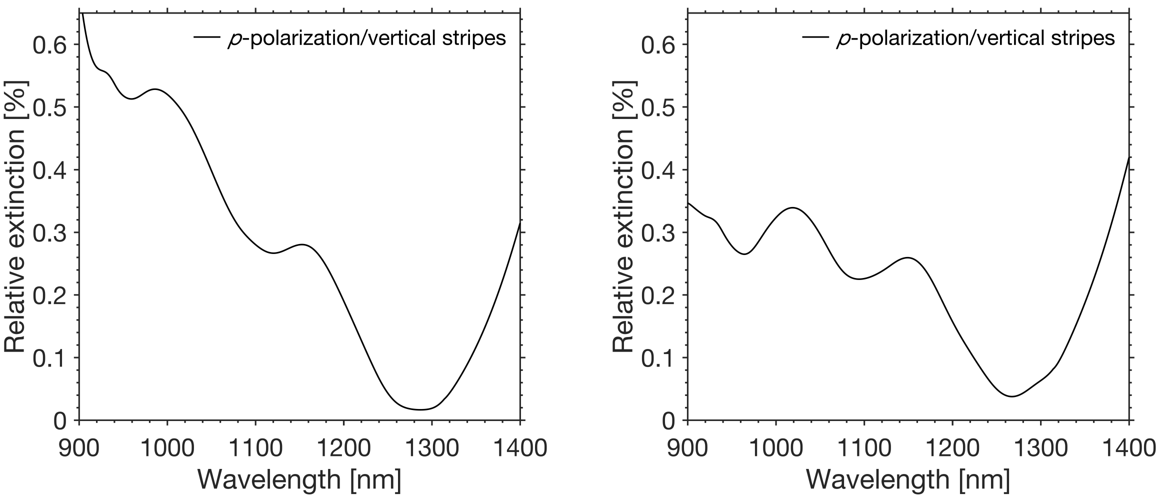

(a) Ag04.

(b) Ag05.

Figure 6.32. Relative extinction spectra for (a) Ag04 and (b) Ag05 using *p*-polarized light and vertical alignment of Ag arrays.

Both spectra show extinction peaks at about 1000 nm and 1170 nm, respectively. Measurements with different combinations of polarization/sample alignment yield similar results. Thus, the periodicity of the fabricated arrays of Ag NPs does not seem to affect the measured extinction spectra. Again, the obtained spectra for the Ag stripes are compared with relative extinction spectra for Ag NPs randomly deposited on PMGI (Ag01) which were partially embedded after thermal annealing, see Fig. 6.33.

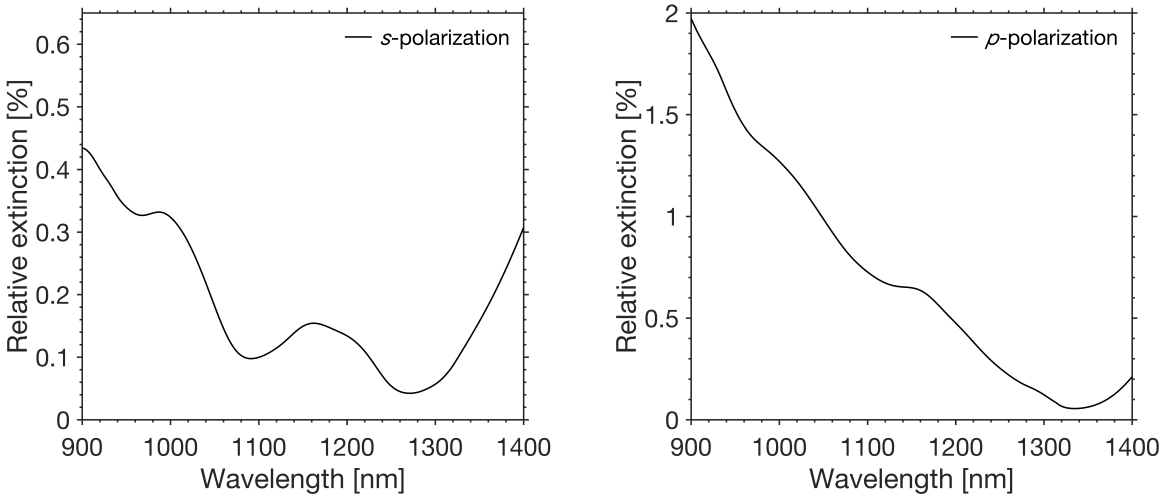

(a) **(b)**

Figure 6.33. Relative extinction spectra for partially immersed Ag NPs in PMGI (Ag01) using linearly polarized light.

The aforementioned peaks can also be observed for the randomly distributed Ag NPs on PMGI. Hence, they constitute a general phenomenon and are not characteristic for the fabricated structures with ordered arrays of Ag NPs. In summary, the transmittance measurements reveal an asymmetrical plasmon band with a pronounced "shoulder" at about 500-550 nm which is expected to be related to plasmonic coupling in dimers which have formed within the Ag stripes. Additional extinction peaks cannot be associated with coupling effects within or between the Ag arrays. More detailed study of the samples is required, e.g. different type of measurement or modified experimental setups, in order to obtain more information about the optical properties. Furthermore, the fabrication process has to be optimized in order to enhance the quality of the Ag stripes.

Chapter 7

Conclusions

As the very first and important stage, the calibration of EQMS for the case of Cu clusters was carried out. In particular, the dependence of particle size on the applied voltage was determined allowing to obtain and deposit the clusters of desired sizes. In addition, the cluster size selection is found to be reasonably good and stays constant for the entire size range of examined clusters ($\approx$ 7-30 nm) with 6.0-9.5% precision of the cluster height. This is in good agreement with a previous study of the size-selection for Ag NPs demonstrating a standard deviation within 7.0%, thus, confirming the repeatability of size selection for different metals.

Dynamics of copper cluster embedding into polymer films using thermal annealing is studied. By creating a small orientation mark in the center of a Si substrate employing FIB milling, it was possible to study the immersion of specific Cu NPs into PMMA during thermal annealing. AFM study of the sample shows that the NPs quickly immerse into the polymer within the first minutes of annealing, before the embedding process slows down drastically. After 1 hour, the NPs are partially immersed by about 5/6 of their height, corresponding to their final embedding depth. This is in contradiction to a number of experimental studies reporting full immersion of metal NPs into polymers. A final conclusion about the origin cannot be drawn. However, it is suggested that the value for the surface tension of Cu NPs might be smaller than the reported one due to nanosize effects or chemical reaction of the Cu NPs with ambient gases during annealing. Consequently, this would lead to a smaller driving force for NP embedding so that the Cu NPs become only partially embedded.

Transmittance measurements were carried out on the prepared samples. It is found that thermal annealing leads to quenching of the LSPR along with NP immersion into the polymer films. It is expected that this is related to enhanced chemical reactivity of Cu NPs with species present in ambient air (particularly oxygen) at elevated temperatures, leading to continuous conversion of Cu to copper oxide NPs and the accompanied damping of the plasmonic properties. A simple treatment method is proposed to preserve the LSPR of Cu NPs during thermal annealing. Prior to annealing, the NPs are treated in ozone environment to form a protective oxide shell which is supposed to efficiently reduce the diffusion of oxygen atoms to the Cu core and, thus, slow down the degradation considerably. This is successfully demonstrated for both Cu NPs deposited on bare and polymer-covered substrates as the plasmonic properties are preserved after thermal annealing and long-term storage in ambient atmosphere for several weeks. Thus, the proposed ozone treatment represents a simple, but efficient procedure to protect Cu NPs against environmental factors causing degradation of the plasmonic properties.

In the second part, ordered stripes of Ag NPs with varying periodicity were successfully fabricated combining the cluster deposition with electron beam lithography. Transmittance measurements were conducted using linearly polarized light and reveal an asymmetrical plasmon band with pronounced "shoulder" located at ca. 500-550 nm. It is suggested that this "shoulder" arises from plasmonic coupling in aggregates of 2 NPs which have formed within the Ag stripes. The resulting longitudinal dipolar mode for the elongated aggregates leads to the observed "shoulder" which is redshifted with respect to the plasmon band of individual Ag NPs. More detailed optical measurements are required in order to obtain more information about the optical properties. After optimization of the procedure for fabrication of the Ag stripes, the used approach can also be applied to produce other structures, e.g. ordered NP arrays with circular or square pattern.

BIBLIOGRAPHY

[1] V.N. Popok, I. Barke, E.E.B. Campbell, and K.-H. Meiwes-Broer. Cluster-surface interaction: From soft landing to implantation. *Surf. Sci. Rep.*, 66:347–377, 2011.

[2] B. von Issendorff and O. Cheshnovsky. Metal to insulator transitions in clusters. *Annu. Rev. Phys. Chem.*, 56:549–580, 2005.

[3] D. Astruc, editor. *Nanoparticles and Catalysis*. Wiley-VCH, 2008.

[4] M. Okumura, Y. Kitagawa, M. Haruta, and K. Yamaguchi. DFT studies of interaction between O_2 and Au clusters. The role of anionic surface Au atoms on Au clusters for catalyzed oxygenation. *Chem. Phys. Lett.*, 346(1-2):163–168, 2001.

[5] H. Haberland. *Clusters of Atoms and Molecules - Theory, Experiment, and Clusters of Atoms*. Springer-Verlag, 1994.

[6] N. Toshima, Y. Shiraishi, and T. Teranishi. Effect of additional metal ions on catalyses of polymer-stabilized metal nanoclusters. *J. Mol. Catal. A: Chem.*, 177(1):139–147, December 2001.

[7] J. Conde, G. Doria, and P. Baptista. Noble metal nanoparticles applications in cancer. *Journal of Drug Delivery*, 2012:1–12, 2012.

[8] E. Weir, A. Lawlor, and F. Regan. The use of nanoparticles in anti-microbial materials and their characterization. *Analyst*, 133(7):835–845, July 2008.

[9] H. Graf, J. Vancea, and H. Hoffmann. Single-electron tunneling at room temperature in cobalt nanoparticles. *Appl. Phys. Lett.*, 80(7):1264–1266, 2002.

[10] S.A. Brown, J. van Litha, and A. Lassessona. Hydrogen Sensors Based on Percolation and Tunneling in films of Palladium Clusters. *Proc. of SPIE*, 6800:1–13, 2008.

[11] L. Ravagnan, G. Corbelli, C. Ghisleri, M. Marelli, and P. Milani. Highly deformable Nanostructured Elastomeric Electrodes With Improving Conductivity Upon Cyclical Stretching. *Adv. Mater.*, 23:4504–4508, 2011.

[12] C.B. Murray, Shouheng Sun, Hugh Doyle, and T. Betley. Monodisperse 3d Transition-Metal (Co,Ni,Fe) Nanoparticles and Their Assembly into Nanoparticle Superlattices. *MRS Bull.*, 26(12):985–991, December 2001.

[13] F. Faupel, V. Zaporojtchenko, H. Greve, U. Schürmann, V.S.K. Chakravadhanula, C. Hanisch, A. Kulkarni, A. Gerber, E. Quandt, and R. Podschun. Deposition of Nanocomposites by Plasmas. *Contrib. Plasma Phys.*, 47(7):537–544, 2007.

[14] P. Fojan, M. Hanif, S. Bartling, H. Hartmann, I. Barke, and V. Popok. Supported silver clusters as nanoplasmonic transducers for protein sensing. *Sens. Actuators, B*, 212:377–381, 2015.

[15] J. Kneipp, H. Kneipp, B. Wittig, and K. Kneipp. Novel optical nanosensors for probing and imaging live cells. *Nanomedicine: Nanotechnology, Biology, and Medicine*, 6:214–226, 2010.

[16] M. Hanif, R.R. Juluri, M. Chirumamilla, and V.N. Popok. Poly(methyl methacrylate) Composites with Size-selected Silver Nanoparticles Fabricated Using Cluster Beam Technique. *J. Polym. Sci., Part B: Polym. Phys.*, 54(12):1152–1159, 2016.

[17] P. Milani, C. Ghisleri, F. Borghi, L. Ravagna, A. Podestà, C Melis, and L. Colombo. Patterning of gold-polydimethylsiloxane (Au-PDMS) nanocomposites by supersonic cluster beam implantation. *J. Phys. D: Appl. Phys.*, 47:1–10, 2014.

[18] R.L. Johnston. *Atomic and Molecular Clusters.* CRC Press, April 2002.

[19] W.A. de Heer. The physics of simple metal clusters: experimental aspects and simple models. *Rev. Mod. Phys.*, 65(3):611–675, 1993.

[20] F. Bakhtar, J.B. Young, A.J. White, and D.A. Simpson. Classical nucleation theory and its application to condensing steam flow calculations. *Journal of Mechanical Engineering Science*, 219(12):1315–1333, December 2005.

[21] M. Volmer and A. Weber. Keimbildung in übersattigten Gebilden. *Z. Phys. Chem.*, 119:277–301, 1926.

[22] R. Becker and W. Döring. Kinetische Behandlung der Keimbildung in übersattingten Dämfen. *Ann. Phys.*, 24:719–752, 1935.

[23] L. Farkas. Keimbildungsgeschwindigkeit in übersättigten Dämpfen. *Z. Phys. Chem.*, 125:236–242, 1927.

[24] W. Band. Dissociation treatment of condensing systems. *J. Chem. Phys.*, 7:324–326, 1939.

[25] A. Bijl. *Discontinuities in the energy and specific heats.* PhD thesis, University of Leiden, 1938.

[26] B.M. Smirnov. *Nanoclusters and Microparticles in Gases and Vapors.* De Gruyter, 2012.

[27] P.V. Kashtanov, B.M. Smirnov, and R. Hippler. Magnetron plasma and nanotechnology. *Phys. Usp.*, 50(5):455–488, 2007.

[28] B.M. Smirnov. Processes Involving Clusters and Small Particles in a Buffer Gas. *Phys. Usp.*, 54:691–721, 2011.

[29] T.P. Martin. Shells of atoms. *Phys. Rep.*, 273:199–241, 1996.

[30] W.D. Knight, K. Clemenger, W.A. de Heer, W.A. Saunders, M.Y. Chou, and M.L. Cohen. Electronic Shell Structure and Abundances of Sodium Clusters. *Phys. Rev. Lett.*, 54(24):2141–2143, 1984.

[31] A. Šiber. Vibrations of closed-shell Lennard-Jones icosahedral and cuboctahedral clusters and their effect on the cluster ground-state energy. *Phys. Rev. B*, 70:1–7, 2004.

[32] G.H. Guvelioglu, P. Ma, X. He, R.C. Forrey, and H. Cheng. First principles studies on the growth of small Cu clusters and the dissociative chemisorption of H_2. *Phys. Rev. B*, 73:1–10, 2006.

[33] V.L. Mazalova and A.V. Soldatov. Geometrical and electronic structure of small copper nanoclusters: XANES and DFT analysis. *J. Struct. Chem.*, 49:107–115, 2008.

[34] M. Kabir, A. Mookerjee, and A.K. Bhattacharya. Structure and stability of copper clusters: A tight-binding molecular dynamics study. *Phys. Rev. A*, 69:1–10, 2004.

[35] B.J. Winter, E.K. Parks, and S.J. Riley. Copper clusters: The interplay between electronic and geometrical structure. *J. Chem. Phys.*, 94:8618–8621, 1991.

[36] D. Reinhard, B.D. Hall, P. Berthoud, S. Valkealahti, and R. Monot. Size-Dependent Icosahedral-to-fcc Structure Change Confirmed in Unsupported Nanometer-Sized Copper Clusters. *Phys. Rev. Lett.*, 79(8):1459–1462, 1997.

[37] M. Kuno. *Introductory Nanoscience: Physical and Chemical Concepts.* Taylor & Francis Inc, 2001.

[38] F. Baletto, R. Ferrando, A. Fortunelli, F. Montalenti, and C. Mottet. Crossover among structural motifs in transition and noble-metal clusters. *J. Chem. Phys.*, 116:3856–3863, 2002.

[39] D. Reinhard, B.D. Hall, D. Ugarte, and R. Monot. Size-independent fcc-to-icosahedral structural transition in unsupported silver clusters: An electron diffraction study of clusters produced by inert-gas aggregation. *Phys. Rev. B*, 55:7868–7881, 1997.

[40] I. Barke, H. Hartmann, D. Rupp, L. Flückiger, M. Sauppe, M. Adolph S. Schorb, C. Bostedt, R. Treusch, C. Peltz S. Bartling, T. Fennel, K.-H. Meiwes-Broer, and T. Möller. The 3D-architecture of individual free silver nanoparticles captured by x-ray scattering. *Nat. Commun.*, 6:1–7, 2015.

[41] H. Hartmann, V.N. Popok, I. Barke, V. von Oeynhausen, and K.-H. Meiwes-Broer. Design and capabilities of an experimental setup based on magnetron sputtering for formation and deposition of size-selected metal clusters on ultra-clean surfaces. *Rev. Sci. Instrum.*, 83:1–6, 2012.

[42] J. Blackman. *Handbook of Metal Physcis, Volume 5. Metallic Nanoparticles.* Elsevier, 2008.

[43] J. Jortner. Cluster size effects. *Z. Phys. D. - Atoms, Molecules and Clusters*, 24:247–275, 1992.

[44] H. Haberland, T. Hippler, J. Donges, O. Kostko, M. Schmidt, and B. von Issendorff. Melting of Sodium Clusters: Where Do the Magic Numbers Come from? *Phys. Rev. Lett.*, 94:1–4, 2005.

[45] P. Braunstein, L.A. Oro, and P.R. Raithby. *Metal Clusters in Chemistry.* WILEY-VCH Verlag GmbH, 1999.

[46] S.K. Ghosh. Kubo Gap as a Factor Governing the Emergence of New Physicochemical Characteristics of the Small Metallic Particulates. *Journal of Science and Technology: Physical Sciences and Technology*, 7(2):114–121, 2011.

[47] E. Barborini, G. Corbelli, G. Bertolini, P. Repetto, M. Leccardi, S. Vinati, and P. Milani. The influence of nanoscale morphology on the resistivity of cluster-assembled nanostructured metallic thin films. *New J. Phys.*, 12:1–12, 2010.

[48] M.C. Salvadori, M. Cattani, F.S. Teixeira, and I.G. Brown. Conducting polymer formed by low energy gold ion implantation. *Appl. Phys. Lett.*, 93:1–3, 2008.

[49] D. Stauffer and A. Aharony. *Introduction to Percolation Theory.* Francis & Taylor, 2nd edition, 2003.

[50] V.N. Popok. Ion Implantation of Polymers: Formation of Nanoparticulate Materials. *Reviews on Advanced Materials Science*, 30(1):1–26, 2012.

[51] F. Faupel, V. Zaporojtchenko, T. Strunskus, and M. Elbahri. Metal-Polymer Nanocomposites for Functional Applications. *Adv. Eng. Mater.*, 12(12):1177–1190, 2010.

[52] M. Niklaus and H.R. Shea. Electrical conductivity and Young's modulus of flexible nanocomposites made by metal-ion implantation of polydimethylsiloxane: The relationship between nanostructure and macroscopic properties. *Acta Mater.*, 59(2):830–840, 2011.

[53] J.-W. Lim and M. Isshiki. Electrical resistivity of Cu films deposited by ion beam deposition: effects of grain size, impurities, and morphological defect. *J. Appl. Phys.*, 99(9):1–7, 2006.

[54] M.I. Stockmann. Nanoplasmonics: The physics behind the applications. *Phys. Today*, 64:39–44, 2011.

[55] K.Y. Kim. *Plasmonics - Principles and Applications.* InTech, 2012.

[56] S.A. Maier. *Plasmonics: Fundamentals and Applications.* Springer Science, 2007.

[57] P.B. Johnson and R.W. Christy. Optical Constants of the Noble Metals. *Phys. Rev. B*, 6(12):4370–4379, 2012.

[58] P.K. Jain, K.S. Lee, I.H. El-Sayed, and M.A. El-Sayed. Calculated Absorption and Scattering Properties of Gold Nanoparticles of Different Size, Shape, and Composition: Applications in Biological Imaging and Biomedicine. *J. Phys. Chem. B*, 110(4):7238–7248, 2006.

[59] K.-H. Meiwes-Broer. *Metal Clusters at Surfaces - Structure, Quantum Properties, Physical Chemistry.* Springer, 2000.

[60] B. Di Bartolo, J. Collins, and L. Silvestri, editors. *Nano-Structures for Optics and Photonics: Optical Strategies for Enhancing Sensing, Imaging, Communication and Energy Conversion*, chapter Cluster Implantation and Deposition Apparatus: Design and Capabilities. Springer Science, 2015.

[61] C. Binns. Nanoclusters deposited on surfaces. *Surf. Sci. Rep.*, 44:1–49, 2001.

[62] B. Nacer, C. Massobrio, and C. Félix. Deposition of metallic clusters on a metallic surface at zero initial kinetic energy: Evidence for implantation and site exchanges. *Phys. Rev. B*, 56:10590–10595, 1997.

[63] A. Kleibert, A. Voitkans, and K.-H. Meiwes-Broer. Reflection high energy electron diffraction as a tool in cluster deposition experiments. *physica status solidi (b)*, 247(5):1048–1055, 2010.

[64] T. Lünskens, P. Heister, M. Thämer, C.A. Walenta, A. Kartouzian, and U. Heiza. Plasmons in supported size-selected silver nanoclusters. *Phys. Chem. Chem. Phys.*, 17:17541–17544, 2015.

[65] A. Perez, P. Melinon, V. Dupuis, P. Jensen, B. Prevel, J. Tuaillon, L. Bardotti, C. Martet, M. Treilleux, and M. Broyer. Cluster assembled materials: a novel class of nanostructured solids with original structures and properties. *J. Phys. D: Appl. Phys.*, 30(5):709–721, 1997.

[66] L. Bardotti, P. Jensen, A. Hoareau, M. Treilleux, and B. Cabaud. Experimental Observation of Fast Diffusion of Large Antimony Clusters on Graphite Surfaces. *Phys. Rev. Lett.*, 74(23):4694–4697, 1995.

[67] R. Gomer. Diffusion of adsorbates on metal surfaces. *Rep. Prog. Phys.*, 53(7):917–1002, 1990.

[68] J.-M. Wen, S.-L. Chang, J.W. Burnett, J.W. Evans, and P.A. Thiel. Diffusion of Large Two-Dimensional Ag Clusters on Ag(100). *Phys. Rev. Lett.*, 73:2591–2594, 1994.

[69] P. Moriarty, Y.R. Ma, M.D. Upward, and P.H. Beton. Translation, rotation and removal of C60 on Si(100)-2x1 using anisotropic molecular manipulation. *Surf. Sci.*, 407(1-3):27–35, 1998.

[70] R. Guerra, U. Tartaglino, A. Vanossi, and E. Tosatti. Ballistic nanofriction. *Nat. Mater.*, 9:634–637, 2010.

[71] M.R. Falvo, J. Steele, R.M. Taylor II, and R. Superfine. Gearlike rolling motion mediated by commensurate contact: Carbon nanotubes on HOPG. *Phys. Rev. B*, 62:10665–10667, 2000.

[72] P. Jensen. Growth of nanostructures by cluster deposition: Experiments and simple models. *Rev. Mod. Phys.*, 71:1695–1735, 1999.

[73] B. Yoon, V.M. Akulin, Ph. Cahuzac, F. Carlier, M. de Frutos, A. Masson, C. Moryb, C. Colliex, and C. Bréchignac. Morphology control of the supported islands grown from soft-landed clusters. *Surf. Sci.*, 443(1-2):76–88, 1999.

[74] S.J. Carroll, R.E. Palmer, P.A. Mulheran, S. Hobday, and R. Smith. Deposition and diffusion of size-selected (Ag400+) clusters on a stepped graphite surface. *Appl. Phys. A*, 67(6):613–619, 1998.

[75] T. Michel, M. Winkler, H. Werner, and H. Fecht, editors. *Metal/polymer interfaces and composite materials prepared by vapor phase deposition.* ddp goldenbogen, 2000.

[76] A. Biswas, Z. Marton, J. Kanzow, J. Kruse, F. Faupel V. Zaporojtchenko, and T. Strunskus. Controlled Generation of Ni Nanoparticles in the Capping Layers of Teflon AF by Vapor-Phase Tandem Evaporation. *Nano Lett.*, 3(1):69–73, 2003.

[77] H. Takele, H. Greve, C. Pochstein, V. Zaporojtchenko, and F. Faupel. Plasmonic properties of Ag nanoclusters in various polymer matrices. *Nanotechnology*, 17:3499–3505, 2006.

[78] S. Demming, A. Hahn, A. Edlich, E. Franco-Lara, R. Krull, S. Barcikowski, and S. Buttgenbach. Softlithographic, partial integration of surface-active nanoparticles in a PDMS matrix for microfluidic biodevices. *Phys. Status Solidi A*, 207:898–903, 2010.

[79] V.N. Popok, M. Hanif, A. Mackova, and R. Mikšovå. Structure and Plasmonic Properties of Thin PMMA Layers with Ion-Synthesized Ag Nanoparticles. *J. Polym. Sci., Part B: Polym. Phys.*, 53:664–672, 2015.

[80] G.J. Kovacs and P.S. Vincett. Subsurface Particle Monolayer and Film Formation in Softenable Substrates: Techniques and Thermodynamic Criteria. *Thin Solid Films*, 111(1):65–81, 1984.

[81] G.J. Kovacs and P.S. Vincett. Formation and Thermodynamic Stability of a Novel Class of Useful Materials: Close-Packed Monolayers of Submicron Monodisperse Spheres Just below a Polymer Surface. *J. Colloid Interface Sci.*, 90(2):335–351, 1982.

[82] Prakash, A. Tripathi, S. Gautam, K.H. Chae, J. Song, V. Rigato, J. Tripathi, and K. Asokan. Phenomenological understanding of dewetting and embedding of noble metal nanoparticles in thin films induced by ion irradiation. *Mater. Chem. Phys.*, 147:920–924, 2014.

[83] Devendra Gupta, editor. *Diffusion Processes in Advanced Technological Materials.* Springer, 2005.

[84] J. Prakash, J.C. Pivin, and H.C. Swart. Noble metal nanoparticles embedding into polymeric materials: From fundamentals to applications. *Adv. Colloid Interface Sci.*, 226:187–202, 2015.

[85] F. Faupel, J. Erichsen, J. Kanzow, U. Schürmann, K. Dolgner, K. Günther-Schade, T. Strunskus, and V. Zaporojtchenko. Investigation of the Surface Glass Transition Temperature by Embedding of Noble Metal Nanoclusters into Monodisperse Polystyrenes. *Macromolecules*, 37:1831–1838, 2004.

[86] R. Weber, I. Grotkopp, J. Stettner, M. Tolan, and W. Press. Embedding of Gold Nanoclusters on Polystyrene Surfaces: Influence of the Surface Modification on the Glass Transition. *Macromolecules*, 36:9100–9106, 2003.

[87] F. Ruffino, V. Torrisi, G. Marletta, and M.G. Grimaldi. Effects of the embedding kinetics on the surface nano-morphology of nano-grained Au and Ag films on PS and PMMA layers annealed above the glass transition temperature. *Appl. Phys. A*, 107:669–683, 2012.

[88] G. Amarandei, I. Clancy, C. O'Dwyer, A. Arshak, and D. Corcoran. Stability of Ultrathin Nanocomposite Polymer Films Controlled by the Embedding of Gold Nanoparticles. *Applied Materials & Interfaces*, 6:20758–20767, 2014.

[89] G. Amarandei, C. O'Dwyer, A. Arshak, and D. Corcoran. The stability of thin polymer films as controlled by changes in uniformly sputtered gold. *Soft Matter*, 9:2695–2702, 2013.

[90] V. Zaporojtchenko, T. Strunskus, J. Erichsen, and F. Faupel. Embedding of Noble Metal Nanoclusters into Polymers as a Potential Probe of the Surface Glass Transition. *Macromolecules*, 34(5):1125–1127, 2001.

[91] S.M. Aharoni. On entanglements of flexible and rodlike polymers. *Macromolecules*, 16(11):1722–1728, 1983.

[92] J.A. Forrest, J.S. Sharp, and J.H. Teichroeb. The properties of free polymer surfaces and their influence on the glass transition temperature of thin polystyrene films. *Eur. Phys. J. E*, 15:473–487, 2004.

[93] J. A. Forrest, Y. Chai, T. Salez, J.D. McGraw, M. Benzaquen, K. Dalnoki-Veress, and E. Raphaël. A Direct Quantitative Measure of Surface Mobility in a Glassy Polymer. *Science*, 343:994–999, 2014.

[94] M.D. Ediger K. Paeng and R. Richert. Molecular mobility in supported thin films of polystyrene, poly(methylmethacrylate), and poly(2-vinyl pyridine) probed by dye reorientation. *Soft Matter*, 8:819–826, 2012.

[95] R.D. Deshmukh and R.J. Composto. Direct Observation of Nanoparticle Embedding into the Surface of a Polymer Melt. *Langmuir*, 23(26):13169–13173, 2007.

[96] O. Polonskyi, O. Kylián, M. Drábik, J. Kousal, P. Solař, A. Artemenko, J. Čechvala, A. Choukourov, D. Slavínská, and H. Biederman. Deposition of Al nanoparticles and their nanocomposites using a gas aggregation cluster source. *J. Mater. Sci.*, 49:3352–3360, 2014.

[97] O. Polonskyi, P. Solař, O. Kylián, M. Drábik, A. Artemenko a, J. Kousal, J. Hanuš, J. Pešička, I. Matolínová, E. Kolíbalová, D. Slavínská, and H. Biederman. Nanocomposite metal/plasma polymer films prepared by means of gas aggregation cluster source. *Thin Solid Films*, 520:4155–4162, 2012.

[98] O. Kylián, J. Kratochvíl, J. Hanuš, O. Polonskyi, P. Solař, and H. Biederman. Fabrication of Cu nanoclusters and their use for production of Cu/plasma polymer nanocomposite thin films. *Thin Solid Films*, 550:46–52, 2014.

[99] A. Artemenko. *XPS analysis of plasma polymers and nanocomposite films without breaking vacuum.* PhD thesis, Charles University in Prague, Faculty of Mathematics and Physics, 2013.

[100] O. Kylián, A. Shelemin, P. Solař, A. Choukourov, J. Hanuš, M. Vaidulych, A. Kuzminova, and H. Biederman. Plasma polymers: From thin films to nanocolumnar coatings. *Thin Solid Films*, pages 1–6, 2016.

[101] H. Biederman, J. Hanuš, T. Steinhartová, O. Kylián, J. Kousal, P. Malinský, A. Choukourov, and A. Macková. Deposition of Cu/a-C:H Nanocomposite Films. *Plasma Process. Polym.*, 13:879–887, 2016.

[102] O. Kylián, A.Kuzminova, J. Beranová, O. Polonskyi, A. Shelemin, A. Choukourov, D. SlavÌnská, and H. Biederman. Antibacterial nanocomposite coatings produced by means of gas aggregation source of silver nanoparticles. *Surface & Coatings Technology*, 294:225–230, 2016.

[103] P. Milani and C. Minnai. Metal-polymer nanocomposite with stable plasmonic tuning under cyclic strain conditions. *Applied Physics Letters*, 107:1–4, 2015.

[104] M. Hanif. *Synthesis of Nanostructured Materials Using Metal Cluster Ion Beams.* PhD thesis, Aalborg University, January 2016.

[105] G. Binnig, C.F. Quate, and C. Gerber. Atomic Force Microscope. *Phys. Rev. Lett.*, 56(930):930–933, 1986.

[106] V.L. Mironov. *Fundamentals of scanning probe microscopy.* NT-MDT, 2004.

[107] N. Tkachenko. *Optical Spectroscopy.* Elsevier Science, 1st edition, 2006.

[108] F. Aqra and A.H. Ayyad. Surface free energy of alkali and transition metal nanoparticles. *Appl. Surf. Sci.*, 314:308–313, 2014.

[109] M. Harris, G. Appel, and H. Ade. Surface Morphology of Annealed Polystyrene and Poly(methyl methacrylate) Thin Film Blends and Bilayers. *Macromolecules*, 36:3307–3314, 2003.

[110] S. Wu. Surface and interfacial tensions of polymer melts. II. Poly(methyl methacrylate), poly(n-butyl methacrylate), and polystyrene. *J. Phys. Chem.*, 74(3):632–638, 1970.

[111] K.K. Nanda, A. Maisels, F.E. Kruis, H. Fissan, and S. Stappert. Higher Surface Energy of Free Nanoparticles. *Phys. Rev. Lett.*, 91(10):1–4, 2003.

[112] S. Xiong, W. Qi, Y. Cheng, B. Huang, M. Wang, and Y. Li. Modeling size effects on the surface free energy of metallic nanoparticles and nanocavities. *Phys. Chem. Chem. Phys.*, 13:10648–10651, 2011.

[113] W.M. Haynes. *CRC Handbook of Chemistry and Physics.* CRC Press, 2002.

[114] A. Moores and F. Goettmann. The plasmon band in noble metal nanoparticles: an introduction to theory and applications. *New J. Chem.*, 30:1121–1132, 2006.

[115] K.L. Kelly, E. Coronado, L.L. Zhao, and G.C. Schatz. The Optical Properties of Metal Nanoparticles: The Influence of Size, Shape, and Dielectric environment. *J. Phys. Chem. B*, 107:668–677, 2003.

[116] A. Curry, G. Nusz, A. Chilkoti, and A. Wax. Substrate effect on refractive index dependence of plasmon resonance for individual silver nanoparticles observed using darkfield micro-spectroscopy. *Opt. Express*, 13(7):2668–2677, 2005.

[117] V.G. Kravets, R. Jalil, Y.-J. Kim, D. Ansell, D.E. Aznakayeva, B. Thackray, L. Britnell, B.D. Belle, F. Withers, I.P. Radko, Z. Han, S.I. Bozhevolnyi, K.S. Novoselov, A.K. Geim, and A.N. Grigorenko. Graphene-protected copper and silver plasmonics. *Sci. Rep.*, 4(5517):1–8, 2014.

[118] M. Shi, H.S. Kwon, Z. Peng, A. Elder, and H. Yang. Effects of Surface Chemistry on the Generation of Reactive Oxygen Species by Copper Nanoparticles. *ACS Nano*, 6(3):2157–2164, 2012.

[119] N. Tajima, M. Fukui, Y. Shintani, and O. Tada. *In Situ* Studies on Oxidation of Copper Films By Using ATR Technique. *J. Phys. Soc. Jpn.*, 54:4236–4240, 1985.

Appendices

Appendix A

Article: Immersion of low-energy deposited metal clusters into poly(methyl methacrylate)

Contents lists available at ScienceDirect

Nuclear Instruments and Methods in Physics Research B

journal homepage: www.elsevier.com/locate/nimb

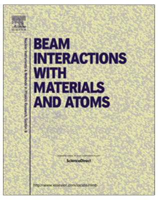

Immersion of low-energy deposited metal clusters into poly(methyl methacrylate)

V.N. Popok [a,*], M. Hanif [b], F.A. Ceynowa [a], P. Fojan [a]

[a] *Department of Physics and Nanotechnology, Aalborg University, Skjernvej 4A, 9220 Aalborg, Denmark*
[b] *Interdisciplinary Nanoscience Center (iNANO), Aarhus University, Gustav Wieds Vej 14, 8000 Aarhus, Denmark*

ARTICLE INFO

Article history:
Received 7 December 2016
Received in revised form 24 April 2017
Accepted 5 May 2017
Available online xxxx

Keywords:
Cluster beam technique
Metal nanoparticles
Polymer films
Localised surface plasmon resonance

ABSTRACT

Immersion of size-selected metal clusters deposited on thin poly(methyl methacrylate) (PMMA) films is studied. Clusters are produced by magnetron sputtering and soft-landed on the polymer substrates. It is found that thermal annealing at temperatures above the polymer glass transition point facilitates embedment of the deposited nanoparticles (NPs) into PMMA. The immersion degree can be controlled by the annealing time. Together with the control of cluster coverage by tuning the deposition time, the described approach represents an efficient method for the formation of thin polymer composite layers with embedded size-selected metal NPs. In the case of silver, the composite films demonstrate excellent plasmonic properties. However, the thermal annealing is found to quench the plasmon resonance of copper NPs. It is suggested that oxidation under elevated temperatures is the most probable mechanism destroying the plasmonic properties of the copper NPs. A simple treatment method by ozone is proposed to form an oxide shell around the metal core, thus, protecting the core against environmental factors causing degradation of the plasmonic properties.

1. Introduction

Polymer films with embedded metal nanoparticles (NPs) are of significant interest due to a number of applications in research and industry [1,2]. This includes different possibilities. (i) To control conductivity by varying a metal filling factor in polymers, thus, allowing to tune the charge carrier transport from variable range hopping towards percolation and insulator-to-metal transition [3–5]. (ii) To form media with ferromagnetic single domain behaviour or superparamagnetism [6,7]. (iii) To synthesise polymer composites utilizing localised surface plasmon resonance (LSPR) of noble metal NPs [8] giving rise to applications in sensor technologies [9,10], fabrication of plasmon resonators demonstrating enormous enhancement of quantum emitter's fluorescence [11,12], thus, facilitating the development of ultra-bright and stable single-photon sources. (iv) To produce antibacterial coatings which are essential for medicine and food technologies [13].

There are different approaches for the formation of metal/polymer composites among which are vapour phase deposition, wet chemistry, ion implantation and some others [14]. All these techniques have their advantages and disadvantages. For example, ion implantation provides a possibility to fill polymers with practically any metal and control its concentration [2,15,16]. However, to nucleate NPs high fluences are required that leads to radiation damage of the polymer matrix and changes of its composition [2,17–20]. Poor control of particle sizes and a relatively wide spread of NPs in depth due to straggling of ion projected ranges are other disadvantages [16,21].

Recently, it has been demonstrated that the cluster beam technique is an efficient method for embedment of metal NPs into polymers [22,23]. The advantages of this approach are (i) in very good control of cluster composition due to the formation in vacuum from pure targets, (ii) a possibility to tune particle sizes prior the deposition or embedding and (iii) in the ability to vary the impact energy [24]. This approach provides fascinating capabilities for the formation of polymer films filled by NPs and these composites demonstrate tunable optical and electrical properties [25,26]. However, the mechanisms governing cluster immersion and properties of embedded NPs require better understanding as well as methodologies to control this process need to be further developed for the synthesis of polymer composites with desired properties.

In the current work, size-selected copper cluster ions produced by magnetron sputtering cluster apparatus (MaSCA) are deposited in the low-energy regime on poly(methyl methacrylate) (PMMA) films prepared by spin-coating. The experiments have shown that NP immersion can be driven by thermal annealing, thus, opening

---

[*] Corresponding author.
E-mail address: vp@nano.aau.dk (V.N. Popok).

http://dx.doi.org/10.1016/j.nimb.2017.05.009
0168-583X/

great capabilities to form metal/polymer nanocomposites with properties attractive for practical applications. The results are compared with the previous work on the embedding of silver clusters into PMMA [23].

2. Experimental

Metal clusters are produced using MaSCA. Schematic drawing of the apparatus is presented in Fig. 1. For cluster production, a commercial source (NC200U, Oxford Applied Research) is utilized. In the source, a metal target of 99,99% purity is sputtered, clusters are formed and expanded into the source chamber through the nozzle. Thereafter, they are collimated into a beam by the conical in shape skimmer and steered into the electrostatic quadrupole mass selector (EQMS). The clusters in the source are formed in different sizes; a significant fraction of them is ionized that allows mass (size) selection by electrostatic fields as earlier described in [27]. The experiments with silver have demonstrated that the standard deviation of the particle diameters within 7% is achieved for optimized EQMS parameters [23]. The results of size-selection for copper particles deposited on Si substrate are shown in Fig. 2 demonstrating very similar values of standard deviation (6–9%), thus, confirming reliability of size selection for different metals.

The current work is focused on the study of copper clusters and the results are compared to those earlier obtained for silver ones [23]. Size-selected negatively charged copper cluster ions are soft-landed on substrates with PMMA film in the deposition chamber with the background pressure of ca. 5×10^{-7} mbar. The clusters are selected using voltage $U_{QP} = \pm 500$ V resulting in NPs with mean diameters of 15 nm as follows from the curve presented in Fig. 2. Typical coverages used in the experiments are below a monolayer of NPs. Polymer films are prepared by a standard spin coating procedure on quartz substrates from 1% solutions in chlorobenzene (molecular weight 950K PMMA C 9 from MicroChem). The films are produced in 50 nm thicknesses and annealed in ambient atmosphere at 100 °C for 10 min. to solidify them and evaporate remaining solvents. After the cluster deposition, the samples are annealed again at 120 °C for 10 min. This temperature is above the glass transition point of PMMA (105 °C) allowing to increase viscoelasticity of the material and "chain mobility" favoring embedment of NPs into the films [14].

Surface morphology of the samples with supported NPs is studied by atomic force microscopy (AFM) in tapping mode using Ntegra Aura nanolaboratory (from NT-MDT). Commercial cantilevers with sharp silicon tips (radius of curvature < 10 nm) are used.

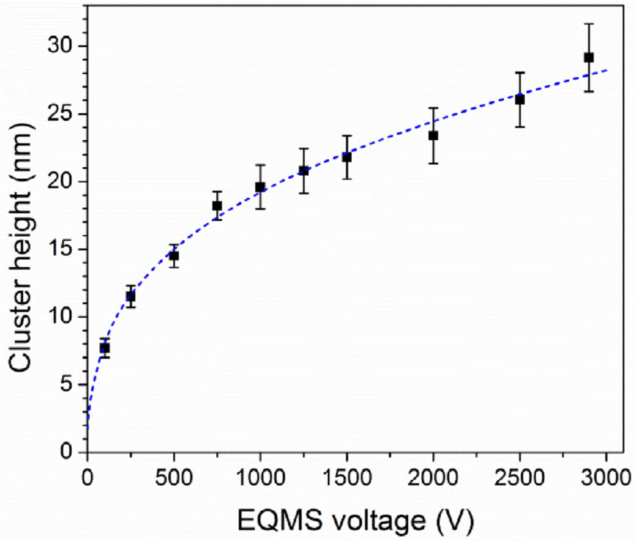

Fig. 2. Measured by AFM height of Cu clusters deposited on Si substrate versus voltage applied to EQMS. Error bars show standard deviations of cluster height.

The extinction spectra are obtained from transmission measurements using a double beam Perkin Elmer High-Performance Lambda 1050 Spectrometer in standard configuration.

3. Results and discussion

AFM images of the samples with as-deposited copper clusters and after the annealing are presented in Fig. 3. The height of NPs after the annealing is decreased indicating partial immersion of the clusters into PMMA. This phenomenon was studied in detail in our previous work with silver and NPs embedment was directly confirmed by cross-sectional transmission electron microscopy [23]. It was also shown that the degree of immersion can be controlled by the duration of thermal annealing. According to the theory presented elsewhere [14,28], the driving force for this process is a large difference in surface free energy (surface tension) between metals and polymers. For example, surface tension (γ) is known to be $\approx$ 1200 mJ/m^2 for silver, 1650 mJ/m^2 for copper, while $\gamma \approx$ 30–40 mJ/m^2 for PMMA [29,30].

Extinction spectra of the samples with copper NPs on/in PMMA are shown in Fig. 4. The spectra for as-deposited clusters demon-

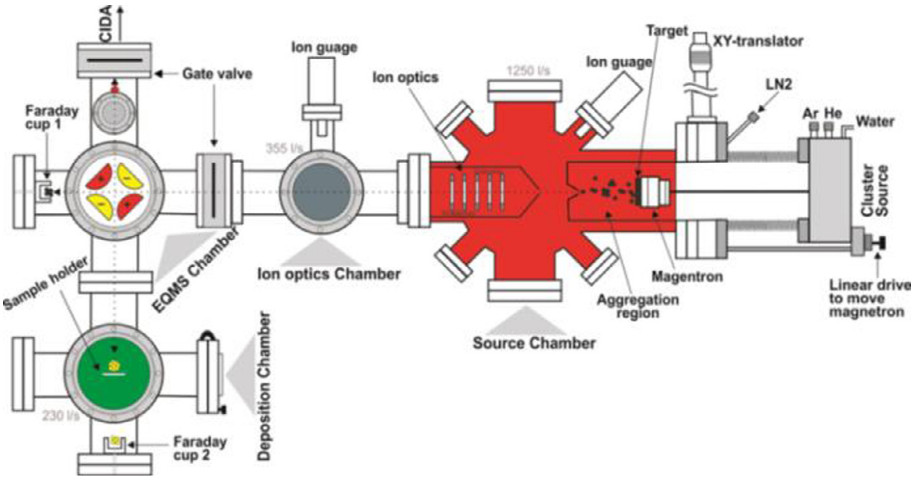

Fig. 1. Schematic view of MaSCA.

Please cite this article in press as: V.N. Popok et al., Immersion of low-energy deposited metal clusters into poly(methyl methacrylate), Nucl. Instr. Meth. B (2017), http://dx.doi.org/10.1016/j.nimb.2017.05.009

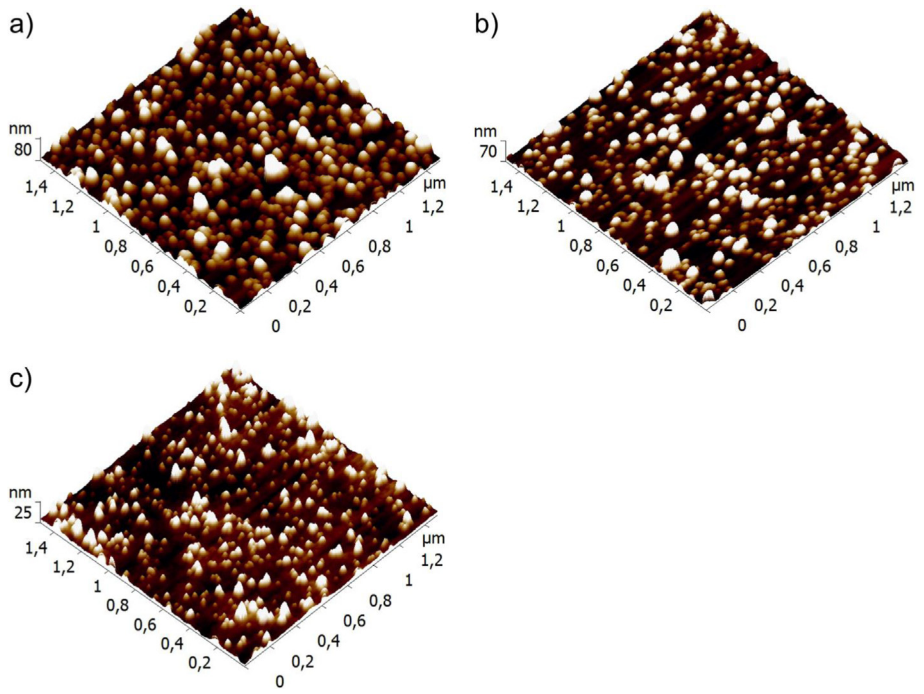

Fig. 3. AFM images of samples with (a) as-deposited copper NPs, (b) after thermal annealing and (c) after second thermal annealing.

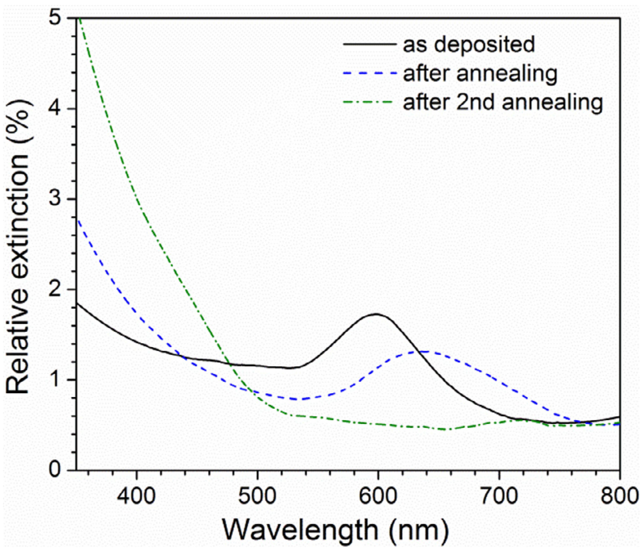

Fig. 4. Relative extinction as a function of wavelength for PMMA with copper NPs before and after thermal annealing.

strate LSPR band with a maximum at wavelength $\lambda \approx 590$ nm which agrees well with the theoretical expectation utilizing Mie theory and giving an equation for the extinction efficiency

$$Q_{ext} = \frac{24\pi R \varepsilon_{med}^{3/2}}{\lambda} \frac{\varepsilon_{im}}{\varepsilon_{im} + (\varepsilon_r + 2\varepsilon_{med})^2} \quad (1)$$

where R is the NP radius, ε_r and ε_{im} are the real and imaginary parts of the metal particle dielectric constant, respectively, ε_{med} is the dielectric function of the surrounding medium. This formula yields a maximum of efficiency for copper NP in air at $\lambda \approx 560$ nm. However, the presence of particles on the polymer surface requires to take into account the dielectric constant of PMMA leading to so-called effective dielectric function [31], which is higher than that of air, thus, causing a "red shift" of the band with respect to the value calculated for air. Immersion of NPs into polymer under the annealing leads to a further increase of ε_{med} which according to Eq. (1) should cause a larger "red shift" and the rise of Q_{ext}. We can clearly observe the "red shift" of the plasmon band for immersed particles in Fig. 4. However, the intensity of the plasmon band is decreased. To better understand the effect of thermal treatment on the plasmonic properties of the composite one more annealing at 120 °C for 10 min. is carried out. The clusters are observed to immerse deeper (see Fig. 3c) but LSPR is almost completely damped as can be seen in Fig. 4. The quenching of the plasmon resonance of the copper NPs after thermal annealing and embedment into PMMA is found to be in contradiction with the theory and the earlier observed results on Ag NPs in PMMA where a significant increase of the plasmon band intensity was observed after thermal annealing and particle embedding [23]. The most probable origin of the plasmon quenching is the high reactivity of copper, in particular, with atmospheric oxygen which is a well-known phenomenon [32,33]. One can expect that this reaction is greatly promoted at elevated temperatures. It is also possible that PMMA, as the oxygen containing polymer, can play some role in this process.

To test the hypotheses of oxidation and possible role of PMMA, Cu clusters are deposited on a quartz substrate (without PMMA) and subjected to thermal annealing. As one can see in Fig. 5, the evolution of LSPR band undergoes a very similar tendency to that presented in Fig. 4. After the first annealing the band is "red shifted" and slightly increased in intensity which can be related to partial oxidation of copper leading to the formation of a surrounding with higher ε_{med}. The second annealing causes damping of the resonance which can be assigned to further rapid conversion of metallic copper into oxide. Most probably, PMMA does not play any important role in this process because the tendencies of the resonance quenching are very similar in the presence and absence of PMMA. Furthermore, the annealing temperatures are low for massive rupture of chemical bonds and release of oxygen.

Please cite this article in press as: V.N. Popok et al., Immersion of low-energy deposited metal clusters into poly(methyl methacrylate), Nucl. Instr. Meth. B (2017), http://dx.doi.org/10.1016/j.nimb.2017.05.009

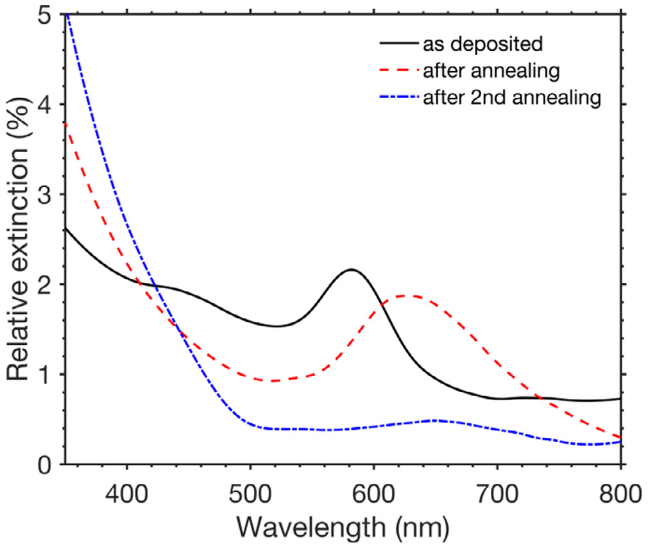

Fig. 5. Relative extinction as a function of wavelength for copper NPs on quartz before and after thermal annealing.

Formation of a protective shell could be a possible solution to preserve LSPR of copper NPs. The following procedure is tested. The particles deposited on the polymer surface are treated with ozone for 20 min. at room temperature. As the result of ozonation the formation of continuous oxide shell coating the metal core is expected, thus, protecting the core against the degradation of its plasmonic properties. One can see in Fig. 6 that the LSPR undergoes “red shift” and the extinction efficiency is increased after the ozone treatment. This behavior is in line with an expectation about the oxide shell formation. The plasmon resonance band is more “red shifted” after the following thermal annealing (120 °C for 10 min.) and contrary to the case of particles non-treated with ozone the band intensity is increased. Then, LSPR preserves on a long time scale (3 weeks) under ambient atmospheric conditions (room temperature and relative humidity of 30–50%). More studies are required to directly prove the shell formation and to understand the dynamics of the reaction processes.

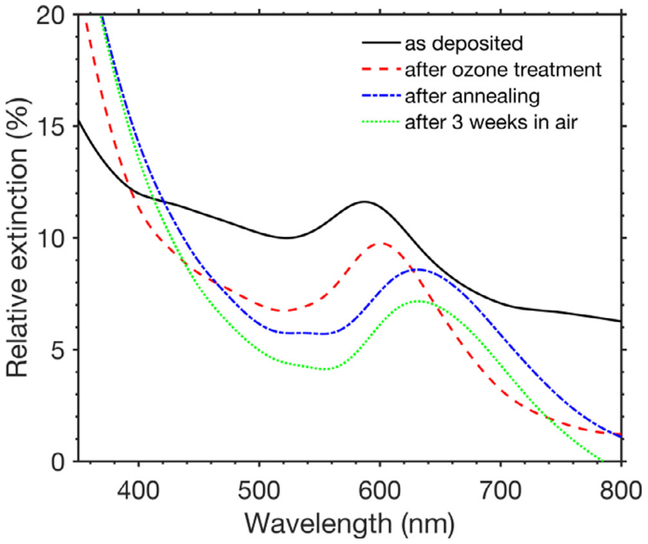

Fig. 6. Relative extinction as a function of wavelength for copper NPs on polymer after ozone treatment, following annealing and long term storage in ambient atmospheric conditions.

4. Conclusions

Size-selected copper NPs are deposited on PMMA films utilizing magnetron sputtering cluster apparatus. Thermal annealing at temperatures above the glass transition point leads to the immersion of the soft-landed clusters into the polymer bulk. This technically simple treatment opens great capabilities for the formation of thin polymer films with either partly or fully embedded size-selected NPs and a controlled filling factor of NPs by the initial cluster surface coverage. The Ag-PMMA composites demonstrate excellent plasmonic properties characterized by a narrow band and high-quality factor of resonance. However, in the case of Cu NPs the thermal annealing causes quenching of LSPR along with the particles immersion. It is suggested that the thermal treatment significantly enhances reactivity of copper with species present in ambient air (most probably with oxygen) causing the conversion of metal copper into copper compounds (oxides) and suppression of the plasmonic properties. This hypothesis is supported by the experiments on the annealing of Cu clusters deposited on quartz demonstrating the same tendency in damping of the plasmon resonance under the thermal treatments, thus, excluding any significant role of PMMA or other effects related to the particle immersion. However, a more detailed study of this phenomenon is required for better understanding the origins and mechanisms. Treatment of metal NPs with ozone is found to be an efficient route to form an oxide shell around the metal core, thus, protecting particles against degradation of the plasmonic properties due to environmental factors.

References

[1] F. Faupel, V. Zaporojtchenko, T. Strunskus, M. Elbahri, Adv. Eng. Mater. 12 (2010) 1177–1190.
[2] V.N. Popok, Rev. Adv. Mater. Res. 30 (2012) 1–26.
[3] M.C. Salvadori, M. Cattani, F.S. Teixeira, I.G. Brown, Appl. Phys. Lett. 93 (2008) 073102.
[4] E. Barborini, G. Corbelli, G. Bertolini, P. Repetto, M. Leccardi, S. Vinati, P. Milani, New J. Phys. 12 (2010) 073001.
[5] V.N. Popok, M.G. Lukashevich, S.M. Lukashevich, R.I. Khaibullin, V.V. Bazarov, Surf. Sci. 566–568 (2004) 327–331.
[6] C.B. Murray, S. Sun, H. Doyle, T. Betley, MRS Bull. 26 (2001) 985.
[7] C. Okay, B. Rameev, R.I. Khaibullin, M. Okutan, F. Yildiz, V.N. Popok, B. Aktas, Phys. Stat. Sol. 203 (2006) 1525–1532.
[8] A. Moores, F. Goettmann, New J. Chem. 30 (2006) 1121–1132.
[9] S. Zeng, D. Baillargeat, H.-P. Ho, K.-T. Yong, Chem. Soc. Rev. 43 (2014) 3426–3452.
[10] K.A. Willets, R.P. Van Duyne, Annu. Rev. Phys. Chem. 58 (2007) 267–297.
[11] K.J. Russel, T.-L. Liu, S. Cui, E.L. Hu, Nature Phot. 6 (2012) 459.
[12] G.M. Akselrod, C. Argyropoulos, T.B. Hoang, C. Ciracì, C. Fang, J. Huang, D.R. Smith, M.H. Mikkelsen, Nature Phot. 8 (2014) 835.
[13] H. Palza, Int. J. Mol. Sci. 16 (2015) 2099–2116.
[14] J. Prakash, J.C. Pivin, H.C. Swart, Adv. Colloid Interface Sci. 226 (2015) 187–202.
[15] R.I. Khaibullin, V.N. Popok, V.V. Bazarov, E.P. Zheglov, B.Z. Rameev, C. Okay, L.R. Tagirov, B. Aktas, Nucl. Instr. Meth. Phys. Res. B 191 (2002) 810–814.
[16] A. Meldrum, R.F. Haglund Jr., L.A. Boatner, C.W. White, Adv. Mater. 13 (2001) 1431–1444.
[17] V.N. Popok, I.I. Azarko, V.B. Odzhaev, A. Toth, R.I. Khaibullin, Nucl. Instr. Meth. B 178 (2001) 305–310.
[18] D.V. Sviridov, Rus. Chem. Rev. 71 (2002) 315–327.
[19] A. Kondyurin, M. Bilek, Ion Beam Treatment of Polymers, Elsevier, Amsterdam, 2008.
[20] V.N. Popok, M. Hanif, A. Mackova, R. Miksova, J. Polym. Sci. B 53 (2015) 664–672.
[21] V.N. Popok, Rev. Adv. Mater. Sci. 36 (2014) 1–12.
[22] C. Ghisleri, F. Borghi, L. Ravagnan, A. Podesta, C. Melis, L. Colombo, P. Milani, J. Phys. D 47 (2014) 015301.
[23] M. Hanif, R.R. Juluri, M. Chirumamilla, V.N. Popok, J. Polym. Sci. B 54 (2016), 1152-11.
[24] C. Binns, Surf. Sci. Rep. 44 (2001) 1–49.
[25] G. Corbelli, C. Ghisleri, M. Marelli, P. Milani, L. Ravagnan, Adv. Mater. 23 (2011) 4504–4508.
[26] C. Minnai, P. Milani, Appl. Phys. Lett. 107 (2015) 073106.
[27] H. Hartmann, V.N. Popok, I. Barke, V. von Oeynhausen, K.-H. Meiwes-Broer, Rev. Sci. Instr. 83 (2012) 073304.
[28] G.J. Kovacs, P.S. Vincett, Thin Solid Films 111 (1984) 65–81.
[29] F. Aqra, A. Ayyad, Appl. Surf. Sci. 314 (2014) 308–313.

Please cite this article in press as: V.N. Popok et al., Immersion of low-energy deposited metal clusters into poly(methyl methacrylate), Nucl. Instr. Meth. B (2017), http://dx.doi.org/10.1016/j.nimb.2017.05.009

[30] F. Ruffino, V. Torrisi, G. Marletta, M.G. Grimaldi, Appl. Phys. A 107 (2012) 669–683.

[31] A. Curry, G. Nusz, A. Chilkoti, A. Wax, Opt. Express 13 (2005) 2668–2677.

[32] M. Shi, H.S. Kwon, Z. Peng, A. Elder, H. Yang, ACS Nano 6 (2012) 2157–2164.

[33] V.G. Kravets, R. Jalil, Y.-J. Kim, D. Ansell, D.E. Aznakayeva, B. Thackray, L. Britnell, B.D. Belle, F. Withers, I.P. Radko, Z. Han, S.I. Bozhevolnyi, K.S. Novoselov, A.K. Geim, A.N. Grigorenko, Sci. Rep. 4 (2014) 5517.

Please cite this article in press as: V.N. Popok et al., Immersion of low-energy deposited metal clusters into poly(methyl methacrylate), Nucl. Instr. Meth. B (2017), http://dx.doi.org/10.1016/j.nimb.2017.05.009

Appendix B

MATLAB Script for Height Distribution

B.1. Main Script

```
%% MATLAB script for comparison of cluster mean height before and after annealing of the samples

% AFM images of samples (before and after annealing), which are
% saved as text files, are read and converted into grayscale
% images
image_before = dlmread('text_files/Name_of_file.txt');
image_after = dlmread('text_files/Name_of_file.txt');
before = mat2gray(image_before);
after = mat2gray(image_after);

% Binary Image Processing, where the threshold of the images
% can be adjusted in order to select background
% (polymer film) and foreground (polymer film+clusters)
[before_fg,before_bg] = mybinaryimage(before,0.62,0.63);
[after_fg,after_bg] = mybinaryimage(after,0.59,0.59);

figure;
% Height of the clusters is calculated for both samples
before_height = image_before(before_fg) - mean(image_before(before_bg));
after_height = image_after(after_fg) - mean(image_after(after_bg));

% Height distributions are plotted in one graph, and
% mean height and standard deviation are added for
% each sample
hold on;
plotting(before_height);
plotting(after_height);
hold off;
```

B.2. Supplementary Functions

```
function [foreground,background] = mybinaryimage(image,threshold_fg,threshold_bg)

binary = imbinarize(image,'adaptive','ForegroundPolarity','bright','Sensitivity',threshold_fg);
foreground = binary;
blending(foreground + 0,image);
binary = imbinarize(image,'adaptive','ForegroundPolarity','bright','Sensitivity',threshold_bg);
background = not(binary);
blending(background + 0,image);
end
```

```
function blending(doublebinaryimage,image)

H = vision.AlphaBlender; %returns an alpha blending System object (H) that combines the pixel of two images, using opacity factor of 0.75
J = step(H,doublebinaryimage,image); %performs alpha blending operation on images 'doublebinaryimage' and 'image'
figure;
imshow(J); %displays pixels with value 0 as black and 1 as white for binary images
end
```

```
function plotting(x)

% Histogram with smoothing fit is constructed
histfit(x(:),[],'kernel');

% Calculation of mean cluster height
meanofpart = mean(x(:));
meanofpart = num2str(round(meanofpart,1));

% Calculation of standard deviation
stdev = std(x(:));
stdev = num2str(round(stdev,1));

str = {['<\ith\rm> = ' meanofpart ' nm'],['Std. dev. = ' stdev ' nm']};
annotation('textbox',dim,'String',str,'FontSize',24,'FitBoxToText','on');
```

```
xlabel('Clusters height [nm]')
ylabel('Counts')
end
```